NTNU

Norwegian University of
Science and Technology

Charged Particle Trajectories in the Local Superbubble

Kristian Joten Andersen

Master of Science in Physics and Mathematics
Submission date: June 2017
Supervisor: Michael Kachelriess, IFY

Norwegian University of Science and Technology
Department of Physics

Abstract

In this thesis we study the propagation of cosmic rays (CR) emitted by sources in the Local Superbubble (LB). There are many bursting sources of CRs inside the LB which may be modelled as a continuous injection of CRs, and therefore we study the LB's effect on CRs by calculating trajectories of individual protons from both a continuous and a bursting source within two models of the LB's magnetic field. These models are constructed using information from literature, each having a regular and random component for which we assume equipartition of energy. We find that the escape time $t_{\mathrm{esc}}(E)$ has a knee-like feature around $E/Z = 5 \cdot 10^{15}$ eV for coherence lengths of the random field smaller than the LB's radius. Additionally, we find that $t_{\mathrm{esc}}(E) \propto E^{-\alpha}$ for energies $E \leq 2 \cdot 10^{15}$ eV where α was calculated to be $\alpha = 0.354 \pm 0.008$. The results are not entirely conclusive and we would have to run more simulations to validate that the knee-like feature stems from the bubble itself.

Preface

This thesis is written as part of my Master's project for my Master of Science degree in Astrophysics. It is worth 30 ECTS credits and is being completed at the Norwegian University of Science and Technology, NTNU, Trondheim. The work has been done under the supervision of Prof. Michael Kachelrieß at the Department of Physics.

Kristian Joten Andersen

Trondheim, June 2017

Acknowledgment

I would especially like to thank Prof. Michael Kachelrieß for providing me with this very interesting Master's project. It has been both a rewarding and challenging task to work on. Also, I would like to thank him for his patience with me and his indispensable help in finding helpful written books and articles on the topic, and for helpful critique and proof reading while writing this thesis.

I would like to thank my brother Vegard Joten Andersen for his helpful critique in English writing while writing this thesis, and for his additional proof reading making the text more comprehensible. Lastly I would like to thank all my fiends whom I met during my studies in Trondheim and Munich for making these five years a joyful time.

K.J.A.

Contents

Chapter 1

Introduction

1.1 Background

According to articles (e.g. Schulreich et al., 2017), our solar system resides within a superbubble (SB) in the interstellar medium (ISM) called the Local Bubble (LB). A SB is a low-density cavity in the ISM, partially filled with hot, soft X-ray emitting plasma. The existence of the LB is widely accepted today, especially after it was found by Galeazzi et al. (2014) to contribute to 60% ($\pm$ 5%) of the 0.25 keV flux in the Galactic plane. From observations the LB is estimated to extend roughly 200 pc in the galactic plane and 600 pc perpendicular to the galactic plane (Galeazzi et al., 2014; Schulreich et al., 2017). Its origin is still an ongoing debate within the scientific community.

Several articles have been written on the subject of the origin of SBs. The leading thesis is that they are created by multiple supernovae (SNe) and stellar winds (SWs) pushing against the gas and dust in the ISM creating a low-density cavity with hot plasma (e.g. see Schulreich et al., 2017; van Marle et al., 2015; Lingenfelter, 2013). The massive O and B stars (> 8 solar masses, $M_\odot$), the progenitors of core collapse SNe, together with other stars down to $\sim 0.1\ M_\odot$ are born in highly compact, star formation regions, i.e. the densest parts of giant molecular clouds (Lingenfelter, 2013). An order of up to 10^5 stars may be formed within a few pc over a time span of $\sim$ 1 Myr, where roughly 100 are SN progenitors. The most massive stars have a lifetime of $\sim$ 3 Myr, while the least massive last $\sim$ 35 Myr. These clusters of stars are normally known as OB star associations (or just OB associations).

To get a deeper understanding of the structure and evolution of SBs one would need to solve a full-blown set, or include also the effect of magnetic fields, of magnetohydrodynamical equations through numerical simulations. Schulreich et al. (2017) attempted this with the LB by back-tracing stars in nearby OB associations who may have initially created or later entered the LB, and then subsequently exploded as SNe, increasing the size of the LB. The result from their model with warm ionized ISM can be seen in Fig. 1.1. Though the resulting SB does not precisely match the physical observations of the LB in size, it gives an informative evolution picture of a SB.

The article by van Marle et al. (2015) shows that the size and shape of a bubble created by SWs and SN explosions are dependent of the magnetic field (MF), mass density, and temperature of the ISM. The general result was that a constant MF in the ISM is shown to prohibit the growth of the bubble in directions perpendicular to the MF lines. The final shape of the SB is mostly

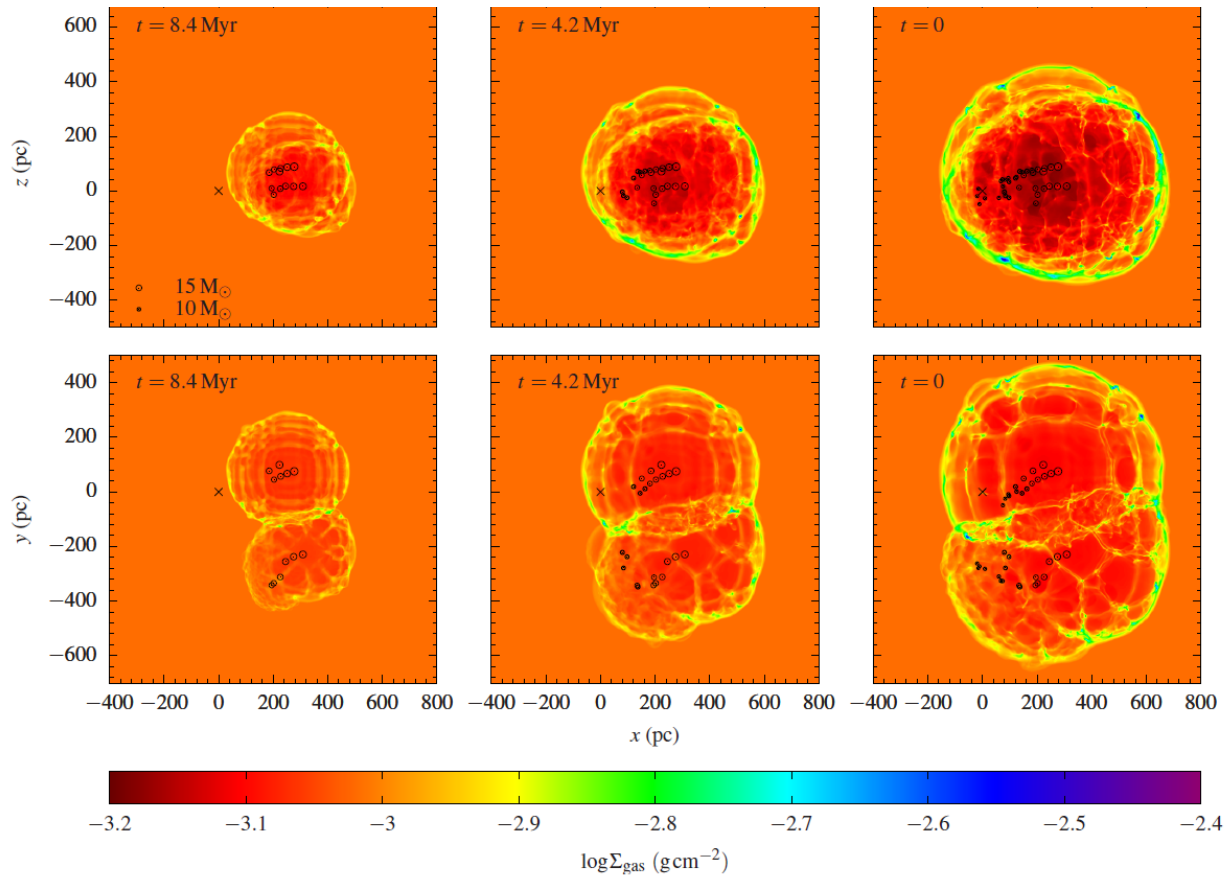

Figure 1.1: Colour-coded maps of the logarithmic total gas column density for three different times before present. Integrations along the y- and z-axis are shown in the upper and lower panels, respectively. Earth's projected position is marked by a cross. Circles indicate the projected centres of SN explosions that occurred in the time frame before the snapshot was taken. The sizes of the circles correspond to the initial masses of the progenitor stars (see legend in the upper left panel). From Schulreich et al. (2017).

determined by the first SN (Schulreich et al., 2017), so any SB created will have a shape that is highly dependent of the MF in the ISM.

Cosmic rays (CRs) are subatomic particles of extra-terrestrial origin. Though they are mostly protons, the other CRs (e.g. gammas, neutrinos, and heavy nuclei) are also very important due to different particle properties (e.g. electric charge, mass to charge ratio, and interaction cross section) that make them propagate differently through the galactic and extragalatic media, while also effect our abilities to observe them. We know that most particles originate from sources in the local galaxy, and that the charged CRs are then being dispersed in the ISM through diffusive motion until they finally escape into intergalactic space (Simpson and Garcia-Munoz, 1988). We also know that the diffusion in the MF of the ISM has the property that higher energy CR diffuse more quickly than lower energy ones, i.e. they escape faster (Gaisser et al., 2013).

The cosmic ray spectra are of great interest as their energy and composition may give information about their sources. As cosmic rays enter the Earth's atmosphere, they collide with air molecules generating air showers. In order to measure the CR spectrum directly, one would

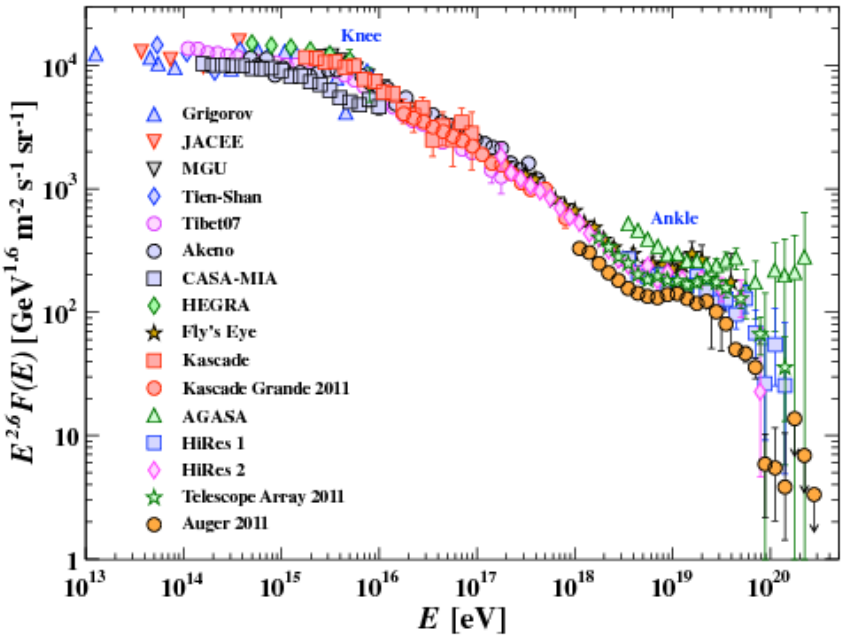

Figure 1.2: Measurements of the all-particle cosmic ray diffuse flux $F(E)$ air shower observatories. Additionally, the positions of the "knee" and "ankle" are indicates. From Beringer et al. (2012)

have to go to balloon borne or satellite stationed detectors. The problem with these are that they are very small, and in the case of satellites very expensive, and therefore are limited in the amount of CR particles that may hit them. This becomes an increasing problem with higher energies when the flux of particles becomes decreasingly smaller, e.g. the CR flux above 100 TeV amounts to about 5 particles per square meter per steradian per day (Gaisser et al., 2013). That is why data for the energy spectrum for the larger energies comes from large air shower arrays on the ground, that determine the CR energies indirectly through observations and measurements of secondary particles created in air showers initiated by the CR particles. The all-particle spectra of very high energy (VHE) cosmic rays from several air shower observatories, starting at energy level 10^{13} eV, can be seen in Fig. 1.2.

The spectra of CR particles can be described by a steeply falling power law over many decades, approximately E^{-3}, for energies > 10 GeV (Chen et al., 2015). The smoothness of this drop of intensity with energy is broken at 2-3 PeV where there is an index change in the power law, commonly referred to as the "knee". The power law indices below and above the knee are -2.72 ± 0.02 and -2.95 ± 0.02 respectively (Fowler et al., 2001). In addition, at $\sim 3\cdot10^{18}$ eV there is a new change in the power law index known as the "ankle". The origin of the knee and ankle are not completely known. At energies below the knee, supernova remnants (SNRs) are thought to be the primary sources of galactic CRs (Cardillo et al., 2016) where protons are the primary component (Fowler et al., 2001). Above the knee, the composition of the CRs is less well known due to

the small flux of particles. Air shower observatories are limited (at best) to acquire information about the composition of the particles of the air shower (Gaisser et al., 2013; Fowler et al., 2001). In order to gain the most information about the air shower particles, one must observe and measure the air showers at as many heights as possible through different types of telescopes and particle detectors, and then use particle theory to back-trace the cascade particles to the initial particle. One theory is that the composition of the CRs above the knee is primarily heavy nuclei (e.g. iron, see Fowler et al., 2001), though the acceleration source is not generally known. It may be galactic or extra-galactic. The CRs above the ankle are believed to be of extra-galactic origin, primarily from active galactic nuclei (AGNs) or Fermi γ-sources (e.g. Jiang et al., 2010; Kachelrieß et al., 2017).

A less discussed potential source for features in the CR spectra is the Local Bubble. Superbubbles have a low density volume with a (generally) weaker MF than that of the ISM outside (van Marle et al., 2015), while the MF in the bubble wall is stronger. Having a bubble wall with an increased MF strength gives the possibility of reflecting CRs, trapping confined CRs inside or reflecting away CRs from outside. Following the fact that charged particles with increasing energy are deflected less by a MF, the relative amount of reflected CRs will also decrease with increasing CR energy.

Superbubbles are as mentioned earlier made by SN explosions inside a low density bubble in the ISM created by an initial SN (e.g. see Fig. 1.1). Due to the spatial extent of the SBs, both the changing magnetic fields in the ISM outside the bubble and new SN explosions at different locations inside and outside the bubble wall (or shell) will effect the shape and magnetic field structure of the bubble wall (Streitmatter and Jones, 2005). This makes the bubble shell potentially very non-homogeneous which leaves the possibilities for "holes" in the shell or tunnels between neighboring bubbles, through which particles may easier escape. The inhomogeneity of a SB's shell may be seen in Fig. 1.1.

Problem Formulation and Objectives

Being able to explain the features of the cosmic ray spectra is of high interest to astrophysicists as it may give much information of the sources of the CRs and the structure of our Galaxy (and possibly others). Thus this has been a field of research for many years. The Local Bubble is one of the less discussed and researched potential sources to the features that we see in the CR spectra for charged particles (as neutral particles are not effected by magnetic fields in equal magnitude), and is therefore of significant interest. Recently, it has been suggested that a local source is visible in the CR spectra measured and, in particular, explains naturally the anomalies observed in the antimatter fluxes (Savchenko et al., 2015; Kachelrieß et al., 2015). Such a source would reside in the LB and, thus is especially important to understand the influence of the LB on the CR spectra. In addition to bursting sources of CRs, cases where many sources contribute to the CR flux may be modelled as a continuous injection of CRs. So both types of sources would have to be considered in order to best describe the effect of the LB on CRs.

The magnetic field in the ISM (and the LB) is found to have both a regular component and an isotropic random (turbulent) component. In order to most accurately simulate the trajectories of CR particles in the Galactic medium, we will have to use literature to find and set up a computation algorithm for the turbulent magnetic field (TMF). This type of algorithm would also be of interest for anyone looking to simulate charged particle motion in any system with a

TMF.

The main objectives of this thesis are thus:

1. Using literature to set up simplified models of the regular magnetic field of a superbubble resembling the LB.

2. Using literature to set up a computational algorithm of the turbulent magnetic field component of the models in the first objective, that is also fulfilling the requirement of isotropy on the scales of the magnetic field models.

3. Characterize the timing and probability properties of CRs created by a continuous or a bursting source, and the position properties of CRs from a bursting source, all from sources inside the modelled superbubble.

1.2 Approach

For the first objective two models for the MF will be modelled, taking inspiration from van Marle et al. (2015), Beck and Wielebinski (2013), Schulreich et al. (2017), and Streitmatter and Jones (2005).

For the second objective the established algorithm for creating turbulent magnetic fields (see Giacalone and Jokipii, 1999) will be used to compute TMFs using Monte-Carlo (MC) computation. Then we will look at the case of small angle scattering (SAS) in TMFs. Using numerical simulations, the scattering angle of highly energetic charged particles in MC computed TMFs will be compared to literature on SAS (Caprini and Gabici, 2015; Harari et al., 2002) and thus setting a limit on the parameters of the computed TMFs to be used in the MF model of the bubble.

To solve the third objective, first simulations of charged particle trajectories with a continuous source for a few given particle energies will be performed for two MF models and the results will be compared. If the results proves to be approximately equal for the most important energies (i.e. lower energies) only one model will be used for further studies. Then the numerical simulations for a larger set of particle energies will be performed for a continuous source. Lastly, based on the results from the continuous source, simulations of a bursting source for the most interesting particle energies regions will be performed. In order to study the timing and position properties of the CRs, a set of functions will be fitted to the computed results.

1.3 Structure of the Thesis

The rest of the thesis is structured as follows. Chapter 2 covers the general theory of the thesis, where section 2.1 introduces the theory and modelling of both the regular and turbulent magnetic fields. Section 2.2 covers the theory magnetic scattering as well as introducing the computation method for the particle trajectory simulations. Section 2.3 continues on scattering theory of diffusive and ballistic motion, and it introduces the different functions used for analyzing the timing and position data from the simulations. In chapter 3, the results from the computations are presented and discussed following the order of the objectives presented earlier in this chapter. Lastly, chapter 4 gives a short summary of the most important results found in this thesis.

Chapter 2

Theory

2.1 Magnetic Fields

Any electromagnetic system in vacuum needs to satisfy the Maxwell equations

$$\nabla \cdot \boldsymbol{E} = \frac{\rho}{\epsilon_0}, \tag{2.1}$$

$$\nabla \cdot \boldsymbol{B} = 0, \tag{2.2}$$

$$\nabla \times \boldsymbol{E} = -\frac{\partial \boldsymbol{B}}{\partial t}, \tag{2.3}$$

$$\nabla \times \boldsymbol{B} = \mu_0 \left(\boldsymbol{J} + \epsilon_0 \frac{\partial \boldsymbol{E}}{\partial t} \right), \tag{2.4}$$

where $\boldsymbol{E}$ and $\boldsymbol{B}$ is the electric and magnetic field, ρ is the total electric charge density, $\boldsymbol{J}$ is the total current density, and ϵ_0 and μ_0 is respectively the electric permittivity and the magnetic permeability in vacuum. In the case of a static magnetic field, equation (2.3) becomes zero, i.e. there are no induced voltages due to the magnetic field. Further, a constant magnetic field implies that the r.h.s. of equation (2.4) must be constant, where the stable solution is a constant electric field and a constant current density. When considering a magnetic field, equation (2.2) is the most important, as it shows that the divergence of the magnetic field is independent of the electric field and is always zero.

2.1.1 Regular Magnetic Field Model

In order to gain information about CR properties in a SB that may be compared to what we may observe from the LB, we want to model our SB in resemblance with the LB. Through observations of CRs and numerical modelling of spiral galaxies, e.g. our own Milky Way, it is found that an axisymmetric spiral magnetic field configuration best fit the observational data (Beck and Wielebinski, 2013, ch. 3.5), including that one large-scale reversal inside about 1–2 kpc of the solar radius is required. The local field in the spirals are oriented parallel to the galactic plane along the spiral arms. Outside the galactic disc (in the galactic halo), the field lines are found to point more perpendicular to the galactic plane rather than along the spiral arms (Beck and

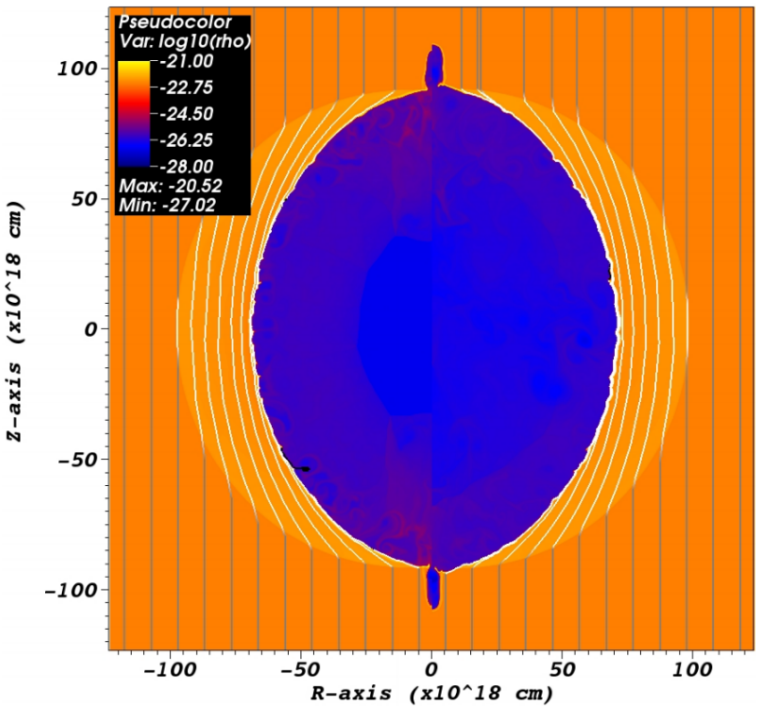

Figure 2.1: Colour-coded map of the logarithmic total gas column density from the end of an evolutionary simulation of a low density bubble created by stellar winds and and a supernova explosion. The field lines of the ISM magnetic field is visible as well. The initial mass of the star in the simulation was 40 $M_\odot$ and the strength of the ISM magnetic field was 5 μG. From van Marle et al. (2015).

Wielebinski, 2013). As the extent of the LB in the galactic plane is about 200 pc (see section 1.1) while being located at ~8 kpc from the galactic center, we model the regular magnetic field outside the bubble in the galactic disc to be constant and pointing in one direction, i.e. exclude curvature of the spiral arm (1 kpc bend ~7.2°).

In van Marle et al. (2015), the bubbles created by SWs and SNe in the ISM with constant magnetic fields take elliptical shapes with sizes depending on the magnetic field strength. The magnetic field lines (MFLs) are pushed outward from the star creating an elliptical magnetic field configuration of the bubble, see Fig. 2.1. For smaller values of the ISM field strength, the field configuration of the bubble becomes more circular in the radial plane (perpendicular to the ISM's MFLs), i.e. more spherical in 3 dimensions.

The Local Bubble has a shape that is closer to a cylinder than a spherical bubble with the cylinder oriented close to the perpendicular direction w.r.t. the galactic plane (Schulreich et al., 2017). Of this reason it would be more valuable to model the SB as a(n) (elliptic) cylinder rather than a sphere (or ellipsoid). Whether or not the LB is magnetically open at the "top" and "bottom" (see Streitmatter and Jones, 2005) would also impact the effect the LB has on CRs, as CRs would potentialy have an easier escape.

To avoid the case of having a magnetically open or closed cylinder we crate an "infinitely" long cylinder where the field is constant perpendicularly to the radial plane (i.e. perpendicularly to the Galactic disc for the LB). Following van Marle et al. (2015), the model field should at least be an elliptic cylinder, but in order to simplify the computations and having the pos-

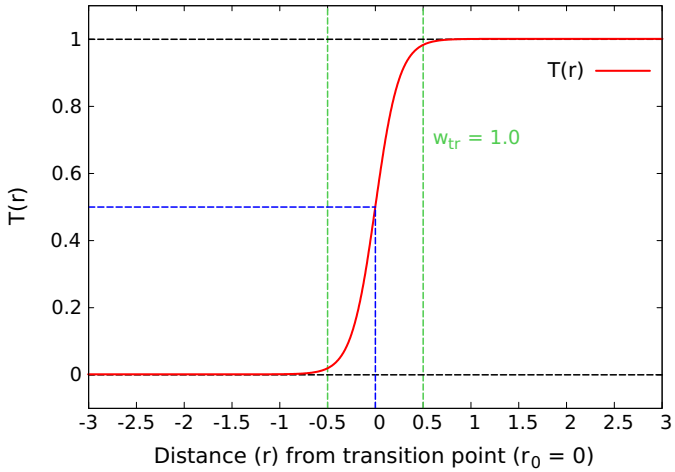

Figure 2.2: The figure shows a plot of the transition function $T(r)$ (see eq. (2.5)). The transition point $r_0 = 0$ and the transition width $w_{\rm tr} = 1.0$.

sibility for cylindrical symmetry, we set the shape of the model field to be circular rather than elliptic. In addition, we introduce two models for the cylindrical field's direction which will now be presented.

Magnetic Field Transition and Strength

To describe the transition between the regular MF in the ISM and the MF of the SB, the following transition function is used:

$$T(r) = \frac{1}{1 + \exp\left(\frac{-8(r-r_0)}{w_{\rm tr}}\right)}, \tag{2.5}$$

where r_0 is the transition point and $w_{\rm tr}$ the transition width. With the choice of 8 in the exponent the transition width is then the width at which the function goes from 1.8% to 98.2% of its maximum value of 1. A plot of equation (2.5) with $w_{\rm tr} = 1.0$ and $r_0 = 0$ can be seen in Fig. 2.2.

In the model of the SB the MF in the ISM outside the bubble is assumed to be constant and pointing in the direction of the spiral arm from here on referred to as the x-axis. The z-axis is pointing along the cylindrical wall of the SB, perpendicular to the Galactic disc defined by the xy-plane. To model the magnetic field we create a unit field representation of the MF using eq. (2.5), and then multiply it with a model of the magnetic field strength. We introduce $\hat{\boldsymbol{b}}$ as a unit vector pointing along the MFLs in the direction of the field at any position. Outside the bubble one simply has

$$\hat{\boldsymbol{b}}(\boldsymbol{r}) = \hat{\boldsymbol{b}}_{\rm out}(\boldsymbol{r}) = \hat{\boldsymbol{x}}, \tag{2.6}$$

where $\boldsymbol{r}$ is the position vector.

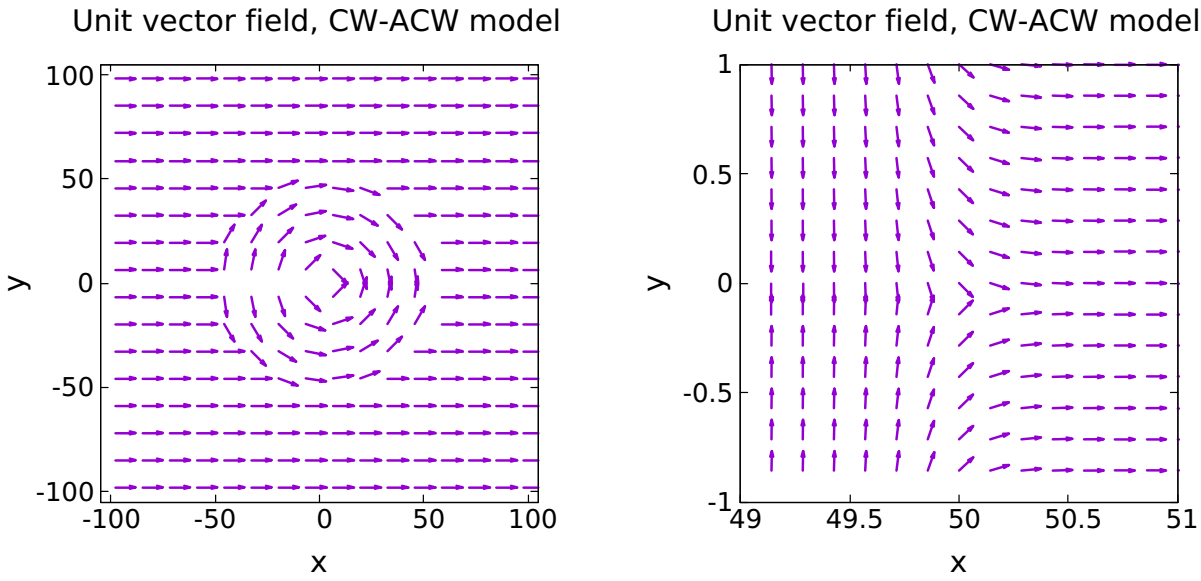

Figure 2.3: Unit vector field plot of the constant outer field, and a circular clockwise ($y > 0$) and anticlockwise ($y < 0$) oriented inner field, with transition radius $r_0 = 50$ and transition width $w_{\text{tr}} = 1.0$ between the inner and outer fields. The left shows the whole inner field while the right is zoomed in on the right edge of the inner field ($y = 0$). Note: the vectors are not to scale, but are re-sized for easier viewing.

For the bubble field we use two representations:

1. A clockwise field for $y > 0$ and anticlockwise for $y < 0$ (CW-ACW).
2. A clockwise field for all values of (x, y) (CW).

The unit vector $\hat{\boldsymbol{b}}$ inside the bubble then becomes

$$\hat{\boldsymbol{b}}_{\text{in},1}(\boldsymbol{r}) = |\sin(\phi)|\hat{\boldsymbol{x}} - \cos(\phi)\frac{\sin(\phi)}{|\sin(\phi)|}\hat{\boldsymbol{y}} \tag{2.7}$$

for the first representation and

$$\hat{\boldsymbol{b}}_{\text{in},2}(\boldsymbol{r}) = \sin(\phi)\hat{\boldsymbol{x}} - \cos(\phi)\hat{\boldsymbol{y}} = -\hat{\boldsymbol{\phi}} \tag{2.8}$$

for the second, where ϕ is the angular position in the xy-plane, positive x-axis referring to $\phi = 0$ and oriented anticlockwise. Using eq. (2.5), identifying r_0 as the effective transition radius, one can make a superposition $\boldsymbol{s}(\boldsymbol{r})$ of the inner and outer field:

$$\boldsymbol{s}(\boldsymbol{r}) = T(r) \cdot \hat{\boldsymbol{b}}_{\text{out}}(\boldsymbol{r}) + (1 - T(r)) \cdot \hat{\boldsymbol{b}}_{\text{in}}(\boldsymbol{r}), \tag{2.9}$$

where $r = |\boldsymbol{r}|$. Consequently, $\hat{\boldsymbol{b}}$ becomes for any position $\boldsymbol{r}$

$$\hat{\boldsymbol{b}}(\boldsymbol{r}) = \frac{\boldsymbol{s}(\boldsymbol{r})}{|\boldsymbol{s}(\boldsymbol{r})|}. \tag{2.10}$$

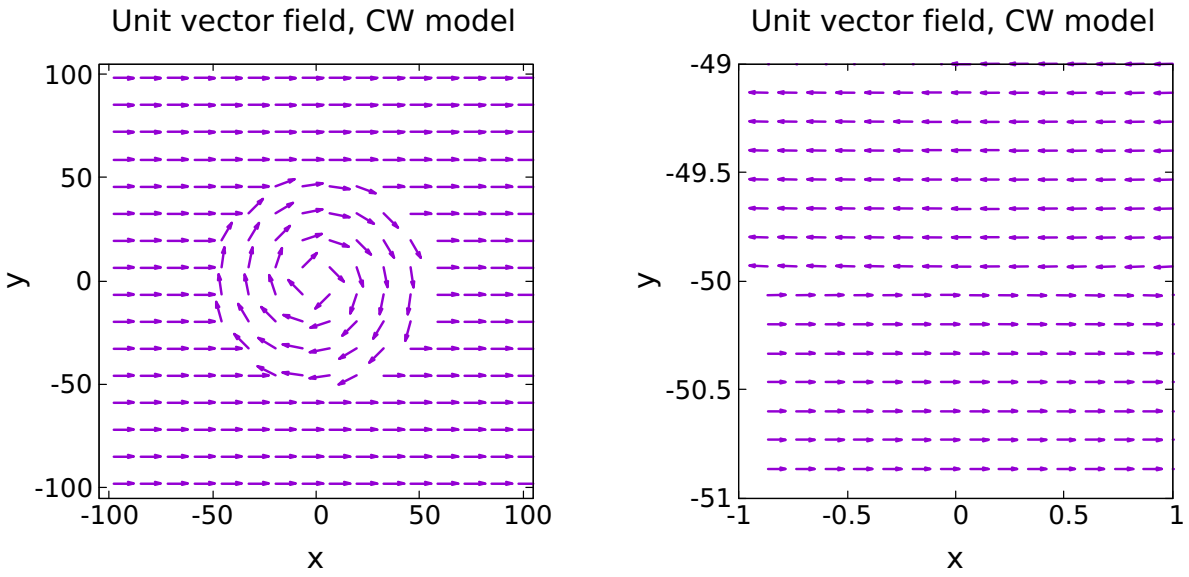

Figure 2.4: Unit vector field plot of the constant outer field and a circular clockwise oriented inner field, with transition radius $r_0 = 50$ between the fields and transition width $w_{\rm tr} = 1.0$. The left shows the whole inner field while the right is zoomed in on the lower edge of the inner field $((x, y) = (0, -50)$. Note: the vectors are not to scale, but are re-sized for easier viewing.

Outside the effective transition region, i.e. $r = r_0 \pm 0.5 w_{\rm tr}$ (see eq. (2.5)) eq. (2.9), and consequently (2.10), is reduced to either $\hat{\boldsymbol{b}}_{\rm in}$ or $\hat{\boldsymbol{b}}_{\rm out}$. Example unit fields of eq. (2.10) are shown in Fig. 2.3 and Fig. 2.4, with the first and second representation of the inner field respectively.

The two representations of the inner field have different implications. The second one fulfills all of Maxwell's equations (see eqs. (2.1)-(2.4)), but gives a sharp flip of the magnetic field at $(x, y) = (0, -r_0)$ where the outer and inner field point in opposite directions (see Fig. 2.4). The first representation clearly violate eq. (2.2) by having magnetic monopoles (see Fig. 2.3), which are hypothetical particles as far as we know and that some scientist are trying to prove the existence of (e.g. see Bramwell et al., 2009). Opposite to the second, the first representation does not have any sharp flip transitions between the outer and inner field. In addition, it follows the direction of the outer field as one might expect if the bubble were to be formed in a constant field and then pushes the external field lines outwards (see van Marle et al., 2015). To see whether there is any difference in the results between the two representations, we will initially use both in our computations. If they prove to be approximately equal in the results, only one will be used for more extensive computations in order to save computing time.

The root mean square (RMS) strength of the magnetic field in the ISM surrounding the LB is estimated to be $B_{\rm RMS} \approx 5$ μG (Beck and Wielebinski, 2013; Sun et al., 2008; van Marle et al., 2015), where according to Sun et al. (2008) $\approx 60\%$ is residing in a random turbulent field. This distribution of the field strength has proven hard to confirm through other sources, and the article by Sun et al. (2008) itself refers to the value of the turbulent field in some places as a mean in the Galactic disc. Of this reason the distribution of the MF strength is chosen to be equally divided between the turbulent and the local (regular) field. While the structure of the turbulent field is discussed in section 2.1.2, we will here take a closer look at the $B_{\rm RMS}$ value of

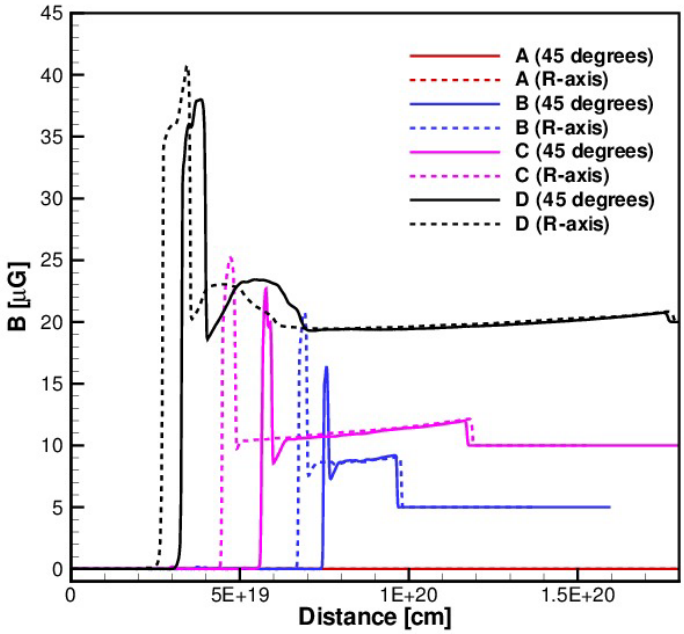

Figure 2.5: From van Marle et al. (2015). The figure shows the magnetic field strength along cuts through 2D simulation results (as described in van Marle et al., 2015) at the end of stellar evolution (i.e. after SN). Each cut starts at the central star and moves either along the R-axis (dashed lines) or at a 45° angle (continuous lines) between the R- and Z-axes (see Fig. 2.1). The initial mass of the star in the simulation was 40 solar masses and case B corresponds to a local magnetic field strength of 5 μG in the interstellar medium.

the MF model.

In van Marle et al. (2015) the MF strength of simulated bubbles from a single OB star (40 solar masses) in different external MFs were computed (see van Marle et al., 2015, for further details). The resulting structure of the B_{RMS} can be seen in Fig. 2.5. The case where the outside MF strength is 5 μG is of most interest as this is most similar to the case of the local ISM. As the magnetic field in this thesis is assumed to be circular, we disregard the ϕ-dependence of the MF strength (i.e. angular dependence in the galactic plane, or xy-plane). Figure 2.5 also show that the B_{RMS} in the bubble barrier has a narrow peak at the inner side and then going over to a more constant and weaker field strength that is still stronger than the outside field. Inside the bubble the field is notably weaker than the field in or outside the barrier, of an order $\leq 10^{-2}$ of the barrier strength. To simplify the field in the barrier, one could assume a constant field in the barrier with the same integrated strength. In addition the width of the barrier could be made narrower as well in order to get a higher strength (while not exceeding the original maximum field strength).

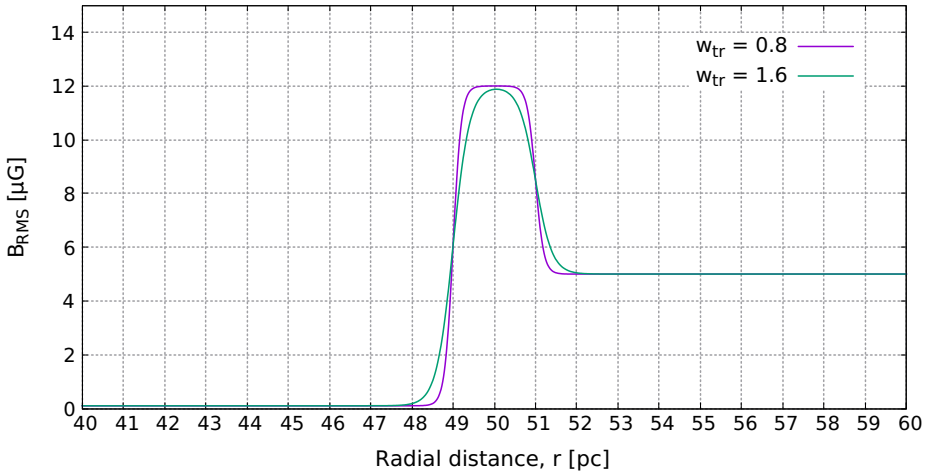

Figure 2.6: Plot showing the magnetic field strength, B_{RMS} of the model following equations (2.5) and (2.11). The bubble radius is set to 50 pc and the bubble width is set to 2 pc. The width of the bubble walls (w_{tr}) is set to 0.8 pc and 1.6 pc for the two respective plots.

Assuming for our toy model of the magnetic field that the field strength of the wall should be similar to the strength of the 5 μG case in Fig. 2.5, the B_{RMS} is set to follow:

$$B_{\mathrm{RMS}}(r) = \begin{cases} 0.1\,\mu\mathrm{G} & \text{if } r \leq r_{\mathrm{bubble}} - \frac{1}{2} w_{\mathrm{bubble}}, \\ 12\,\mu\mathrm{G} & \text{if } r_{\mathrm{bubble}} - \frac{1}{2} w_{\mathrm{bubble}} < r \leq r_{\mathrm{bubble}} + \frac{1}{2} w_{\mathrm{bubble}}, \\ 5\,\mu\mathrm{G} & \text{if } r > r_{\mathrm{bubble}} - \frac{1}{2} w_{\mathrm{bubble}}, \end{cases} \tag{2.11}$$

where r_{bubble} is the radius to the bubble barrier's center and w_{bubble} is the width of the bubble barrier. In addition, equation (2.5) is used for the transitions between the r-regions in eq. (2.11) with $r_0 = r_{\mathrm{tr}}$, i.e the respective transition radii of eq. (2.11), and w_{tr} (transition width) equal to a set value. The transition regions are hereby referred to as the inside and outside bubble walls.

As the Local Bubble in about 200 pc in diameter (of the "cylinder"), and the bubble in Fig. 2.5 is $\sim$ 50 pc in diameter for the 5 μG case, a superbubble of a scale size in between these would be an optimal starting point. A diameter of 100 pc for the MF toy model is therefore chosen, i.e. $r_{\mathrm{bubble}} = 50$ pc. As the MF strength of the barrier should be similar to Fig. 2.5, w_{bubble} is set to 2 pc. In order to have suitable, yet not too sharp, bubble walls a transition width (see. eq. (2.5)) $w_{\mathrm{tr}} = 0.8$ pc is chosen. A plot of the resulting B_{RMS} is shown in Fig. 2.6, including a plot of B_{RMS} with a transition width $w_{\mathrm{tr}} = 1.6$ pc (double of what is chosen). As one may see from the figure, in the case where $w_{\mathrm{tr}} = 1.6$ pc the transition width is so large that the B_{RMS} of the model only reach the maximum value of 12 μG fro a very short r-interval and the transition itself becomes so wide that it does not represent what is seen in Fig. 2.5.

For the model we assume the bubble barrier, i.e. the region with increased MF strength, is part of the bubble field and thus the transition between the inner (circular) field and the outer (constant) field is at the outer wall of the barrier, i.e. at $r = 51$ pc. Additionally, we assume the transition width between the inner and outer field is equal to that of the of the bubble barrier's walls, i.e. $w_{\mathrm{tr}} = 0.8$ pc.

2.1.2 Modelling the Turbulent Magnetic Field

The existence of a turbulent (or random) magnetic field in the ISM is widely agreed upon in the scientific community. However, what is less agreed upon is both the strength and correlation scale of the TMF, especially the latter. According to Sun et al. (2008), in the Galactic disc the TMF in the ISM has a RMS strength of 3 μG, but the authors say little about the correlation scale. There have been many attempts to characterize the TMF in the ISM or in SNR (e.g. see Rand and Kulkarni, 1989; Padoan et al., 2016), where the correlation scale has been varying from 10 pc to 250 pc for the TMF in the ISM.

Hydrodynamic turbulence is normally modelled as eddy currents of different scale sizes, where the energy of each eddy is depending on the eddy's scale size. Similarly, one can model a turbulent magnetic field as a Gaussian random field with zero mean and a RMS value B_{RMS} using superposition of Fourier modes (i.e. plane waves, or magnetic eddies) as

$$B_i(\boldsymbol{x}) = \int \frac{\mathrm{d}^3 k}{(2\pi)^3} B_i(\boldsymbol{k}) e^{i(\boldsymbol{k}\cdot\boldsymbol{x}+\phi_i(\boldsymbol{k}))}, \tag{2.12}$$

where $\boldsymbol{x}$ is the position vector, $B_i(\boldsymbol{x})$ is the magnetic field component in direction of $\hat{\boldsymbol{e}}_i$, $\boldsymbol{k}$ is the wave vector of the Fourier modes, and $\phi(\boldsymbol{k})$ are random phases (Harari et al., 2002, p. 3). Note that $|\boldsymbol{k}| = k = \lambda/2\pi$ were λ is the wavelength (or scale size) of each mode (i.e. magnetic eddy), and all wave vectors have random directions independent of each other. In order for this field to have zero divergence, see equation (2.2), the components $B_i(\boldsymbol{k})$ must be so that

$$\boldsymbol{B}(\boldsymbol{k}) \cdot \boldsymbol{k} = 0, \tag{2.13}$$

where

$$\boldsymbol{B}(\boldsymbol{k}) = B_x(\boldsymbol{k})\hat{\boldsymbol{e}}_x + B_y(\boldsymbol{k})\hat{\boldsymbol{e}}_y + B_z(\boldsymbol{k})\hat{\boldsymbol{e}}_z. \tag{2.14}$$

If the field is isotropic and homogeneous the random Fourier modes satisfy the relation

$$\langle \boldsymbol{B}(\boldsymbol{k}_i) \cdot \boldsymbol{B}^*(\boldsymbol{k}_j) \rangle = B^2(k_i)\delta(\boldsymbol{k}_i - \boldsymbol{k}_j). \tag{2.15}$$

Further, this makes it so that the root mean square value is

$$B^2_{\mathrm{RMS}} \equiv \langle \boldsymbol{B}(\boldsymbol{x}) \cdot \boldsymbol{B}^*(\boldsymbol{x}) \rangle = \int B^2(k)\mathrm{d}k. \tag{2.16}$$

Theoretical models suggest that the turbulent magnetic field follows a power law

$$E(k) \propto B^2(k) \propto k^{-\gamma}, \tag{2.17}$$

where $E(k)$ is the energy of a mode with $|\boldsymbol{k}| = k$, and γ is the spectral index of the power law ($\gamma = 5/3$ corresponding to Kolmogorov turbulence which is normal in hydrodynamic turbulence). We further assume that there is a maximum scale size at which the energy is fed into the turbulent system, and then the energy is transferred to smaller scale sizes until it reaches a point where it is lost to the surroundings (e.g. viscous heating of the charged particles creating the eddies). This is analogous to hydrodynamic turbulence. This makes it possible to find the energy of each eddy through the normalization of the field strength B_{RMS} (see Harari et al., 2002,

for more information):

$$B^2(k) = B^2_{\mathrm{RMS}} k^{-\gamma} \frac{(\gamma-1)k_{\mathrm{min}}^{\gamma-1}}{1-(k_{\mathrm{min}}/k_{\mathrm{max}})^{\gamma-1}}, \tag{2.18}$$

where the wave numbers of the turbulence is constrained by the limits $k_{\mathrm{min}} < k < k_{\mathrm{max}}$ (i.e. scale sizes $\lambda_{\mathrm{min}} < \lambda < \lambda_{\mathrm{max}}$)

For the toy model in this thesis, a single turbulent field is used both inside and outside the bubble to simplify the computation. Also, the largest scale size of the TMF is set to 10 pc , i.e. the lower limit of previous attempts to characterize the TMF in the ISM (Rand and Kulkarni, 1989). This is to make sure that the TMF does not have modes that is effectively constant over the whole bubble model, while also resulting in fewer modes needed in each computation (will be shown later).

Computational Algorithm

In order to compute a random turbulent magnetic field of the same form as the magnetic field in equation (2.12) this report follows the algorithm presented in Giacalone and Jokipii (1999). The algorithm in Giacalone and Jokipii (1999) computes a complex magnetic field through a superposition of Fourier modes, each with a random polarization and a random direction defined by two angles θ and ϕ. A three-dimensional realization of $\boldsymbol{B}(\boldsymbol{r})$ which satisfies equation (2.2) may be written

$$\boldsymbol{B}(\boldsymbol{r}) = \sum_{j=1}^{n_k} B(k_j)\boldsymbol{\zeta}_j e^{i(k_j z' + \beta_j)}, \tag{2.19}$$

where n_k is the number of modes, k_j is the the mode's wave number, and $B(k_j)$ is the amplitude of the respective mode and may be chosen to follow the desired power spectrum. $\boldsymbol{\zeta}_j$ is the polarization vector and is given by

$$\boldsymbol{\zeta}_j = \cos(\alpha_j)\hat{\boldsymbol{e}}_{x'} \pm i\sin(\alpha_j)\hat{\boldsymbol{e}}_{y'}. \tag{2.20}$$

Each wave propagates in its own z'-direction with polarization in the $x'y'$-plane, where the primed system is related to the unprimed system through the rotation

$$\boldsymbol{r'_{3D}} = R(\theta,\phi)\boldsymbol{r_{3D}}, \tag{2.21}$$

with rotation matrix

$$R(\theta,\phi) = \begin{pmatrix} \cos(\theta)\cos(\phi) & \cos(\theta)\sin(\phi) & -\sin(\theta) \\ -\sin(\phi) & \cos(\phi) & 0 \\ \sin(\theta)\cos(\phi) & \sin(\theta)\sin(\phi) & \cos(\theta) \end{pmatrix}, \tag{2.22}$$

where θ and ϕ are functions of k. It can easily be shown that the primed system is defined by orthonormal basis vectors. The phases α_j and β_j, and the sign $\pm$ in equation (2.20), chosen randomly, are responsible for the random polarization. Meanwhile the angles θ and ϕ gives the random propagation direction. This means that for any realization of the magnetic field, and for each k, there are five random numbers θ, ϕ, α, β, and s. The random numbers' possible values (i.e. the range) and probability distributions giving an isotropic and homogeneous field

Table 2.1: Properties of the random parameters for an isotropic field.

Parameter	Parameter range	Probability distribution
α	$0 < \alpha < 2\pi$	$p(\alpha) = 1/2\pi$
β	$0 < \beta < 2\pi$	$p(\beta) = 1/2\pi$
θ	$0 < \theta < \pi$	$p(\theta) = \sin(\theta)/2$
ϕ	$0 < \phi < 2\pi$	$p(\phi) = 1/2\pi$
s	$\{+,-\}$	$p(+) = 0.5,\ p(-) = 0.5$

are shown in Tab. 2.1.

It should be noted that the matrix in eq. (2.22) is specific for propagation in the z'-direction, and the probability distribution of the random numbers is necessary for an isotropic TMF. The rotation matrix as described in Giacalone and Jokipii (1999) is from an earlier article by the same authors (see Giacalone and Jokipii, 1994). Though the rotation matrices from the articles are equal (with a difference in $\theta \leftrightarrow -\theta$), the assumed propagation direction in the primed system (exponential in eq. (2.19)) is different: x' for Giacalone and Jokipii (1994) and z' for Giacalone and Jokipii (1999). By calculating the mean square value of ζ_j in each direction using the probability distribution of the parameters as shown in Tab. 2.1, one would get 1/3 for each direction with z' as the propagation direction of the field modes, but 5/12 in the x- and y-directions and 1/6 in the z-direction for x' as the propagation direction. As an isotropic field requires equal mean square value in any direction, i.e. $\langle \boldsymbol{\zeta}_j \cdot \boldsymbol{\zeta}_j^* \rangle = 1/3$ (see eqs. (2.15), (2.16) and (2.19)). Additionally, if one neglect the probability densities (i.e. use flat distributions, see Tautz (2012)) for the parameters and uses z' as the propagation direction, one would get $3/8 = 0.375$ for the mean square value of ζ_j in the x- and y-directions and $1/4 = 0.25$ in the z-direction which is not isotropic.

The wave numbers k_j are logarithmically distributed between $k_{\min}$ and $k_{\max}$ in order to give each decade in scale sizes equal weighting of k numbers. This is similar to an assumption for normal hydrodynamic turbulence, where eddies are modelled to transfer its energy into eddies of a smaller scale size with a constant scale ratio, resulting in logarithmically spaced scale sizes. Additionally, in order for the computed field to be approximately isotropic one need a minimum number of modes per decade, n_{dec}. This number increases with increasing spectral index of the power law as each new mode with equal logarithmic spacing gets an increasingly smaller magnetic strength than the last. In other words $B(k_j)/B(k_{j+1})$ $(k_j < k_{j+1})$ gets smaller when γ is increased and the field becomes more defined by the smaller k_j and their direction.

Normalization

The turbulent magnetic field strength should be normalized to the value B_{RMS}. Given that the TMF is isotropic, equations (2.22) and (2.20) show that $|\boldsymbol{\zeta}_j| = 1$. Now, if for any pair $\{\boldsymbol{k}_j, \boldsymbol{k}_l\}$ the total spatial size of the magnetic field $L_{MF} \gg 2\pi/|k_j - k_l|$, it may be shown for the Fourier modes that

$$\langle (\boldsymbol{\zeta}_j e^{i(k_j z'_j + \beta_j)}) \cdot (\boldsymbol{\zeta}_l e^{i(k_l z'_l + \beta_l)})^* \rangle = \delta(\boldsymbol{k}_j - \boldsymbol{k}_l). \tag{2.23}$$

Using this result and inserting equation (2.19) into (2.16) one gets

$$B_{\mathrm{RMS}}^2 = \sum_{j=1}^{n_k} B^2(k_j). \tag{2.24}$$

The desired power law for the turbulence is given by equation (2.17). Using the scale sizes of the Fourier modes one can rewrite the amplitude as

$$B(k) = B(k_{\mathrm{min}}) \left(\frac{k}{k_{\mathrm{min}}} \right)^{-\gamma/2}, \tag{2.25}$$

where $B(k_{\mathrm{min}})$ is the amplitude of the mode corresponding to the minimum wave number k_{min}, i.e. the largest turbulent structure. Inserting equation (2.25) into (2.24) one gets

$$B^2(k_{\mathrm{min}}) = \frac{B_{\mathrm{RMS}}^2}{\sum_{k_j} \left(\frac{k_j}{k_{\mathrm{min}}} \right)^{-\gamma}}, \tag{2.26}$$

and the square root of the r.h.s. gives the normalized value for $B(k_{\mathrm{min}})$. In the case where the field is not isotropic, equation (2.16) does not simply result in equation (2.24), and each mean value of $\langle \boldsymbol{B}(\boldsymbol{k}_i) \cdot \boldsymbol{B}^*(\boldsymbol{k}_j) \rangle$ would have to be calculated.

The magnetic field should be real. On the contrary, the field created by equation (2.19), and presumably (2.12), is complex. In order to acquire a real field, one only has to take the real part of the resulting field, but this will change the RMS value. Using $\boldsymbol{x} \cdot \boldsymbol{x}^* = \mathrm{Re}^2(\boldsymbol{x}) + \mathrm{Im}^2(\boldsymbol{x})$, equation (2.16) gives

$$B_{\mathrm{RMS}}^2 = \langle \boldsymbol{B}(\boldsymbol{r}) \cdot \boldsymbol{B}^*(\boldsymbol{r}) \rangle = \langle \mathrm{Re}^2(\boldsymbol{B}) \rangle + \langle \mathrm{Im}^2(\boldsymbol{B}) \rangle . \tag{2.27}$$

In addition, $\langle \mathrm{Re}^2(\boldsymbol{B}) \rangle = \langle \mathrm{Im}^2(\boldsymbol{B}) \rangle$ which may be acquired by taking the mean square of the real and imaginary part of $\boldsymbol{\zeta}$ times the exponent (see eq. (2.19). Now one simply gets

$$\langle \mathrm{Re}^2(\boldsymbol{B}) \rangle = \frac{1}{2} B_{\mathrm{RMS}}^2. \tag{2.28}$$

In order to make only the real part of the computed B-field to have a RMS value equal to B_{RMS} one only needs to multiply $B(k_{\mathrm{min}})$ with $\sqrt{2}$. The new equations for the turbulent magnetic field would then be

$$\boldsymbol{B}(\boldsymbol{r}) = \mathrm{Re} \left\{ \sum_{k_j} B(k_j) \boldsymbol{\zeta}_j e^{i(k_j z' + \beta_j)} \right\}, \tag{2.29}$$

$$B(k_{\mathrm{min}}) = B_{\mathrm{RMS}} \left(\frac{2}{\sum_{k_j} \left(\frac{k_j}{k_{\mathrm{min}}} \right)^{-\gamma}} \right)^{1/2}, \tag{2.30}$$

with equation (2.25) staying the same.

2.2 Magnetic Scattering

The net force on a charged particle moving through an electromagnetic field is given by the Lorentz force law (Griffiths, 2014, p. 212, p. 542):

$$\boldsymbol{F}_L = \frac{\mathrm{d}\boldsymbol{p}}{\mathrm{d}t} = q\left(\boldsymbol{E} + \boldsymbol{v} \times \boldsymbol{B}\right), \tag{2.31}$$

where $\boldsymbol{E}$ and $\boldsymbol{B}$ are respectively the electric and magnetic fields, $\boldsymbol{v}$ is the particle velocity, q is the particle's electric charge, and $\boldsymbol{p}$ is the particle momentum. Newtons second law retains its validity in relativistic mechanics (Griffiths, 2014, p. 542) as long as one uses the relativistic momentum given by the equation (Griffiths, 2014, p. 535)

$$\boldsymbol{p} = \gamma_L m \boldsymbol{v}, \tag{2.32}$$

where m is the particle mass and γ_L is the (relativistic) Lorentz factor

$$\gamma_L = \frac{1}{\sqrt{1 - \frac{v^2}{c^2}}} = \frac{E}{mc^2}, \tag{2.33}$$

where E is the energy of the particle. Using eq. (2.32), eq. (2.31) can easily be rewritten for either $\boldsymbol{p}$ or $\boldsymbol{v}$. In the case of a zero electric field ($\boldsymbol{E} = \vec{\boldsymbol{0}}$) the acceleration of the particle due to the Lorentz force will be perpendicular to the magnetic field lines and the particle velocity. With no acceleration in the direction of the velocity, the kinetic energy of the particle is conserved. In circular motion the acceleration a is $a = v_\perp^2 / r$, where $v_\perp$ is the particle velocity perpendicular to the acceleration and r is the radius. Using this and equation (2.31) in the case of a constant magnetic field with straight field lines the charged particles move in helical motion around the field lines with gyroradius R_g, a.k.a. the Larmor radius, given by

$$R_g = \frac{p_\perp}{|q|B}. \tag{2.34}$$

The relativistic energy of a particle is $E = \gamma_L mc^2$, with c being the speed of light in vacuum. Further one may use that the charge of the particle is a sum of elementary charges e, $|q| = Ze$ where Z is an integer, so that the gyroradius may be written

$$R_g = 1.081 \cdot 10^{-3}\mathrm{pc}\frac{\beta_\perp}{Z}\frac{E}{10^{18}\mathrm{eV}}\frac{\mathrm{G}}{B}, \tag{2.35}$$

where $\beta_\perp = v_\perp / c$.

For a particle propagating through a turbulent magnetic field, one may define the gyroradius of the particle through equation (2.35) using the RMS value of the magnetic field strength, i.e. $B = B_{\mathrm{RMS}}$. If the gyroradius of the particle $R_g \ll \lambda_c$, i.e. the correlation length of the field, the particle would experience the magnetic field to be approximately constant with parallel field lines on a scale size of the same order as the gyroradius. One would then expect the propagation motion of the particle to be similar to a helical motion following the magnetic field lines. In the opposite case where $R_g \gg \lambda_c$ the magnetic field change so rapidly so that the particle would not "see" the details of the magnetic field. The particle motion would then primarily depend on the

mean value of the field $\langle \boldsymbol{B} \rangle$. If the mean value is zero, one would expect the turbulence to induce small (tiny) deviations from a straight particle trajectory over scale lengths $\sim \lambda_c$.

Caprini and Gabici (2015) give two equations for the deflection angle of electrons/positrons propagating through a turbulent magnetic field that is statistically homogeneous and isotropic. The deflection angle δ is set to depend on five parameters, namely the distance propagated D, the magnetic field's correlation length L_c, the Larmor radius, i.e. the gyroradius R_g, and two spectral indices (n_B, m_B) of a power law given by

$$P_B(k) = B^2(k) \cdot k^2 = A \begin{cases} \left(\frac{k}{k_0}\right)^{n_B} & \text{if } k \leq k_0 \\ \left(\frac{k_0}{k}\right)^{m_B} & \text{if } k > k_0 \end{cases} \tag{2.36}$$

where A is a normalization constant and k_0 correspond to a characteristic scale size $\lambda_B = 2\pi/k_0$. Further they assume $m_B = 11/3$, which here corresponds to Kolmogorov turbulence, and vary n_B.

In the two cases where the propagation distance $D \ll \lambda_B$ and $D \gg \lambda_B$ one gets for the RMS value of the deflection angle (Caprini and Gabici, 2015)

$$\sqrt{\langle \delta^2 \rangle} \simeq \frac{2}{\sqrt{3}} \frac{D}{R_g} \quad \text{if } D \ll \lambda_B, \tag{2.37}$$

$$\sqrt{\langle \delta^2 \rangle} \simeq \frac{\sqrt{D\lambda_B}}{R_g} \cdot \Pi\left(\frac{D}{\lambda_B}, n_B\right) \quad \text{if } D \ll \lambda_B, \tag{2.38}$$

where

$$\Pi\left(\frac{D}{\lambda_B}, n_B\right) = \left[\left(\frac{\lambda_B}{D}\right)^{n_B+2} \left(\frac{(n_B+1)\Gamma(n_B+4)\sin\left(n_B\frac{\pi}{2}\right)}{\pi^2(2\pi)^{n_B+1} n_B(n_B+2)^2(3n_B+11)}\right) + \frac{n_B+3}{10n_B+20} + \mathcal{O}\left(\frac{\lambda_B}{D}\right)^3\right]^{\frac{1}{2}}. \tag{2.39}$$

A plot of equation (2.39) is shown in Fig. 2.7. One can see from the figure that $\Pi(D/\lambda_B, n_B)$ is generally increasing in value with increasing D, and that for values of $n_B > 0$ becomes approximately constant at $D > \lambda_B$. The value of this scalar is depending on n_B itself, but for $n_B \gg 1$ one see that $\Pi(D/\lambda_B, n_B) \to 10^{-1/2}$ for propagation distances $D > \lambda_B$. Aharonian et al. (2010) considered the same power law of a TMF as Caprini and Gabici (2015), but through different mathematical derivation got a function for Π in the limit $D \gg \lambda_B$ given by

$$\Pi\left(\frac{D}{\lambda_B} \gg 1, n_B\right) = \left[\frac{(m_B-3)(n_B-1)}{4(m_B-2)(n_B-2)}\right]^{\frac{1}{2}}, \tag{2.40}$$

which for $m_B = 11/3$ (Kolmogorov turbulence) and $n_B \gg 2$ gives the same result as found above ($\Pi \approx 10^{-1/2}$). In addition to the two sources above, Harari et al. (2002) considered a case where there is a higher limit $k_{\max}$ (lower scale limit) to the power spectrum. If the $k_{\max}$ value is of many orders larger than $k_{\min} = 2\pi/\lambda_B$, this would be equivalent to the above cases, and one would have $\Pi(D/\lambda_B \gg 1) \approx 10^{-1/2}$. In the case where $k_{\max} \to k_{\min}$ the correlation length λ_c of the field

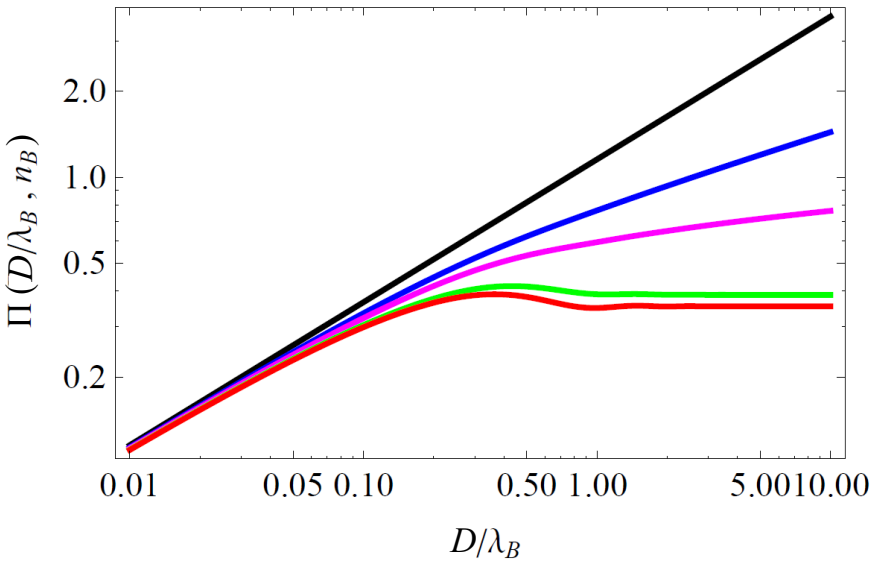

Figure 2.7: The function $\Pi(D/\lambda_B, n_B)$ defined in eq. (2.39) for different values of the large scale spectral index n_B: from top to bottom $n_B \to -3$ (black), $n_B = -2.5$ (blue), $n_B = -2$ (magenta), $n_B = 0$ (green), $n_B = 2$ (red). From Caprini and Gabici (2015)

changes with respect to λ_B like

$$\lambda_c = \frac{1}{2}\lambda_B \frac{\gamma - 1}{\gamma} \frac{1 - (k_{\min}/k_{\max})^{\gamma}}{1 - (k_{\min}/k_{\max})^{\gamma-1}}, \tag{2.41}$$

which for Kolmogorov turbulence in the limit $k_{\max} \to \infty$ gives $\lambda_c = \lambda_B/5$, and for $k_{\max} \to k_{\min}$ gives $\lambda_c = \lambda_B/2$. Thus the value of $\Pi(D/\lambda_B \gg 1) \to 0.5$ in the limit where $k_{\max} \to k_{\min}$. For more detail of the derivations, see the respective articles (Caprini and Gabici, 2015; Aharonian et al., 2010; Harari et al., 2002). There are no specific expression for the RMS of the deflection angle in the interval where $D \sim \lambda_B$ as this is the most difficult region to characterize.

In our model of the turbulent magnetic field the power law starts at a minimum wave number $k_{\min}$ corresponding to a maximal scale size of the turbulence. The power law then falls of with increasing k equivalent to Kolmogorov turbulence ($\gamma = 5/3$), see equation (2.17), to a maximum $k_{\max}$ (i.e. minimum scale size of the turbulence). This power law is equivalent to eq. (2.36) with $n_B \to \infty$ and a cutoff at $k_{\max} > k_0$, where $k_0 = k_{\min}$. Note the difference in γ vs. m_B as the power law in Caprini and Gabici (2015) is $P(k) = E(k)k^2 \propto k^{-m_B}$, while our is defined through $E(k) \propto k^{-\gamma}$ (i.e. $m_B = \gamma + 2$). To find the error of a normalization of the TMF going from $k_{\min}$ to $k_{\max}$ rather than $k \to \infty$, one may use eq. (2.18). By setting $k_{\min} = 1$, $B_{\mathrm{RMS}} = 1$ and choosing a set $k_{\max} \to \infty$, an integral over k of eq. (2.18) from $k = k_{\min}$ to $k = k_{\max} \to \infty$ is through definition equal to 1. Doing the same integral with a finite upper limit $k_{\max}$ gives the relative MF energy ($E \propto B^2$) residing in the turbulence with $k \leq k_{\max}$. Calculations give for the first 6 decades 0.99990 = 99.990% of the MF energy, while for 11 decades it is as good as 1.

Assuming that one has a charged particle inside a turbulent magnetic field as described by our model. Further assume that the gyroradius, as described in eq. (2.35), is such that it is much smaller than the largest scale size of the turbulence, but still (much) greater than the smallest

scale size, i.e. $2\pi/k_{\max} \ll R_g \ll 2\pi/k_{\min}$. For propagation distances $D \sim R_g$ one has three cases of deflection. The first case is for the turbulence modes with $\lambda = 2\pi/k \gg R_g$. These modes change so slowly over the propagation distance that the combined field of these modes is approximately constant, and the particle moves along the field lines of these modes with deflection angle proportional to the distance propagated. The second case is that of the turbulence modes with $\lambda \ll R_g$. These modes change so fast that one effectively get small angle scattering that creates small wriggles on the larger deflections. These small deflections effectively average out over longer propagation lengths, and we can therefore neglect them in the numerical computations. The third case is for the turbulence scales where $\lambda \sim R_g$. As mentioned earlier the deflections where $D \sim \lambda_B$ are hard to describe, but they are still large and will therefore have to be included in the numerical computations.

2.2.1 Computation Method for the Particle Trajectories

To solve the ordinary differential equation (ODE) that is the equation of motion (EOM), described in eq. (2.31), we use a Runge-Kutta (RK) solver as described in Press et al. (1997, ch. 16.2). The code has an adaptive stepsize control with error estimation in order to perform the propagation with smallest possible running time.

The described computational algorithm of the TMF, see section 2.1.2, uses a set number of modes per decade (n_{dec}). In order to solve the EOM, the RK solver has to compute the magnetic field at many positions. While the regular field (i.e. not the TMF) is fast to calculate, the calculation of the TMF requires several computation steps for each mode, making it substantially slower. This makes the computation time of the particle trajectories proportional to the number of modes used. As argued in the end of the previous section, modes with $\lambda = 2\pi/k \ll R_g$ of the particle will have their contributions averaged out over longer propagation distances. Of this reason we chose to disregard these modes in the trajectory computations, but one still has to include them for the normalization of the field. We chose to draw the line at $\lambda = R_{g,\min}/3$, where $R_{g,\min}$ is the smallest gyroradius of the particle anywhere in the model (i.e. in the bubble barrier where $B_{\text{RMS}} = 12\ \mu$G). One third in scale size correspond to approximately half a decade in wave numbers. Even though the minimum gyroradius of the whole TMF ($R_{g,\min}$) is slightly larger than the scale size of the modes we disregard, the gyroradius w.r.t. only the turbulence of scale sizes $< R_{g,\min}/3$ gets even smaller as $R_{g,\min}$ decreases, because the modes contribute less to the total (constant) B_{RMS} (see eq. (2.35)). For high particle energies where $R_{g,\min} > 2\pi/k_{\min}$ the number of modes is set to be equal to that of half a decade, in order to have a non-vanishing TMF with some degree of isotropy.

Particles with lower energies will have smaller gyroradii than higher energy particles. This leads to larger deflections, which when solving the EOM demands higher precision of the RK solver and therefore more time. Additionally, as lower energy particles require more modes total (due to more decades), the computation time gets even longer for these particles compared to higher energies. One could use the same number of modes for all particles, i.e. regulate the number of modes per decade, but this would not give the opportunity to test particles with different energies in the same fields. If the number of modes per decade has to be reduced to a number no longer sustaining an approximately isotropic field, a solution is to run the trajectories with more realizations of the TMF, and would be comparable to a TMF changing in time, rather than the time independent TMFs that are computed. This will also lead to better aver-

aged statistics, although one loose information of the individual TMFs, assuming the same total number of trajectories is used.

In De Marco et al. (2007) the authors tried to describe the propagation of high energy cosmic rays in the Galaxy using numerical techniques. They modelled the TMF using 100 modes per decade in order to have reasonable computation time. Their result was a TMF with anisotropy. With access to more computational power, we have the possibility to compute TMFs with 1 000 modes per decade (or more) for most energies, possibly solving the anisotropy problem of the TMF.

According to Haverkorn and Spangler (2013) the dissipation scale in the ISM turbulent magnetic field is of order $50-250$ km, which compared to 10 pc is of magnitude $10^{-11}-10^{-12}$. In comparison, 1 AU is of order $5\cdot10^{-6}$ that of 1 pc, so one only makes a small error by normalizing from 10 pc to turbulence scales of $1-10$ AU than to ~ 100 km as we have shown earlier in Sec. 2.2. Using eq. (2.35) one find for a proton with energy $E = 1.0\cdot10^{13}$ eV inside the MF model barrier with $B_{\mathrm{RMS}} = 12$ μG that the gyroradius $R_g \approx 9.0\cdot10^{-4}$ pc ≈ 180 AU. This particle energy is the smallest used in the computations, as we want to stay at energies $\gg E_0 = mc^2$ to ensure that the particles are highly relativistic ($\gamma_L \gg 1$). Setting the lower limit of the turbulence scale sizes to 10 AU (5.3 decades from 10 pc) results in a relative error of $2.9\cdot10^{-4}$ in the total energy of the TMF w.r.t. lower scale size equal to ~ 100 km. This we view as an acceptable approximation, and the TMF is normalized from 10 pc to 10 AU.

2.3 Diffusion, Ballistic Motion, and Curve Fitting

In the propagation of the cosmic rays we will be looking at two cases. In the first case we will be looking at a continuous source of VHE protons at the center of the bubble, and then trace the particles until they reach an arbitrary distance in the xy-plane from the origin where they are considered to be lost. In the second case we assume a burst of VHE protons at the origin and trace the protons for a given amount of time. The protons with the highest energies will have gyroradii that are (much) larger than the bubble diameter, and will consequently have a behaviour close to ballistic particles, i.e. moving in straight lines. For the smallest energies, even inside the bubble where the R_g is at its maximum, it will still be much smaller than the bubble radius. In a purely turbulent field they would be expected to have a diffusive behaviour.

First we look at a bursting source case and with ballistic particles. Assuming the particles are emitted isotropically form the origin, i.e. the unit momentum vectors are evenly distributed on the unit sphere, the radius r of the particles position in the xy-plane after a time t_p is

$$r = R_p \sin(\theta), \tag{2.42}$$

where $R_p = v t_p \simeq c t_p$ is the total distance propagated and θ is the angle between the z-axis and the propagation direction. For an isotropic distribution the angle between the z-axis and the position vector, θ (a.k.a. the zenith angle), has a defined value $0 \le \theta \le \pi$ and it has the probability distribution $f(\theta) = \sin(\theta)/2$, while the angle ϕ in the xy-plane is distributed evenly between 0 and 2π. As $\sin(\theta) = \sin(\pi-\theta)$ one also gets $r(\theta) = r(\pi-\theta)$. If we have isotropy, the particles will be evenly distributed on a sphere of radius R_p after a time t_p has passed. The area

of a ring of the spherical shell between θ and $\theta + \mathrm{d}\theta$ is

$$2\pi R_p \sin(\theta)\mathrm{d}\theta. \tag{2.43}$$

The area of the projected spherical shell onto the xy-plane is simply

$$2\pi R_p \sin(\theta)\mathrm{d}r, \tag{2.44}$$

with the relation $\mathrm{d}r = \cos(\theta)\mathrm{d}\theta$. As the contribution to particle density w.r.t. the xy-plane is equal for θ and $\pi - \theta$ (over and under the plane), we only have to look at θ above the xy-plane ($0 \leq \theta \leq \pi/2$) and normalize accordingly. As the number density of particles is proportional to the area of the shell (i.e. constant density per area), and we have the relation between the area of a cut of the shell ($\mathrm{d}\theta$, see eq. (2.43)) and its projection onto the xy-plane (see eq. (2.44)), we get for the number density in the xy-plane for ballistic particles

$$n_b(r,\phi) \propto \frac{\mathrm{d}A_{\text{shell}}}{\mathrm{d}A_{\text{plane}}} = \frac{2\pi R_p \sin(\theta)\mathrm{d}\theta}{2\pi R_p \sin(\theta)\mathrm{d}r} = \frac{1}{\cos(\theta)} = \frac{1}{\sqrt{1-\frac{r^2}{R_p^2}}}. \tag{2.45}$$

This can be normalized for the particles as $0 \leq r \leq R_p$ (Rottmann, 2003, ch. 10, eq. 51), and we get

$$n_b(r,\phi) = \begin{cases} \frac{2}{\pi R_p}\frac{1}{\sqrt{1-\frac{r^2}{R_p^2}}} & \text{if } 0 \leq r \leq R_p, \\ 0 & \text{otherwise.} \end{cases} \tag{2.46}$$

Equation (2.46) can also easily be rewritten for propagated time instead of propagated distance.

Now looking at the lower energy case of a bursting source. If one assumes diffusion for the particles the probability density function at a given time and in any direction is a Gaussian distribution

$$g(\boldsymbol{x}) = \frac{1}{\sqrt{2\pi}\sigma}\exp\left(\frac{-x^2}{2\sigma^2}\right), \tag{2.47}$$

where $x = |\boldsymbol{x}|$ and σ is the standard deviation (STD) in the given direction defined by

$$\sigma^2 = 2Dt, \tag{2.48}$$

where D is the diffusion coefficient and t is the time that the particles have diffused (or propagated). In the model of the bubble field we have assumed cylindrical symmetry, so we may assume $\sigma_x = \sigma_y$, and eq. (2.47) may be written for r as

$$g_r(r,\phi) = g_x(x) \cdot g_y(y) = \frac{1}{2\pi\sigma_x^2}\exp\left(\frac{-r^2}{2\sigma_x^2}\right), \tag{2.49}$$

which is the probability density in the xy-plane where σ_x is the 1D STD (in x- or y-direction). For particle diffusion one also has

In the case where we trace particles until they reach an arbitrary distance (in r) away from the origin, one will end up tracing the particles for different amounts of time. Consequentially,

one will then loose details of the particle trajectories at specific times, but gain other information concerning timing properties which we will now look at.

Going back to the case where the particles are traced for a certain amount of time. One may use the probability density functions to calculate the time accumulated probability density $\tau(r)$, i.e. the relative amount of time spent by all particles inside an area $\mathrm{d}A$ (or volume $\mathrm{d}V$), by integrating the probability density functions for the particles at any given r over time. First, looking at the ballistic case using $R_p \simeq ct$, we integrate eq. (2.46) from 0 to t_f and divide the result on t_f:

$$\begin{aligned}\tau_b(r,t_f) &= \frac{1}{t_f}\int_0^{t_f} n_A(r,\phi)\mathrm{d}t = \frac{2}{\pi c t_f}\int_{t_0}^{t_f}\frac{\mathrm{d}t}{t\sqrt{1-\frac{r^2}{c^2t^2}}} \\ &= \frac{2}{\pi c t_f}\int_{t_0}^{t_f}\frac{\mathrm{d}t}{\sqrt{t^2-\frac{r^2}{c^2}}} = \frac{2}{\pi c t_f}\ln\left[\frac{t_f+\sqrt{t_f-\frac{r^2}{c^2}}}{t_0+\sqrt{t_0-\frac{r^2}{c^2}}}\right].\end{aligned} \tag{2.50}$$

We recognize $t_f = R_f/c$ and $t_0 = r/c$, i.e. the time it takes for the first particles to reach r, which simplifies eq. (2.50) to

$$\tau_b(r,t_f) = \frac{2}{\pi R_f}\ln\left[\frac{R_f}{r}+\sqrt{\frac{R_f}{r}-1}\right] \quad \text{if } 0 \le r \le R_f. \tag{2.51}$$

This integration over time in not very helpful when dealing with bursting sources, as the probability density of the particle position is defined momentarily in time. Instead it becomes very helpful for continuous sources of CRs, where we have no information on when the particles was ejected from the source, but may have knowledge of the potential lifetime of the particles. The particle density may therefore be described by the integrated probability density of a bursting source from $t_0 = 0$ to the lifetime of the particles (i.e. t_f).

Another case for continuous sources is if one has a system with finite borders, and one wants to characterize the probability density of particles inside the system. If one has a constant source of CRs, the system will be in a steady state if the loss of particles (at the system borders) are equal to the ejection rate from the source. Given a mean escape time of the particles, one may calculate the total number of particles, and using the probability density one would get the particle density. The difference from e.g. eq. (2.51) is that now one would only add up the time for the particles still inside the borders of the system, and consequently the resulting probability density is only valid inside the borders of the system.

If the particles are ballistic and one traces them to an arbitrary radius $R_{\max}$, it is easy to show that the time spent in a given r-interval of length $\mathrm{d}r$ is the same for a single particle, i.e. the relative time a particle spend inside dr compared to the propagation time of the particle is equal for all particles, as long as each particle is allowed to reach $R_{\max}$ ($t_f \to \infty$). The relative amount of time spent by all particles in $r \to r+\mathrm{d}r$ ($n_r(r)$) will then be constant, and the probability

density w.r.t dA is simply

$$\begin{aligned} \tau_b(r) &\propto \frac{\mathrm{d}r}{\mathrm{d}A} = \frac{\mathrm{d}r}{2\pi r \mathrm{d}r} \Longrightarrow \\ \tau_b(r) &= Ar^{-1} \quad \text{if} \;\; 0 \leq r \leq R_{\max}, \end{aligned} \tag{2.52}$$

where A is a normalization constant. Through integration of $\tau_b(r)$ over $\mathrm{d}A = r\mathrm{d}r\mathrm{d}\phi$ it is easily shown that

$$A = \left[\int r^{-1}\mathrm{d}A\right]^{-1} = \frac{1}{2\pi R_{\max}}. \tag{2.53}$$

It is worth noting that eq. (2.52) is not possible to normalize for $r \to \infty$, as A would in this case have to go to zero. This is what one would expect for particles propagating for infinite amount of time, where the partial time spent in a small (or any finite area) would go to zero. With isotropic emission ($n(\theta) = \sin(\theta)/2$) of ballistic particles from the origin, the mean length $\langle L_{\text{bal}} \rangle$ of the trajectories out to a given limit radius r_{limit} is

$$\langle L_{\text{bal}} \rangle = \int_0^{\pi} \frac{\sin(\theta)}{2} \frac{r_{\text{limit}}}{\sin(\theta)} \mathrm{d}\theta = \frac{\pi r_{\text{limit}}}{2}, \tag{2.54}$$

giving a mean propagation time to the limit

$$\langle t_{\text{limit}} \rangle = \frac{\langle L_{\text{bal}} \rangle}{v} = \frac{\pi r_{\text{limit}}}{2c}, \tag{2.55}$$

where the particle speed $v \approx c$ for highly relativistic particles.

Considering the diffusion case for a given propagation time t_f. Performing the same integration for eq. (2.49) as for eq. (2.46) in (2.51), using the relation in eq. (2.48), one gets

$$\begin{aligned} \tau_d(r, t_f) &= \frac{1}{t_f} \int_0^{t_f} g_r(r, \phi) \mathrm{d}t = \frac{1}{t_f} \int_0^{t_f} \frac{1}{4\pi D t} \exp\left(\frac{-r^2}{4Dt}\right) \mathrm{d}t \\ &= \frac{1}{4\pi D t_f} \int_0^{t_f} \frac{\exp\left(\frac{-r^2}{4Dt}\right)}{t} \mathrm{d}t = \frac{1}{4\pi D t_f} \Gamma\left(0, \frac{r^2}{4Dt_f}\right), \end{aligned} \tag{2.56}$$

where Γ is the upper incomplete gamma function defined by (NIST, 2017, eq. (8.2.2))

$$\Gamma(z, a) = \int_a^{\infty} x^{z-1} e^{-x} \mathrm{d}x. \tag{2.57}$$

In the limit $z \to 0$ eq. (2.57) can be approximated to (NIST, 2017, eqs. (6.6.2) and (8.4.4))

$$\Gamma(0, a) = -\gamma_{EM} - \ln(a) - \sum_{k=1}^{\infty} \frac{(-a)^k}{k(k!)}, \tag{2.58}$$

where γ_{EM} is the Euler-Macheroni constant (NIST, 2017, eq. (5.2.3))

$$\gamma_{EM} = \lim_{n \to \infty} \left(1 + \frac{1}{2} + \frac{1}{3} + \frac{1}{2} + \ldots + \frac{1}{n} - \ln(n)\right) = 0.57721\,56649\,01532\,86060\ldots. \tag{2.59}$$

Attempting to find a function describing the probability density for diffusion of particles from a continuous source out to an arbitrary distance (i.e. a system with borders) is much more complicated. One would have to perform the time integral of the Gaussian distribution (eq. (2.49)) from $t = 0$ to an arbitrary large time $t_f \to \infty$, while only including the particles that are still inside $r < R_{\max}$ (as argued earlier earlier). One now gets

$$\begin{aligned}
\tilde{\tau}_d(r, t_f) &= \frac{\int_0^{t_f} g_r(r,\phi)\mathrm{d}t}{\int_0^{t_f}\left[\int_0^{2\pi}\int_0^{R_{\max}} g_r(r,\phi) r\,\mathrm{d}r\,\mathrm{d}\phi\right]\mathrm{d}t} \\
&= \frac{\frac{1}{4\pi D}\Gamma\left(0, \frac{r^2}{4Dt_f}\right)}{\int_0^{t_f}\left[1-\exp\left(\frac{-R_{\max}^2}{4Dt}\right)\right]\mathrm{d}t} \\
&= \frac{\frac{1}{4\pi D}\Gamma\left(0, \frac{r^2}{4Dt_f}\right)}{\left[1-\exp\left(\frac{-R_{\max}^2}{4Dt_f}\right)\right]t_f + \frac{R_{\max}^2}{4D}\Gamma\left(0, \frac{R_{\max}^2}{4Dt_f}\right)} \\
&= \frac{\tau_d(r, t_f)}{\left[1-\exp\left(\frac{-R_{\max}^2}{4Dt_f}\right)\right] + \frac{R_{\max}^2}{4Dt_f}\Gamma\left(0, \frac{R_{\max}^2}{4Dt_f}\right)}.
\end{aligned} \tag{2.60}$$

Note the difference between $\tilde{\tau}_d$ in eq. (2.60) and τ_d in eq. (2.56). Whereas τ_d considers particles at all values of r, $\tilde{\tau}_d$ only consider those where $r \leq R_{\max}$.

2.3.1 Fit-Functions

Both eqs. (2.60) and (2.56) are complicated and hard to use when fitting curves to a data plot. As eq. (2.58) rely on an infinite sum which one needs to compute to a certain precision for every value of a. The computational program used for curve fitting in this thesis reached a limit at $k \approx 120$. This makes $\Gamma(0, a)$ suddenly change in value as a approach the maximum value of k in the series expansion, making it not appropriate to use for curve fitting. Instead of fitting using eqs. (2.56) and (2.60), we use an other function:

$$f(r) = A \cdot r^d \cdot \exp\left(\frac{-\mathrm{r}^2}{2\sigma^2}\right), \tag{2.61}$$

where A is an amplitude parameter, and d and σ are other fitting parameters. The r^d is inspired by the ballistic cases and the exponent is proportional to a Gaussian distribution. In Fig. 2.8 the fit-function $f(r)$ (eq. (2.61)) is fitted against $\tau_d(r, t_f)$ (eq. (2.56)) for two values of t_f. One can see from the plots that the fit-function is a good substitute for $\tau_d(r, t_f)$ in the range of the fit. Additionally, one can see that σ in eq. (2.61) behave closely to $\sqrt{2Dt}$ in eq. (2.56), as should be expected as both are based on the Gaussian distribution.

To fit the probability density at a given time t we use the following function:

$$g(r) = \frac{A}{\sqrt{1-\frac{r^2}{R_m}}}\exp\left(\frac{-\mathrm{r}^2}{2\sigma^2}\right), \tag{2.62}$$

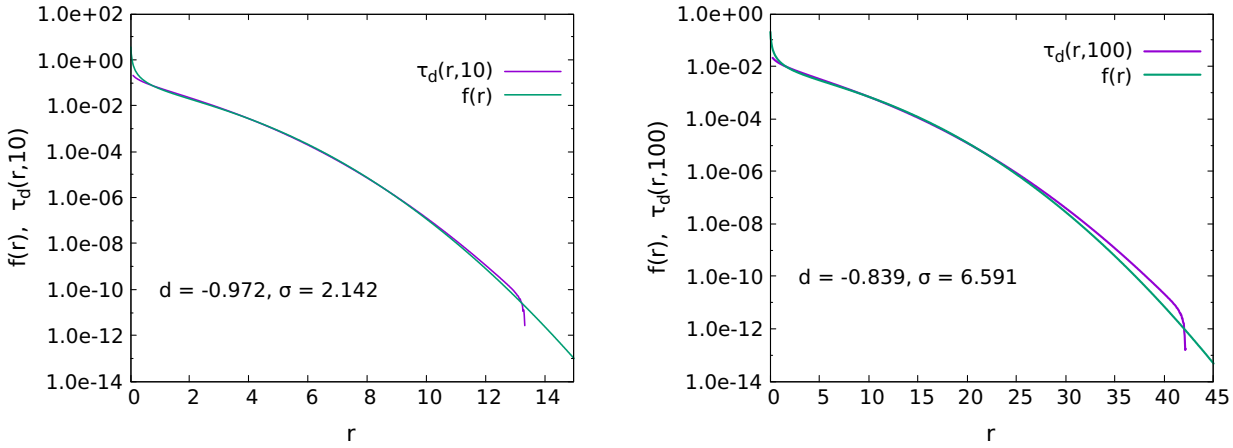

Figure 2.8: Plots of $\tau_d(r,t_f)$ (eq. (2.56)) and a fitted curve $f(r)$ (eq. (2.61)). The fitting parameters d and σ of $f(r)$ is shown in each plot. Left: $4Dt_f = 10$ (unit less length), and the fit-function $f(r)$ is fitted to values of $\tau_d(r,t_f)$ from $r = 0.5$ to 10 with increments of 0.5. In the curve fitting, each point was given an error estimate of one tenth (1/10) its value. Right: $4Dt_f = 100$ (unit less length). $f(r)$ was fitted in the same manner as in the left plot, with data points of $\tau_d(r,t_f)$ from $r = 1$ to 40 with increments of 1.

where A is an amplitude parameter, and R_m and σ are other fitting parameters. The function is inspired by the density functions of a Gaussian distribution and a ballistic distribution, see eqs. (2.46) and (2.49).

When analyzing the time and position data from the trajectory simulations, we will fit using the function in eq. (2.61) for constant CR sources, and the function in eq. (2.62) for bursting sources. We define the following 4 cases for the curve fitting:

1. Using $f(r)$ with all fitting parameters, i.e. A, d, and σ.

2. Using $f(r)$ with $d = 0$, i.e. only Gaussian diffusion is considered. Fitting parameters: A and σ.

3. Using $f(r)$ with $\sigma \to \infty$, i.e. assuming a "ballistic" case with no Gaussian diffusion. Fitting parameters: A and d.

4. Using $g(r)$ with all fitting parameters, i.e. A, R_m, and σ.

Chapter 3

Results and Discussion

3.1 Small Angle Deflections

Initially, the computation of the turbulent magnetic field was tested to see whether or not the field would give the same result for small angle scattering, as predicted by eq. (2.38). Setting the spectral index of the power law $\gamma = 5/3$ (eq. (2.17)) to match Kolmogorov turbulence, a number of field realizations were computed with 1000 modes per decade. Further, for each field realization 50 protons were injected at a random position within a sphere with radius 1000 times the largest turbulence scale size ($L_{\max}$, or λ_B), initially set to 10 pc. Each proton was given an isotropic starting momentum, i.e. $\hat{\boldsymbol{p}}$ evenly distributed on the unit sphere, and an energy corresponding to a gyroradius $R_g = 10\,000\,\lambda_B$ (e.g. $E \approx 10^{19}$ eV for $B_{\mathrm{RMS}} = 0.1$ μG). Then the protons were traced for a total propagation distance of 300 λ_B and along the way the RMS deflection angle δ_{RMS} was sampled. As the total number of modes determines the computation time of the simulations, the number of decades had to be restricted. As both the R_g and the distance propagated D are given in units of λ_B, eq. (2.38) simplifies.

Figure (3.1) shows the results of RMS deflection angles for many TMF realizations with different values for the TMF parameters. One using 2 decades with $n_{\mathrm{dec}} = 1000$ and a total of 6000 trajectories, the second also using only 0.5 decades with $n_{\mathrm{dec}} = 1000$ and 4800 trajectories, while the third having no decades $k_j = k_{\min}$, but having 2000 modes. We see that δ_{RMS} is approximately twice as large as the expected theoretical values from Caprini and Gabici (2015). We would expect the results from the realization with 0 decades to be close to the maximum value predicted by Harari et al. (2002) (for a small number of decades), but this is however not the case as it is the other deflections that approximate this theoretical maximum. Why the values are larger than the theoretical ones are not easily explained, but it might have to do with the precision of the computation, either having too few modes or possibly errors originating in the solving of the EOM. Further, the results also show that the δ_{RMS} is larger for a decreasing number of decades, as is expected by Harari et al. (2002). In addition, the δ_{RMS} values are following the theory with respect to $\Pi(D/\lambda_B, n_B \gg 2) \approx$ constant. With respect to our regular field model ($\lambda_B = 10$ pc), the range at which $\Pi(D/\lambda_B)$ is approximately constant is at least $300\lambda_B = 3\,000$ pc (about the width of the halo component of the Galactic MF, De Marco et al. (2007)), or approximately 9 600 years of propagation. In the case of small angle scattering we expect the protons to move with ballistic properties, meaning 3 000 pc is more than enough for our model. We also notice that the difference between 0.5 and 2 decades are small, meaning that we only make a small

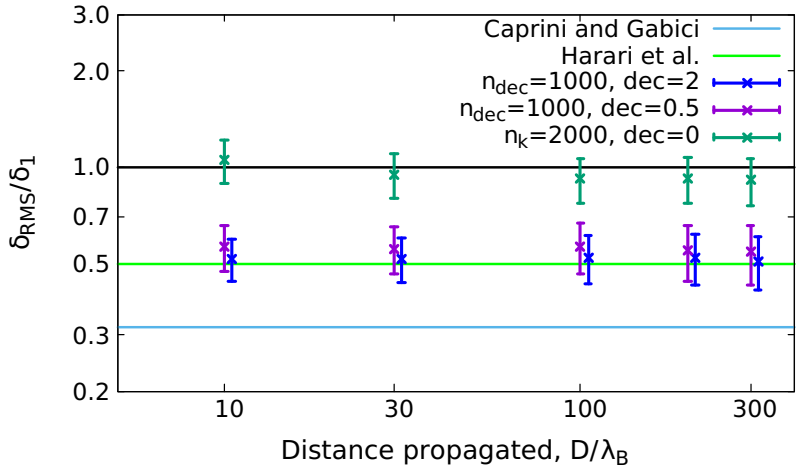

Figure 3.1: Plot of the RMS deflection angle, δ_{RMS}, for turbulent magnetic fields (TMFs) with multiple realizations, each field with its own number of modes per decade (n_{dec}) and total number of decades (dec). For the results marked $n_k = 2000$ the TMFs had no decades, i.e. the wave vectors of the modes, $\boldsymbol{k}_j$, were all of the same length $k = k_{\mathrm{min}} = 2\pi/\lambda_B$. The solid lines represent the theoretical RMS scattering angles as from eq. (2.38), where $\Pi(D/\lambda_B, n_B \gg 2)$ holds different theoretical values: $10^{-1/2}$ (Caprini and Gabici, 2015), 0.5 (Harari et al. (2002), $n_{\mathrm{dec}} \to 0$). δ_1 represent the theoretical δ_{RMS} in the limit where $\Pi(D/\lambda_B, n_B \gg 2) = 1$. Note that the blue values (dec = 2) are shifted slightly to the right for easier viewing

error by only using half a decade for small angle scattering. This also saves a lot of computation time.

From theory (see eq. (2.31)) one expect the energy (or the value of the momentum) of the protons to be conserved, as the force is always applied perpendicular to $\boldsymbol{p}$. To check if there was energy conservation in the simulation, the initial and end momentum was compared for each trajectory. If the deflection angle would be a result of an additional momentum perpendicular to the initial momentum $\boldsymbol{p}$, then the new momentum $\boldsymbol{p'}$ would be

$$\boldsymbol{p'} = \boldsymbol{p} + \delta_{\mathrm{RMS}} |\boldsymbol{p}| \hat{\boldsymbol{e}}_{\perp}, \tag{3.1}$$

where $\hat{\boldsymbol{e}}_{\perp}$ is a unit vector in the direction of the deflection, perpendicular to $\boldsymbol{p}$. Assuming δ_{RMS} is small, one further has

$$p' = |\boldsymbol{p'}| = \sqrt{1 + \delta_{\mathrm{RMS}}^2} |\boldsymbol{p}| \approx \left(1 + \frac{1}{2}\delta_{\mathrm{RMS}}^2\right) p. \tag{3.2}$$

At D/λ_B the values of $\delta_{\mathrm{RMS}} \approx 8.7 \cdot 10^{-4}$ which gives $(p' - p)/p \approx 3.8 \cdot 10^{-7}$. The maximum relative deviation for both simulations in Fig. 3.1 was of order 10^{-10} which is much less than if the momentum was added, i.e. one has energy conservation.

The small angle deflections could also be simulated for more than 2 decades in wave numbers and/or for smaller values of R_g, but this require a substantial amount of time (or many processors) to compute, which in the case of this thesis was prioritized for the SB simulations. The precision of the RK solver could also have been lowered in order to gain shorter simulation time, but then the energy conservation could come into questioning.

3.2 Regular Magnetic Field Models

Table 3.1: An overview of the parameter values of the regular magnetic fields (MFs) and the turbulent magnetic fields (TMFs).

Parameter name	Parameter symbol	Parameter value
Bubble radius	r_{bubble}	50.0 pc
Bubble width	w_{bubble}	2.0 pc
Wall transition width	w_{tr}	0.8 pc
Transition radius, inner to outer MF	$r_{\text{tr,io}}$	51.0 pc
Maximum turbulent scale size, TMF	λ_B	10.0 pc
Lower normalization scale size, TMF	λ_{min}	10.0 AU = $4.85 \cdot 10^{-5}$ pc

From section 3.1 we learned that $n_{\text{dec}} = 1000$ was a sufficient number in order for the TMF to be approximately isotropic. To compare the two regular field models of the bubble, as described by eqs. (2.7)-(2.10), we look at a case where we have a continuous source and trace the protons to a set radius equal to double the bubble radius. The source was set to be located at the origin to get cylindrical symmetry w.r.t. the bubble field. The parameters for the radial magnetic strength $B_{\text{RMS}}(r)$, see eq. (2.11), was defined using the parameters found in Tab. 3.1, as well as the transition radius between the bubble's inner MFs and the external MF in the ISM. The TMF scale sizes is also shown in the table and we assume Kolmogorov turbulence, i.e. spectral power law index $\gamma = 5/3$. In order to compare the fields we looked at four proton energies: $1.8 \cdot 10^{14}$ eV, $1.0 \cdot 10^{15}$ eV, $1.0 \cdot 10^{16}$ eV, and $1.0 \cdot 10^{18}$ eV. The spread in E was to cover cases where R_g in the barrier (see eq. (2.35)) is either much larger, of similar size, smaller, or much smaller than the barrier width. Note that because we use protons and both eq. (2.31) and eq. (2.35) depend on the total electric charge of the particles, any energy represented in our results will apply for any relativistic particle with E/Z equal to the same energies (Z = number of elementary charges = 1 for protons).

Both regular fields (CW and CW-ACW, see Sec. 2.1.1) were then injected with a given number of protons at the origin with isotropically distributed momentum vectors. The proton energies and numbers, and the TMF parameters used for each energy can be seen in Tab. B.1 in the appendix, where the error parameter of the RK solver (ϵ_{RK}) is a parameter indicating the precision in the numerical solution of the EOM (for further details see Press et al., 1997, ch. 16.2). For the random numbers in the computation we used a random number generator with the same initial seed for the same energies, resulting in equal TMFs for the MF models at the same energies, thus the difference in the results would be due to the regular fields only. The protons were sent out from the origin in isotropic directions and were traced until they reached $r = 2r_{\text{bubble}} = 100$ pc or until they had propagated for 100 000 years (i.e. $\approx 31\,300$ pc). Note in Tab. B.1 that $n_{\text{dec}} < 1000$ for the smaller energies due to increasing computation time with decreasing energy. Also, as we expect the less energetic protons to propagate for a longer time, thus contributing more data to the probability density per trajectory, the number of trajectories is less for the smaller energies than the higher energies. In addition, the weighting of B^2 between the regular field and the TMF was assumed to be 50%-50% of B^2_{RMS}, i.e. equipartition.

The probability density (see Sec. 2.3) for each model and energy was calculated from the simulation data, summing up the total time spent by every proton inside 20 equally spaced

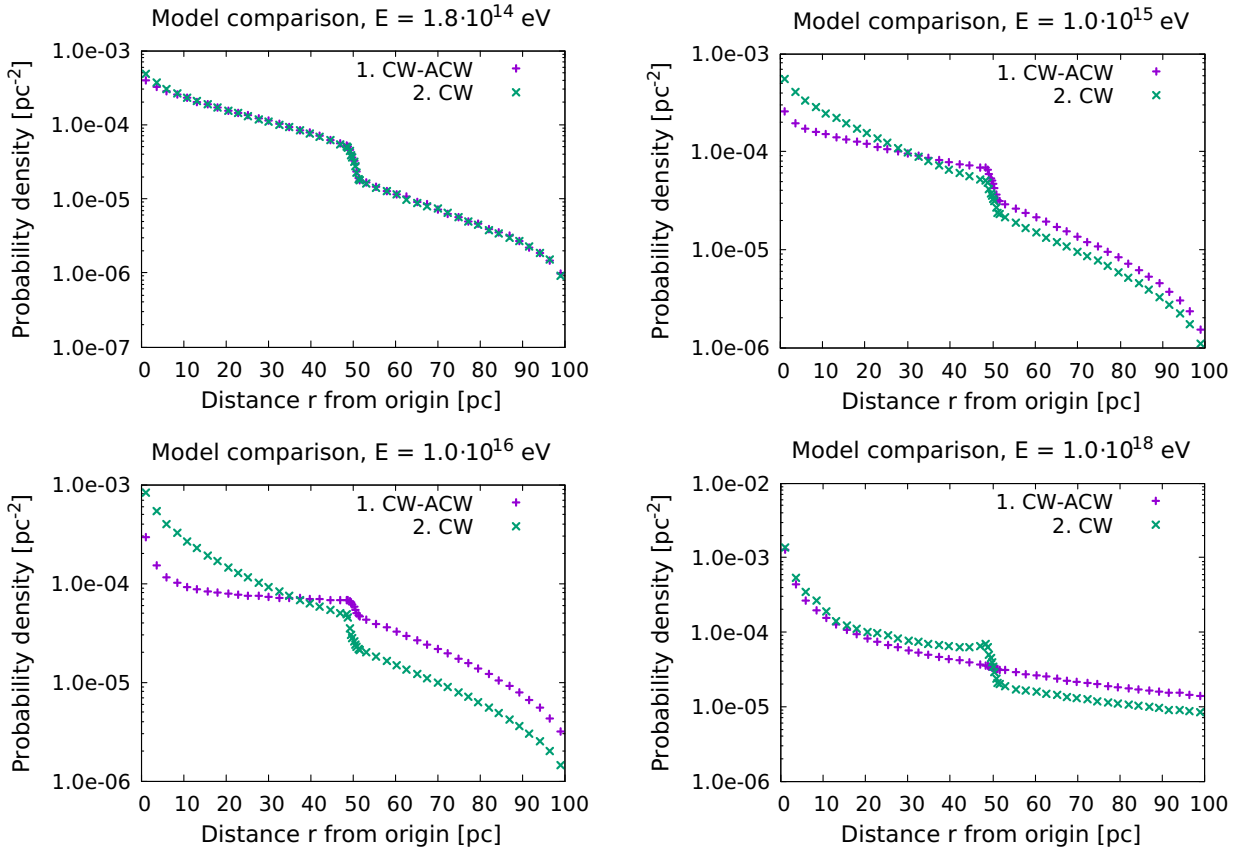

Figure 3.2: The plots show the calculated probability density as function of r from the proton trajectory simulations, each representing one proton energy. The results from the two different models of the inner bubble field is plotted against each other for comparison: 1. Clockwise-anticlockwise rotation (CW-ACW), 2. clockwise rotation (CW) (see Sec. 2.1.1).

r-intervals (i.e. radial distance in the xy-plane) of width $\Delta r = 2.41$ pc inside and outside the bubble barrier. The barrier itself was divided into 10 equal r-intervals, which was ranging from $r = r_{\text{bubble}} - 0.5w_{\text{bubble}} - w_{\text{tr}}$ to $r = r_{\text{bubble}} + 0.5w_{\text{bubble}} + w_{\text{tr}}$. This includes $0.5w_{\text{tr}}$ of the inside and outside regions, i.e. where $B_{\text{RMS}}(r)$ is equal to that of the inside or outside field, see eq. (2.11). The radial value of each bin is set to be the middle radius of each bin, in order for each circular area to be defined by $2\pi r\Delta r$. The results of the simulations of the four energies mentioned earlier can be seen in Fig. 3.2

From the plots in Fig. 3.2 one can see several aspects. At the smallest energies the densities are almost identical, with a slightly higher value for the CW model at the smallest radial distances ($r < 10$ pc). As the energy increases, the CW model tend to increase in probability density at lower r while getting smaller at higher values of r compared to the CW-ACW model. As the energy increases, the effect of the barrier (at $r \sim 50$ pc) on the probability density gets smaller for the CW-ACW model while it stays approximately the same for the CW model. Lastly, outside the bubble ($r > 50$ pc) the shape of the probability density is close to identical for both models. The last observation is the easiest to explain. As there is no difference between the models outside the bubble ($r > 51$ pc), we expect the protons to behave equally w.r.t. the magnetic field. Note

Table 3.2: Propagation time results from the CW vs. CW-ACW model comparison.

Energy E [eV]	Model	Mean total time $\langle t_p \rangle$ [yr]	Mean time outside $\langle t_{\text{out}} \rangle$ [yr]	Mean time inside $\langle t_{\text{in}} \rangle$ [yr]	SE mean inside [yr]	Max time inside $t_{p,\text{max}}$ [yr]
$1.8 \cdot 10^{14}$	CW	17 188.0	2 903.0	14 285.0	200.0	93 957
$1.8 \cdot 10^{14}$	CW-ACW	16 266.0	2 808.0	13 458.0	186.0	90 603
$1.0 \cdot 10^{15}$	CW	15 446.0	3 268.0	12 178.0	131.0	91 799
$1.0 \cdot 10^{15}$	CW-ACW	11 020.0	3 273.0	7 747.0	93.0	69 085
$1.0 \cdot 10^{16}$	CW	8 480.0	1 791.0	6 689.0	67.0	100 000
$1.0 \cdot 10^{16}$	CW-ACW	3 871.0	1 740.0	2 131.0	10.0	18 921
$1.0 \cdot 10^{18}$	CW	905.0	285.0	620.0	39.0	100 000
$1.0 \cdot 10^{18}$	CW-ACW	540.6	264.4	276.2	3.4	9 482

that the TMFs have the same modes for each energy, and while the inner field may cause the protons to leave the bubble at different spatial positions where the TMFs would have different phases, these details are washed out in the statistics. It is also important to note that while the inner fields are generally independent of angular direction ϕ in the xy-plane (i.e. cylindrical symmetry), with exception of the CW-ACW model at $y = 0$, the outer field has no such symmetry. This means that one would expect different probabilities outside the bubble depending on ϕ. Normally one would define two probability densities, one parallel and one perpendicular to the magnetic field lines of the outer field. However, this will not be considered in this thesis, as we are more interested in the properties of the bubble and not the ISM.

Now, if one assumes the models of the inner fields have no preferred point at which they let protons escape the field, then statistically the protons will leave both fields isotropically w.r.t. ϕ (and θ). Consequentially the proton motion outside the bubble should be statistically equivalent, with the same amount of time spent inside each r-interval. The only explanation of the difference outside the bubble is that the total time that the protons have used is different for the relevant energies. This is in agreement with the raw data from the simulation, as seen in Tab. 3.2, where one sees that the mean propagation time $\langle t_p \rangle$ is larger for the CW model than the CW-ACW model. Additionally, one can see that the mean time spent propagating outside the bubble (in and outside the barrier) is approximately the same, as expected.

Looking at the maximum time of any trajectory in the two models at the different energies (see Tab. 3.2) one sees that while at larger E the maximum time goes down for the CW-ACW model, the maximum time in the CW model goes to the limit of 100 000 years set by the simulations. This means that not all protons escaped to a distance $r = 2r_{\text{bubble}}$, and are presumably being trapped in the bubble. One possible explanation of this can be the structure of the regular fields themselves. By extrapolating the fields seen in Figs. 2.3 and 2.4 in the z-direction and taking a cut of the xy-plane along the z-direction (i.e. through $x = 0$) one ends up with two pictures of the regular field inside the bubble. One where the MFLs point into the plane for all values of y, i.e. the CW-ACW model looking in positive x into the plane, and one where the MFLs point into the plane at $y > 0$ and out where $y < 0$, i.e. the CW model looking in positive x-direction into the plane. If one excludes the TMF, any charged particle initially propagating from the origin in this plane would only be accelerated in a direction limited by this plane, in other words the par-

ticle would stay in the plane as long as it stays inside the bubble. Assume a proton (or another positively charged particle) with $R_g > 2r_{\text{bubble}}$ that is sent fourth from the origin with an angle $\theta \to \pi$ w.r.t. the positive z-axis (i.e. close to negative z-direction). Depending on the model, one of two things would happen: If the model is the CW-ACW, the proton is initially deflected towards negative y-direction and keeps going until it hits the barrier (due to a large R_g). If it is the CW model, the proton would initially be deflected towards the z-axis and when it reaches $y = 0$ the acceleration flips again towards the z-axis thus making the proton "resonate" around $y = 0$. This may also be the case with a TMF though the filed deflects the proton into an angular direction, because for high E values this deflection gets smaller per propagated distance.

When looking at the raw data for $E = 1.0 \cdot 10^{18}$ eV, we see that the minimum z-value for the CW model was -29 647 pc while it was only -1 432 pc for the CW-ACW model. This indicate a resonance in the CW model for particles propagating in negative z-direction. One may, using the same case as above, convince one self that for the CW model all positive particles propagating in positive z-direction are deflected away from the z-axis, while towards positive y-direction for the CW-ACW model (both giving no resonance). Further we note that any resonance will keep the protons inside the bubble longer thus result in higher probability density inside the bubble (and presumably for lower values of r) and longer mean propagation time. Both of these effects are present in the plots and the average time data for the higher energies in Fig. 3.2 and Tab. 3.2. The resonance should not have a large impact on the smaller energies, i.e. $R_g \ll \lambda_B$, as the TMFs will contribute substantially to the deflection of the protons. For $E = 1.8 \cdot 10^{14}$ eV the $R_g \approx 1.8$ pc inside the bubble and the protons would rather turn to helical motion along the MFLs with slight deflections due to smaller turbulence scales. Additionally, viewed against the Local Bubble, who's size perpendicular to the Galactic plane is estimated to approximately 600 pc (see Sec. 1.1), particles resonating for several kpc perpendicular to the Galactic plane would soon find themselves outside the LB and the width of the halo component of the Galactic MF (around 3 kpc, De Marco et al. (2007)).

Now we take a look at the probability density at the barrier. What is clear from the plots in Fig. 3.2 is that for the CW-ACW model the effect of the bubble barrier is decreasing with increasing E until the protons do not seem to "see" the barrier for $1.0 \cdot 10^{18}$ eV. For any proton with R_g in the barrier much greater than the width of the barrier itself is likely to be only experiencing a small deflection when propagating through the barrier. Only if the proton hits the barrier at an angle so that it is almost parallel to the barrier, and if the orientation of the MFLs is so that the MF deflect the proton towards the side of the barrier at which the proton entered, then the proton is likely to be reflected from the wall. For high energies in the CW-ACW model this would only happen for protons moving in the negative z direction at $y > 0$ or in positive z-direction at $y < 0$ (see Fig 2.3 for spatial orientation of the CW-ACW field). When they later reach the other side of the bubble, still propagating in the same z-direction, they will be deflected outwards and away from the bubble and escape. While at smaller energies, where $R_g < w_{\text{bubble}}$, there is always a large possibility that the proton is reflected from the wall as the proton may perform a full (helical) loop in the barrier and be thrown out again. In the case for $E = 1.0 \cdot 10^{16}$ eV the gyroradius is $R_g \approx 1$ pc inside the barrier. This means that the particle might be reflected by the barrier which has a width of 2 pc. Additionally, the R_g inside the bubble is approximately 100 pc, equal to the diameter of the bubble, which puts the protons somewhere between diffusive and ballistic (more towards the latter). As the TMF has a largest scale size of 10 pc, it could easily deflect the protons in an angular direction in the barrier and scatter the protons around

the bubble. Given enough reflections this could make the protons inside become approximately equally distributed thus contributing to equally to the r-intervals of the accumulated time per area and flattening out the probability density. This might be the case for the flattening of the CW-ACW model in the plot as this model do not get the possible "resonances" that the CW model may get.

In contrast to the CW-ACW model, the fall of the probability density over the barrier does not seem to change for the CW model. Why this is, is not easily explained. It might be a result of the earlier mentioned "resonance" where the protons also reach the wall for ballistic energies for each crossing of the z-axis, but we can not be entirely sure.

In the end we are mostly interested at the low energy particles as these are the ones most likely to come from supernova remnants either from within the Local Bubble or from other adjoined bubbles. The two models show little difference at the lower energies and subsequently we may therefore only use one model in the further computations. Thus we choose to use the CW-ACW model going forward.

3.3 Continuous Source

In this section we will be looking at the case where we have a continuous source of CRs inside the magnetic SB. The source was set to be located at the origin, as in Sec. 3.2, in order to obtain cylindrical symmetry w.r.t. the regular bubble field. As mentioned at the end of Sec. 3.2 we only consider the CW-ACW model for the bubble field. With the case of a constant source of CRs, one does not possess the total number of particles in the system (as one could approximate from a bursting source like a SN), but one would be able to tell something about the production rate of the CRs. If one knows the production rate as a function of energy and the average time a particle would use to leave the system (i.e. the bubble in our case) one would be able to acquire a steady state particle number thus with the probability density also get the particle density.

By increasing the number of injected energies for the protons, new simulations were performed for a continuous source in the same manner as in Sec. 3.2. The model parameters was kept the same as well, see Tab. 3.1, and the maximum radius was $R_{\max} = 2r_{\text{bubble}}$ beyond which the particles were considered lost. The input parameters of the TMF for each proton energy can be seen in Tab. B.2 in the appendix, while data on the change in particle momentum (due to small numerical errors by the RK solver when solving the EOM) can be seen in Tab. B.3. Note that at small E the relative error of the momentum increases, but in order to keep the simulation time within reason some precision had to be sacrificed. We still note that the largest relative change was $\approx 7\%$ ($E = 1.8{\cdot}10^{13}$ eV, with a mean relative change $\sim 0.3\%$) in a region where we have large angle scattering (diffusion). As will be later shown, we only have small angle scattering for the largest energies where the relative change in momentum was small compared to δ^2_{RMS}.

To analyze the resulting time density distributions we use the three cases of eq. (2.61) defined in Sec. 2.3.1, i.e. cases 1, 2 and 3. Case 1 was shown to be a good substitution for eq. (2.56) (Gaussian diffusion to a time t_f), and using the fact that the denominator in eq. (2.60) (Gaussian diffusion to a time t_f, only considering particles inside a radius $R_{\max}$) is a constant for any given $R_{\max}$ case 1 should be a good substitute for eq. (2.60) as well. Further, the ballistic time density was described by eq. (2.52) which corresponds to case 3 (or case 1) with $d = -1$ (and $\sigma \to \infty$).

To see how these functions best fit to the different results, we first take the probability density

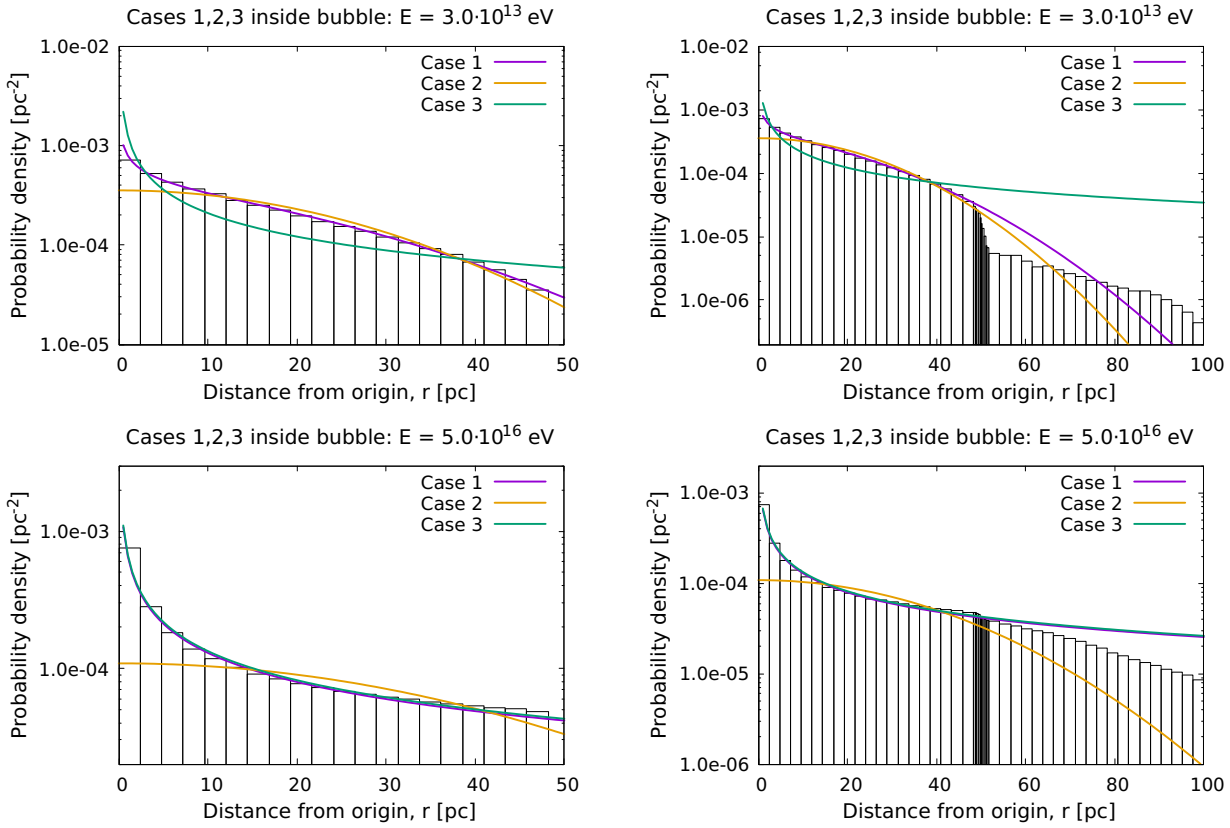

Figure 3.3: Best fit of cases 1, 2, and 3 to the time density distribution inside the bubble at proton energies $E = 3.0 \cdot 10^{13}$ eV (top) and $E = 5.0 \cdot 10^{16}$ eV (bottom). The left plots only show the inside of the bubble, while the plots to the right show the entire system out to $r = 2r_{\text{bubble}}$. The black regions in the plots on the right correspond to the bubble barrier.

results from two energies, $3.0 \cdot 10^{13}$ eV and $5.0 \cdot 10^{16}$ eV, and perform curve fitting on them. In the lower energy case the protons' gyroradii inside the bubble are less than 1 pc and we expect therefore diffusion like motion of the protons. At the higher energy case a protons gyroradius is ~ 500 pc and thus we expect more ballistic motion than diffusion. The best fit to the results of all three cases are shown in Figs. 3.3 and 3.4 where each data point (given an r-value corresponding to the middle of the bin, see the figures) is given an uncertainty of one tenth its value. In Fig. 3.3 we see the functions fitted to the values inside the bubble while in Fig. 3.4 we see them fitted to the outside values.

In Fig. 3.3 we see that the case 1 fit is close to perfect for both energies (note that in the bottom plots case 1 and 3 almost completely overlap). Further, while case 3 (representing a Gaussian-like distribution) never really fit any of the energies it is far better for the lower energy. On the contrary, case 2 gives a good fit at the higher energy while being bad at lower. The fact that case 2 gives such a good fit indicate ballistic-like motion at higher energies. In general, the plots show that the case 1 fit is performing well for both high and low particle energies.

Looking at the plots in Fig. 3.4 for the curve fitting outside the bubble one can see a few changes to the fitting cases. While case 1 still perform well it is now approximately equal to case 2 for both energies. Case 3 on the other hand is not performing well in any of the fits. The

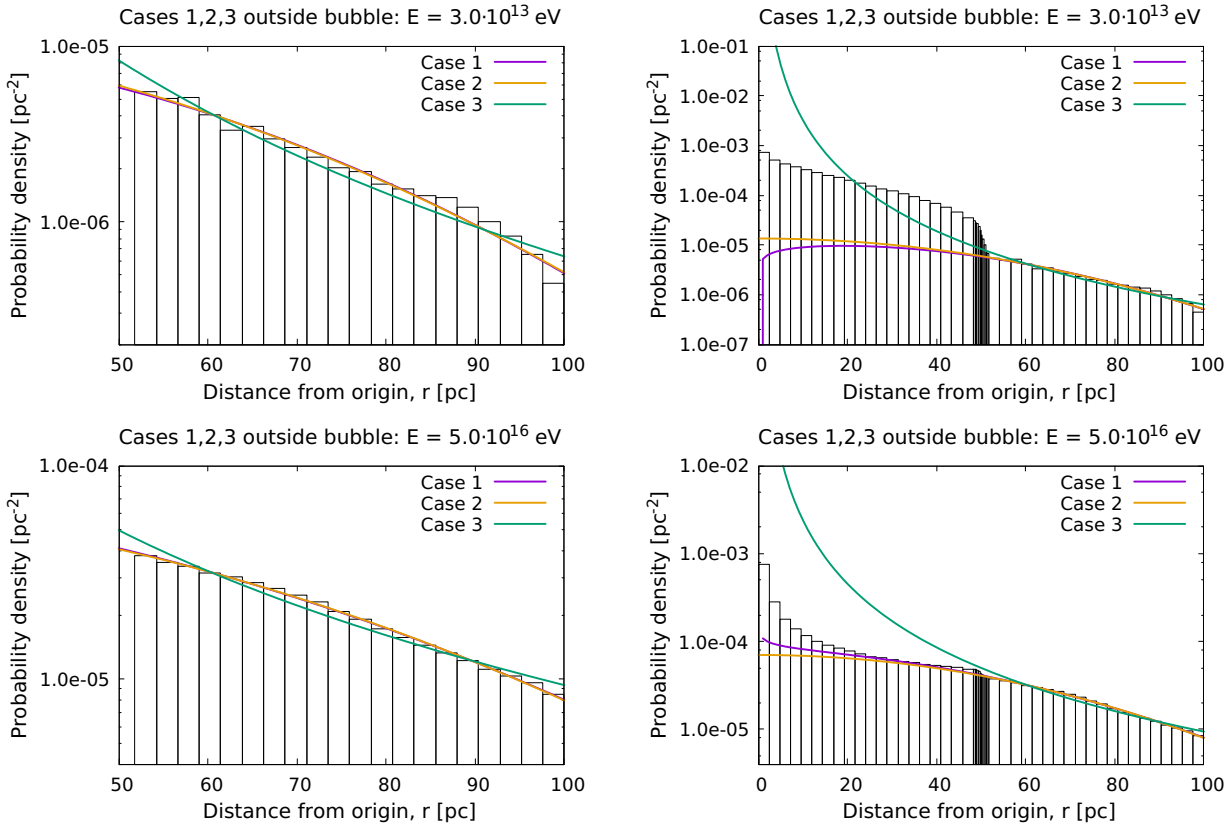

Figure 3.4: Best fit of cases 1, 2, and 3 to the time density distribution outside the bubble at proton energies $E = 3.0 \cdot 10^{13}$ eV (top) and $E = 5.0 \cdot 10^{16}$ eV (bottom). The left plots only show the outside of the bubble, while the plots to the right show the entire system out to $r = 2r_{\text{bubble}}$. The black regions in the plots on the right correspond to the bubble barrier.

explanation to this lies in the fact that outside the bubble the $B_{\text{RMS}} = 5$ μG giving a gyroradius $R_g \sim 10$ pc for $E = 5.0 \cdot 10^{16}$ eV. This is the same as λ_B of the TMF and is smaller than the bubble radius thus no longer resulting in ballistic-like motion. In general this means that both cases 1 and 2 work well for curve fitting of the data outside the bubble for most of the relevant energies (see Tab. B.2), but we would still expect case 3 to be valid (and thereby case 2 not to be) at energies $E \gg 5.0 \cdot 10^{16}$ eV, i.e. ballistic particles outside the bubble. Similarly to what is seen inside the bubble, in the case of ballistic particle outside the bubble we would expect to see an effect in the case 1 parameters for the highest energies, i.e. that $\sigma \to \infty$, making case 1 equal to case 3.

3.3.1 Curve Fitting the Probability Densities

The curve fitting was performed for each of the cases 1, 2, and 3 (see Sec. 2.3.1) on the probability densities for each E (see Tab. B.2). An error estimate of one tenth of the data values was used (as was done in Figs. 3.3 and 3.4). The resulting values of the fitting parameters, with the exception of the amplitude parameter A, can be seen in Fig. 3.5 for case 1 and Fig. 3.6 for cases 2 and 3. As argued earlier case 3 is not a good fit outside the bubble and would not give any

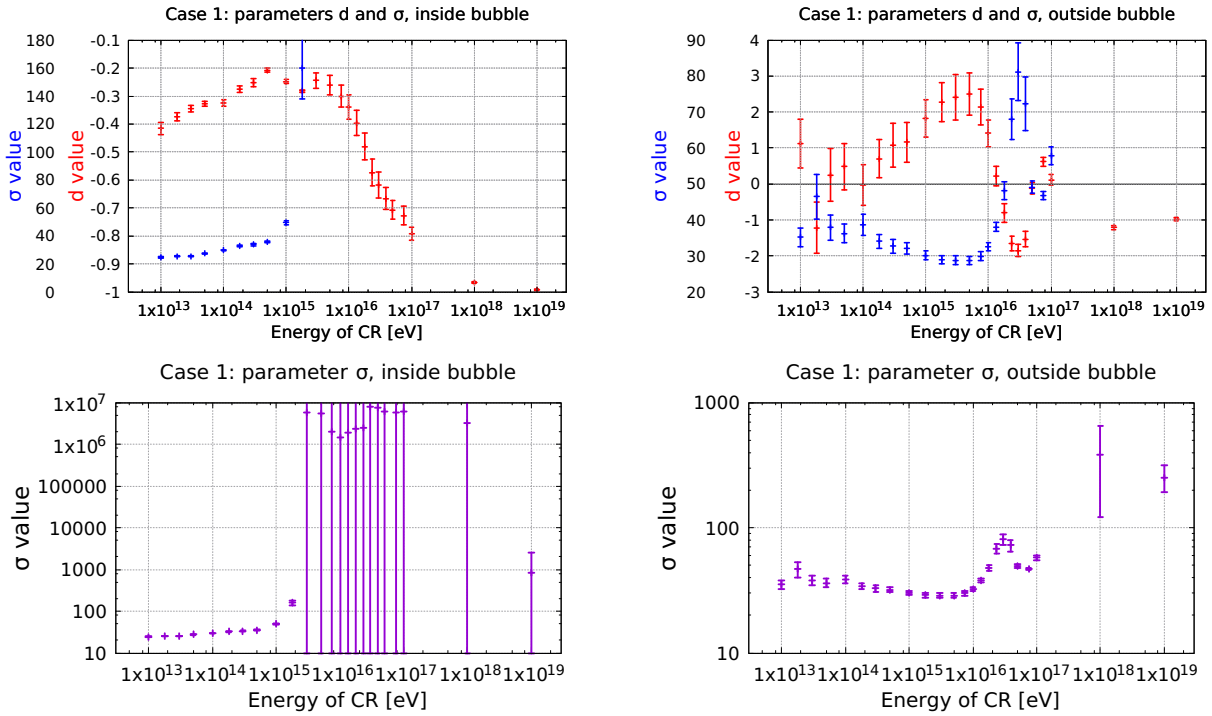

Figure 3.5: Results from the curve fitting of the probability densities from the simulations with a constant cosmic ray source. The plots show the fitting parameters d and σ from the case 1 curve fitting, see Sec. 2.3.1.

valuable contribution to information about the probability densities and is therefore excluded from the figure. The amplitude constants are not likely to be normalized with respect to the the other parameters and the function fitted, due to the change in the probability densities over the bubble barrier, thus are only used to gain the best possible fit and therefore we do not plot them. All the parameter values (with estimated errors) from the case 1 curve fitting (the best fit in general) are shown in Tabs. B.4 and B.5 in the appendix.

From the top-left and bottom plots in Fig. 3.5 we notice that the σ-parameter "diverges" after $E = 1.8 \cdot 10^{15}$ eV inside the bubble. At this energy the gyroradius R_g of the protons are approximately 18 pc $\approx 2\lambda_B$ of the TMF, and at the first energy where σ has "diverged" we find that the gyroradius is approximately 30 pc ($E = 3.0 \cdot 10^{15}$ eV). Consequently, case 1 should equal case 3 (Fig. 3.6) for $E \geq 3 \cdot 10^{15}$ eV which is what we see. Additionally, we see that though the values of d are the same for case 1 and 3 for the higher energies (inside the bubble), the error estimate in case 1 is larger which is due to the fact that d and σ are coupled. Looking at the plots outside the bubble barrier in Fig. 3.5 we do not see the same sudden divergence in the values of σ, though the value of σ increases at the two largest energies. This would be expected if the density goes towards that of a ballistic case, i.e. probability density $\propto r^{-1}$, which is what we see for the two highest energies where $d \to -1$ both inside and outside the bubble.

Considering the inside case of Fig. 3.5, we see that as σ "diverges" the value of d does not sharply change to -1 (indicating ballistic motion), but changes rather smoothly from $d \approx -0.25$ to $d = -1$. From the fit function (eq. (2.61)) we see that a value $0 < d < -1$ with $\sigma \to \infty$ (i.e. exponential = 1) describes a probability density that is less decreasing than the ballistic case. To

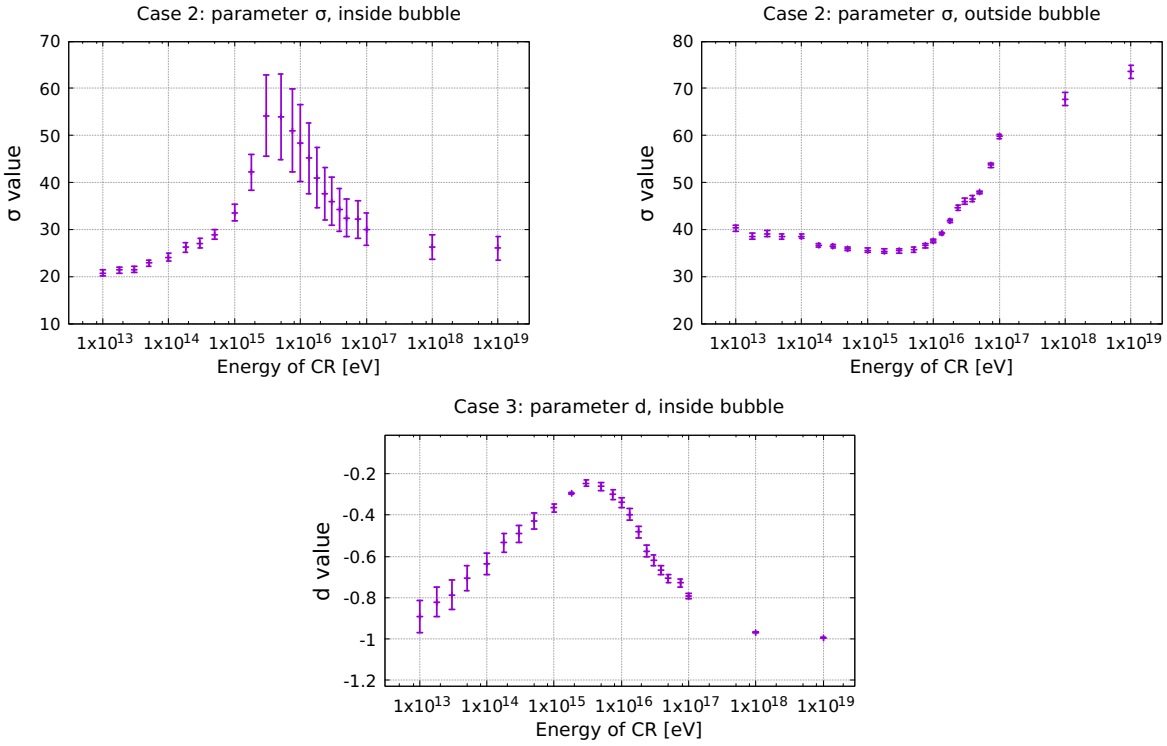

Figure 3.6: Results from the curve fitting of the probability densities from the simulations with a constant cosmic ray source. The top plots show the fitting parameter σ from the case 2 curve fitting, and bottom plot shows the fitting parameter d from the case 3 curve fitting inside the bubble, see Sec. 2.3.1.

get a better understanding of the probability density at these values, a plot of the probability density at $E = 7.5 \cdot 10^{15}$ eV is shown in Fig. 3.7. We see straight from the plot that the probability density has flattened out at higher r inside the bubble. As argued in Sec. 3.2, when the gyroradius in the barrier wall is slightly smaller than the barrier width, the particles are most likely to be reflected by the bubble barrier while still having a gyroradius inside the bubble of similar order to r_{bubble} thus letting the particles move quite freely and distribute themselves relatively fast inside the bubble. Consequently the position probability density inside the bubble will become approximately constant in a short period of time (w.r.t. total propagation time) and result in a flat(ter) probability density. In other words, as an integral of a constant particle density over time equals the constant multiplied with the total time, thus resulting in a constant probability density. To get a better view of how the particle trajectories look like, the trajectories of four energies ($1.0 \cdot 10^{14}$ eV, $1.0 \cdot 10^{15}$ eV, $1.0 \cdot 10^{16}$ eV, and $1.0 \cdot 10^{17}$ eV) are plotted in Figs. C.2 and C.1 in the appendix. These plots will not be discussed further here.

Looking at the plots in Fig. 3.5 we see that outside the bubble there is a sudden transition at $E \sim 10^{16}$ eV where d goes from positive to negative values while σ gets a sudden increase in value. Additionally, at $E = 10^{17}$ eV it looks like there is almost another transition pushing the values in the opposite direction than that of the first one. As a decreasing d (more negative) would result in a faster decreasing probability density while an increase of σ result in the opposite, the net result of the first change in the values is hard to predict. We see that $E = 10^{16}$ eV is in be-

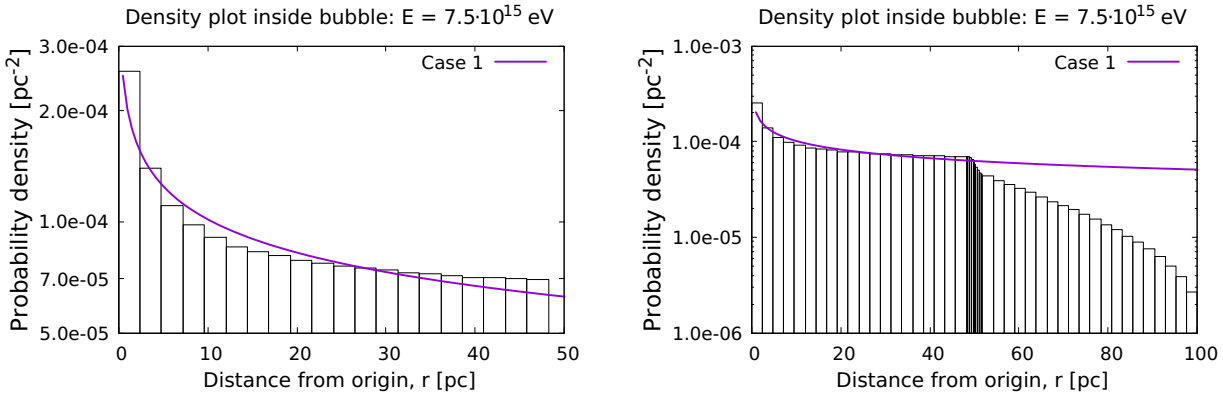

Figure 3.7: Best fit of case 1 to the time density distribution inside the bubble at proton energy $E = 7.5 \cdot 10^{15}$ eV. The left plots only show the inside of the bubble, while the plots to the right show the entire system out to $r = 2r_{\text{bubble}}$. The black regions in the plots on the right correspond to the bubble barrier.

tween the the higher energy in Fig. 3.4 and the energy in Fig. 3.7. Looking at the part of the plots outside the bubble we see a slight tendency for the shape of the probability density to straighten out (and possibly start to curve upwards) at higher values of r when E increases. Additionally, we recognize that at $E = 5.0 \cdot 10^{16}$ the gyroradius outside the bubble $R_g \approx \lambda_B = 10$ pc. This could mean that the transition is a result of the particles becoming more ballistic in the external MF similarly to what was observed inside the bubble.

In an attempt to explain the mentioned transitions it is important to look at the magnetic fields themselves. Inside the bubble we have a regular field fulfilling cylindrical symmetry while the outside MF does not (as it points in constant x-direction, see Fig. 2.3). Therefore we do an error in our approximation where we simplify the particle density distribution to be independent of angle outside the bubble barrier as one would have two different diffusion constants for diffusive motion in respectively parallel and perpendicular direction to the MFLs. If $R_g \gg r_{\text{bubble}}$ (the distance between the barrier and R_{max}) we do not expect the particles (protons) to be deflected in any major direction and thus we should not see a difference in the densities w.r.t. ϕ within R_{max} (i.e. we expect full ballistic motion). Further, in the case of $R_g \ll \lambda$ we expect the particles to follow the MFLs. As the regular field is modelled with 50% of the total field energy, the particles are more likely to move along the direction of the regular field with some motion perpendicular due to the TMF. Note that outside the bubble the movement in z- and y-direction is symmetric due to the constant regular field in x-direction. The interesting case is when $R_g \approx \lambda$ as one would would see strong deflections as helical motion around the regular MF with additional smaller deflections induced by the TMF. Whether or not this may explain the second transition is not certain. In order to check the effect of both λ_B and the partial energy in respectively the regular or turbulent MFs, new computations would have to be performed while changing one parameter at the time. These are computations we regrettably did not have the time to perform.

As shown in Sec. 2.3.1, the fitting cases 2 and 3 are only equivalent to case 1 with either $d = 0$ or $\sigma \to \infty$, but they may be able to help explain what we see in the results of case 1 (Fig. 3.5). As we have argued, case 2 is working well for mostly all energies outside the bubble and

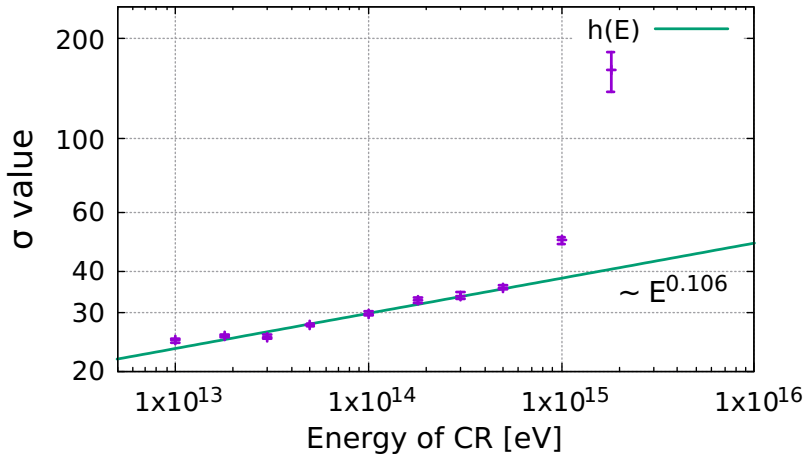

Figure 3.8: Plot of the σ values of curve fitting case 1 inside the bubble at lower energies. $h(E) = A \cdot E^{\alpha}$ is fitted to the σ-values of the 8 lowest energies.

for the lower energies inside. Looking at the results from case 2 in the bottom plot in Fig. 3.6 (outside the bubble) we see equal tendencies of the σ values in case 2 as in case 1, and while the transition is still there for case 2, we do not see a local maximum in the values of σ. The local top in the values of σ in case 1 may be there because of a strong correlation between d and σ.

On the inside of the bubble, Fig. 3.3 shows that case 2 is only valuable if E is small. Consequently the values for σ at higher E inside the bubble in Fig. 3.6 make no sense. On the other hand, if one compares σ of lower energies in cases 1 and 2 (Figs. 3.5 and 3.6) inside the bubble, we see that the σ values are almost equal with case 2 being slightly smaller, probably due to the difference in values of d. As $d < 0$ gives a steeper fall for eq. (2.61) than $d = 0$, σ would have to increase in order to (partially) negate the change. Further we see that the values of σ for lower energies in both cases 1 and 2 approximate a linear dependence in logarithmic scale, i.e. $\sigma \propto E^{\alpha}$. Fitting the 8 lowest values of σ in case 1 to a function $h(E) = A \cdot E^{\alpha}$ resulted in $\alpha = 0.106 \pm 0.009$ and the fit can be seen in Fig. 3.8.

If we were to look at what the physical meaning of σ in eq. (2.61) is, we remember that in eq. (2.48) we have $\sigma^2 = 2Dt$ where D is the diffusion coefficient. For 2D Gaussian diffusion one has for the radial distance $\langle r^2 \rangle = 4Dt$, meaning σ becomes a measure of the RMS distance. This is easily shown by integrating r^2 multiplied with eq. (2.49) over all space (dA). For cosmic rays propagating with diffusive motion in a purely isotropic TMF defined by Kolmogorov turbulence ($\gamma = 5/3$, eq. (2.17)), with no regular field components and with gyroradii of the particles $R_g \ll \lambda_c$ (= correlation length $< \lambda_B$) one has (Berezinskii et al., 1990):

$$D \propto E^{1/3}. \tag{3.3}$$

If we were to use eq. (2.48) and the result in Fig. 3.8, assuming $t = t_f$ is constant as most particles reach $R_{\max}$, we get $D \propto E^{0.212}$. We see that it is off by a factor of $\sim 3/2$. As both the gyroradii of the particles are not necessarily much smaller than λ_B ($> \lambda_c$) and the fact that we have a regular field, we do not expect to recreate eq. (3.3). Another reason to why we do not get the result from eq. (3.3) may be because of the assumption made when equating the expected probability density for diffusive motion with the fitting function (i.e. eq. (2.60) and

eq. (2.61)) in Sec. 2.3.1. In Fig. 2.8 we see that for $4Dt = 10$ we should have $\sigma^2_{\text{fit}} = \sigma^2 = 5$, but the fit gave $\sigma_{\text{fit}} = 2.142 \Rightarrow \sigma^2_{\text{fit}} = 4.588 = 0.918\sigma^2$. Further, for $4Dt = 100$ ($\sigma^2 = 50$) we got $\sigma_{\text{fit}} = 6.591 \Rightarrow \sigma^2_{\text{fit}} = 43.441 = 0.869\sigma^2$, thus the σ_{fit} calculated in the curve fitting is lower than the true value used in eq. 2.60 and seemingly increasing in relative error with increasing Dt. On the other hand, due to an increasing MF strength in the barrier (where the diffusion coefficient would change) we get reflection of the CRs that is not expected by diffusive motion in the MF inside the barrier. This may in turn effect the probability density so that one get an increase in σ (as seen when σ "diverges") though this primarily happen once the particles leave diffusive motion. A final notation is that in addition to the requirement of diffusive motion, the $\sigma^2 \propto D$ assumption should also be viewed over scales $\gg \lambda_c$ or over many realizations of the TMF to wash out details of the TMF. We try to do the latter, but we still have a model that is of similar scale as λ_B.

If we look at the values of σ at low energies for the fitting cases outside the bubble (case 1 and 3, Figs. 3.5 and 3.6), we see that contrary to inside the bubble, the values of σ has a local minimum at $E = 5 \cdot 10^{15}$ eV and increase slightly with decreasing E. As mentioned when we were looking at the transition region at $E \sim 10^{16}$ eV, the outside field does not have cylinder symmetry. If one assumes the particles mainly follow the regular MFLs (i.e. motion in the x-direction), the particles leaving the bubble at $x = 0$ will have further to go in order to reach the maximum radius set by the model than particles leaving at $y = 0$. Simple calculation gives a 73% longer path for $x = 0$ than $y = 0$ for $R_{\text{max}} = 2r_{\text{bubble}}$, i.e 50 pc for the first and 86.6 pc for the latter. This angular dependent motion becomes difficult to explain using an angular independent model. Thus it is clear that a cylinder symmetric function like eq. (2.61) will not be sufficient to truly depict the position and time density distributions outside the bubble, especially when the particles leave at different angles.

3.3.2 Escape Time and Particle Density

As mentioned in the beginning of Sec. 3.3 the mean escape time, or mean time spent, of the CRs in the bubble are of high interest. Together with the accumulated time density one may calculate the particle density when the system is in steady state. To calculate the escape time for the protons we calculated the mean time each particle spent inside the bubble. Note that we defined inside by the inner 20 r-intervals (48.2 pc) used when fitting the probability density, i.e. inside of the bubble barrier (see Sec. 3.2). The resulting escape times from the simulations are shown in Fig. 3.9. More data of the propagation time of the trajectory simulations can be seen in Tab. B.6 in the appendix. From the table we see that for the smallest energies some protons reached the absolute value in propagation time set by the simulation. This would possibly make the calculated escape time smaller as the particles may still be inside the bubble. The faction of protons that propagated for the full 100 000 yr was not more than 3% for any energy, indicating that the calculated values are very close to the more precise escape time values if the particles were allowed to propagate until they reached the outer boundary of $r = 100$ pc. To do this we would have to increase the propagation time and thereby the total computation time. Berezinskii et al. (1990) states that for CR with diffusive motion the diffusion coefficient has the property $D \propto E^{1/3}$, thus making the mean escape time ($\langle t_{\text{esc}} \rangle = \langle t_{\text{in}} \rangle$) to a given radius $\langle t_{\text{esc}} \rangle \propto E^{-1/3}$. To check the energy dependence of the mean escape times, the results for $E \leq 1.8 \cdot 10^{15}$ eV was fitted

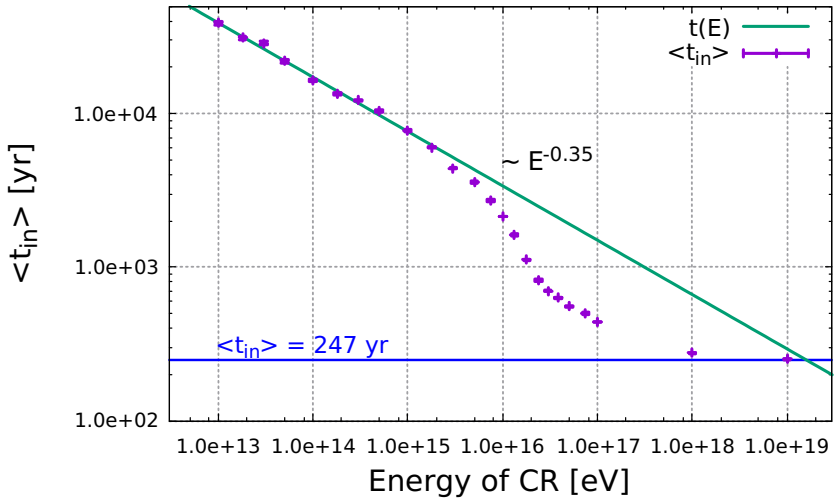

Figure 3.9: Mean time spent inside the bubble ($\langle t_{\text{in}} \rangle$) for each particle energy in the simulations. The green curve represent the function $t(E) = A \cdot E^{-\alpha}$, and is fitted to the escape times for energies $E \leq 1.8 \cdot 10^{15}$ eV. The blue line represent the theoretical mean time spent by isotropically emitted, purely ballistic particles.

against a function

$$t(E) = A \cdot E^{-\alpha}, \tag{3.4}$$

with A and α being fitting parameters. The result of the fit was a value

$$\alpha = 0.354 \pm 0.008,$$

which is just shy off the theoretical 1/3 value, and further giving an indication of the mean escape time for lower energies. As mentioned in Sec. 2.2.1 we only go down to proton energies of $E = 1.0 \cdot 10^{13}$ eV because lower energies would require very long computation time in order to keep up the precision of the simulations. However (see Fig. 3.9), we are already in the scaling region w.r.t. E and we may therefore just extrapolate down to lower E.

We see from Fig. 3.9 that the escape time from the bubble (i.e. the mean time inside) starts to drop away from that expected from diffusion (i.e. $t(E) \propto E^{-1/3}$) at energies $\geq 3.0 \cdot 10^{15}$ eV. The largest bend we see at $E = (5-8) \cdot 10^{15}$ eV, and the escape time thus gain a knee-like structure around this energy. At $3.0 \cdot 10^{15}$ eV the gyroradius inside the bubble is ≈ 30 pc $= 3\lambda_B$, while inside the barrier it is ≈ 0.25 pc $= w_{\text{bubble}}/8$. We also recognize $E = 3.0 \cdot 10^{15}$ eV as the energy at which σ "diverged" in the fitting of the probability densities (Fig. 3.5). We can therefore define an energy limit for when the escape time of the protons deviate from the trend of diffusive motion inside the bubble, and we set the limit to be $E_{\text{diff}} = 2 \cdot 10^{15}$ eV. Further, we see that the mean time has a second "transition" where the absolute value of the derivative of $\langle t_{\text{in}} \rangle$ w.r.t. E stops growing and start to decrease in value, thus $\langle t_{\text{in}} \rangle$ starts to approach a constant value. This starts at the data point for $E = 2.4 \cdot 10^{16}$ eV where the gyroradius in the barrier is $R_g = 2.1$ pc $\approx w_{\text{bubble}}$. At this energy limit particles are more likely to get through the barrier than being reflected by it, thus the bubble looses most of its effect on the probability density and the fall in probability over the wall is approaching zero (e.g. see Fig. 3.4). These "transitions" look very much like the "knee"

and "ankle" features of the CR spectra (see Fig. 1.2), where the first feature (the "knee") being located at approximately the same energy while the "ankle" in Fig. 3.9 is more than an order of magnitude lower. This may indicate that the LB has some effect on the "knee" in the observed CR spectra.

The blue line in Fig. 3.9 is a mean escape time for purely ballistic particles, calculated from eq. (2.55) using $r_{\text{limit}} = 48.2$ pc giving $\langle t_{\text{limit}} \rangle = 246.9$ yr. We see from the figure that the mean time inside the bubble for the two highest energies are close to this value, just as expected when the particles' gyroradii are $R_g \geq 10\,000$ pc inside the bubble, but still ≥ 100 pc in and outside the barrier. This further add on to the ballistic properties to these particles energies when considering our MF model.

If we were to have a constant CR source where the injection rate of particles (into the system) was well defined w.r.t. the particle energy, we would be able to calculate the particle density at a position inside the bubble using the results from the probability densities from the simulations and the escape times shown in Fig. 3.9. The resulting particle densities would then correspond to what we would expect to see in the observed CR spectra at a radial position inside the bubble. We stress the position to be inside the bubble as we here have cylindrical symmetry in the bubble model in contrast to outside the bubble barrier in the ISM. Note that one would have to either re-normalize the probability densities inside the bubble in order to use $\langle t_{\text{in}} \rangle$ (see Tab. B.6 or Fig. 3.9), or still use the probability densities and use the mean propagation times from the simulations ($\langle t_{\text{prop}} \rangle$ in Tab. B.6).

The full effect of what we see from Fig. 3.9 is that if the injection rate of CRs into the bubble from a constant source at the center of the the modelled superbubble is well defined and follows a power law in energy ($N(E) \propto E^{-\beta}$), we would expect to see properties in the CR spectra similar to the "knee" and "ankle" in our observed CR spectra (see Fig. 1.2). As we have only looked at a single constant source inside the bubble and have not considered multiple sources (injection at random position inside the bubble giving a more constant particle density) or any sources outside the bubble, the degree of the Local Bubble's effect on the observed CR spectra are however unclear. Additionally, we have only used a very simplified 2D model with one set of parameters for the bubble, thus new simulation using other bubble parameters, or even a more realistic 3D model of the bubble's MF, must be performed in order to truly validate the effect of the LB on the CR spectra. With the above considered, the results are a positive indication that there might be something to the LB considering the CR spectra.

In Giacinti et al. (2015) the authors showed that the CR "knee" could be entirely explained by energy-dependent CR leakage from the Milky Way. They did so by simulating individual CRs trajectories in the Galactic mean field (i.e. the MF in the ISM) and found that the escape time of the cosmic rays exhibited a knee-like structure around $E/Z = \text{few} \cdot 10^{15}$ eV (Z = number of elementary charges). They modelled the TMF using Kolmogorov turbulence and two different scales for the largest turbulent fluctuations (i.e. λ_B), namely 10 pc and 25 pc. Their result in the escape time of the CRs (Fig. 1 Giacinti et al., 2015) is closely resembling our result from Fig. 3.9 indicating that the LB may, in addition to diffusion of CRs in the ISM, have some effect on explaining the CR "knee". We have only used protons ($Z = 1$) in our simulation, but as mentioned in the beginning of Sec. 3.2 we would expect the results to hold for any combination where E/Z is equal (see also eqs. (2.31) and (2.35). Furthermore, we should perform new simulations with other bubble parameters, but the same parameters for the TMF and external field (and vice versa), to see whether or not we obtain any difference in the mean escape times. This, as earlier

mentioned, we did not have the time to perform.

3.4 Bursting Source

Bursting sources of VHE CRs like SNe are common in the universe. One of the closest SNR to our Sun is the Vela SNR located in an adjoined superbubble to the LB, about 250 pc away, and its age is approximated to be 12 000 years (NASA, 2015). Knowing how the distribution of CRs from the Vela SN (and others) would possibly look like (e.g. at the Earth today) would be of high interest. We therefore simulate trajectories of protons emitted from a bursting source and sample their positions at given points in time to compute the probability density of the CRs at these times. We assume isotropic emission from the source as well as the source being located at the center of our bubble model. The bubble model used is the CW-ACW model (see Sec. 2.1.1) with the MF parameters as defined in Tab. 3.1 (see Sec. 3.2), i.e. the same as what was used in Sec. 3.3 for a continuous CR source.

In Sec. 2.3 we showed that the probability density w.r.t. the xy-plane of isotropically ejected particles at a time t follows eq. (2.46), while CRs in diffusive motion follow a Gaussian distribution (see eq. (2.49). To describe our results we fit the function in eq. (2.62), i.e. the fourth case of curve fitting (see Sec. 2.3.1) which is a product between these two distributions. We expect this function to explain the probability distributions well as either parameter σ or R_m may go to infinity and thus giving either a ballistic or diffusive probability density respectively. In addition, for a constant distribution of particles both σ and R_m would go to infinity.

From the results in Sec. 3.3 we already have a notion of what energies gives diffusive or ballistic motion (or a combination) for our bubble model. From the results in Sec. 3.3 we choose 4 energies to simulate trajectories for: $1.0 \cdot 10^{14}$ eV, $1.0 \cdot 10^{15}$ eV, $1.0 \cdot 10^{16}$ eV, and $1.0 \cdot 10^{18}$ eV. At $E = 1.0 \cdot 10^{14}$ eV we expect to see approximately pure diffusive motion, e.g. see Fig. 3.5, while we at $E = 1.0 \cdot 10^{18}$ eV expect approximately pure ballistic motion. The two other energies are chosen from Fig. 3.9 as they indicate the end of diffusive motion at $E = 1.0 \cdot 10^{15}$ eV (see Fig. 3.9 and the start of easier barrier penetration, i.e. less reflection, at $E = 1.0 \cdot 10^{16}$ eV. The details of the specific parameters of the TMF and number of particle trajectories for each simulation can be seen in Tab. B.7 in the appendix.

We ran simulations of the four energies mentioned earlier and sampled the positions of the particles after they had propagated for 100, 300, 1 000, 3 000, and 10 000 years. The resulting probability densities at each propagation time for each energy are shown in Figs. 3.10-3.13. The probability densities was calculated in r-intervals as was done in Secs. 3.2 and 3.3 (20 bins of $\Delta r = 2.41$ pc inside, 10 bins of $\Delta r = 0.36$ pc in the barrier), but outside the bubble the bin size was doubled to that of the bins inside (i.e. $\Delta r = 4.82$ pc). Each probability density was curve fitted in the same manner as in Sec. 3.3.1, using eq. (2.62) as the fit function of which the best fits are plotted in the same figures as the probability densities. Additionally, all fitting parameters from the best fits of the probability densities in Figs. 3.10-3.13 are shown in Tabs. B.9-B.15 in the appendix. The relative change in particle momentum, due to numerical error in the solving of the EOM, can be seen in Tab. B.8. We see from the table that the relative momentum change is substantially low for all energies. At $E = 1.0 \cdot 10^{18}$ eV has a gyroradius $R_g \approx 200pc$ in the outside MF, meaning that even for the largest energy we expect total deflection angles larger than 2π over a time period of 10 000 years (propagation length $\sim$ 3100 pc).

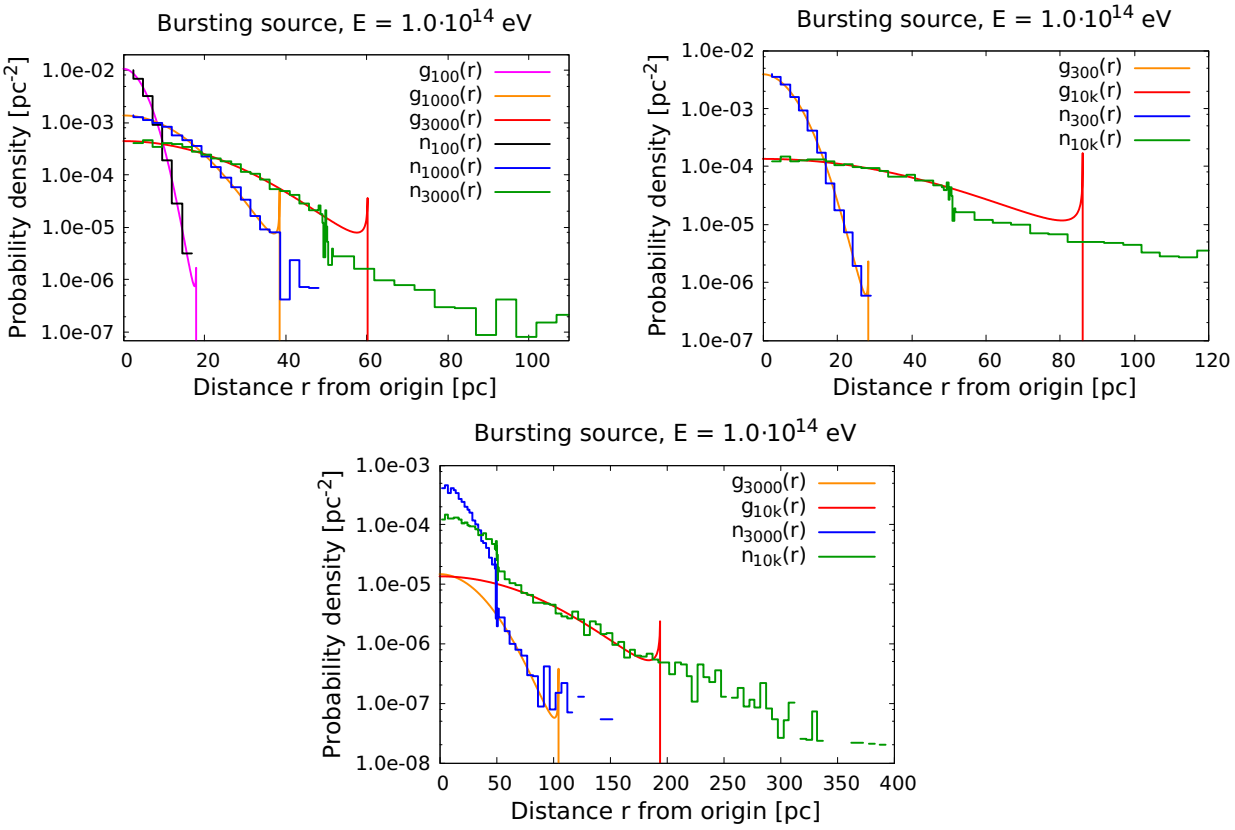

Figure 3.10: The plots show the computed probability densities from $1.0 \cdot 10^{14}$ eV protons ejected from a bursting source located in the center of the modelled superbubble. The top plots show the probability densities ($n(r)$) with the respective best fit from the curve fitting ($g(r)$, eq. (2.62)) at respectively 100, 1 000, and 3 000 years (left), and at 300 and 10 000 (10k) years (right) after the ejection from the origin. In the top plots $g(r)$ is only fitted to the probability density inside the bubble ($r < 50$ pc). In the bottom plot, the probability densities after 3 000 and 10 000 years are plotted to their outer limit, and $g(r)$ is only fitted to the data outside the bubble ($r > 50$ pc).

First we look at the plots and results from $E = 1.0 \cdot 10^{14}$ eV seen in Fig. 3.10 and Tabs. B.9 and B.10. From the curve fitting inside the bubble (i.e. only fitting to data points inside) we see that the parameter R_m is close to the highest values of r (i.e. $r_{\max}$) where $r_{\max} < 50$ pc, but that it is larger than 50 pc for the times where the particles have reached the wall (i.e. 3 000 and 10 000 yr). The only place where R_m seams to have a larger effect on the fitting is after a propagation time of 1 000 yr where, though only some particles have reached the wall, the best fit found it better to cut off earlier thus cutting off the last bins. This might have been different if we were to have more trajectories giving better precision. The more prominent feature of the fit is that σ is well defined and do not "diverge", meaning we do not have a case where the probability density inside the bubble becomes constant. One would from theory expect $\sigma^2 \propto t$, i.e.

$$\sigma / \sqrt{t} = \sqrt{2D} = \text{constant}$$

from diffusive motion (see eq. 2.48). Calculating $\beta = \sigma / \sqrt{t}$ from the fitted parameters inside the bubble we get

$$\begin{aligned}
\beta_{100} &= 0.373 \pm 0.002 \text{ pc s}^{-\frac{1}{2}}, \\
\beta_{300} &= 0.352 \pm 0.003 \text{ pc s}^{-\frac{1}{2}}, \\
\beta_{1000} &= 0.563 \pm 0.019 \text{ pc s}^{-\frac{1}{2}}, \\
\beta_{3000} &= 0.188 \pm 0.008 \text{ pc s}^{-\frac{1}{2}}, \\
\beta_{10\text{k}} &= 0.305 \pm 0.071 \text{ pc s}^{-\frac{1}{2}}.
\end{aligned}$$

We see that these values do not match, indicating we do not have pure diffusive motion, but as mentioned earlier in Sec. 3.3 we do not expect this either as we have a regular field component in our MF and the gyroradius is not much smaller than λ_B. What is interesting is that the values at 100, 300 and 10 000 yr are not too different, and in a logarithmic scaling between 100 and 10 000 yr we get a decrease in value of 0.034 per decade. With this estimation we get a value $\beta_{300} \approx 0.356$ pc s$^{-0.5}$, which is not fat off from the calculated value. On the other hand, the error in $\beta_{10\text{k}}$ is so large that it contains β_{100} and β_{300} thus one may actually have something that is constant (i.e. the diffusion coefficient D). The fact that at both β_{1000} and β_{3000} deviate much from the other values indicates that the values are not very stable w.r.t. the curve fitting. The value of β at 1 000 yr might be explained due to the R_m parameter being smaller than $r_{\max}$ of the particles, but how much it changes β_{1000} is hard to predict. Calculating β from the parameters fitted outside the bubble one has $\beta_{3000} = 0.497$ pc s$^{-0.5}$, and $\beta_{10\text{k}} = 0.621$ pc s$^{-0.5}$,. These values are less well defined, due to the high relative error in the parameters and potentially bad curve fitting (see Fig. 3.10).

As we are also interested in the distance the CR particles may traverse in 10 000 years (i.e. about the age of the Vela SNR) we see that the first particles reach a radial distance $r = 250$ pc in between 3 000 and 10 000 years after being emitted from the source. In other words, if the model was representative of the superbubble where the Vela SNR is located and our LB, which it is not due to assumed ISM outside the bubble, protons from Vela with energy $E = 1.0 \cdot 10^{14}$ eV could have reached the earth by now. An additional aspect is worth noting, namely that as the regular field outside the bubble is mainly pointing in one direction (x-direction in the case of

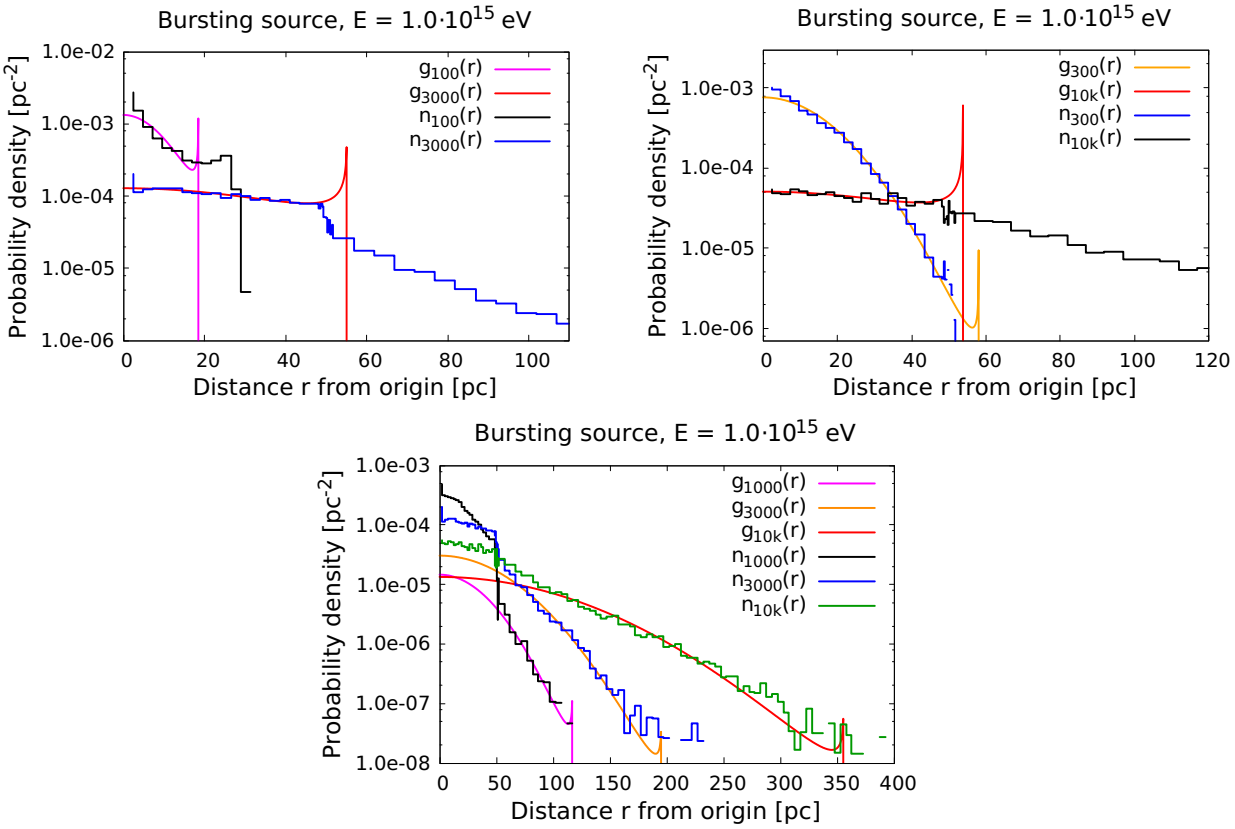

Figure 3.11: The plots show the computed probability densities from $1.0 \cdot 10^{15}$ eV protons ejected from a bursting source located in the center of the modelled superbubble. The top plots show the probability densities ($n(r)$) with the respective best fit from the curve fitting ($g(r)$, eq. (2.62)) at respectively 100 and 3 000 years (left), and at 300 and 10 000 (10k) years (right) after the ejection from the origin. In the top plots $g(r)$ is only fitted to the probability density inside the bubble ($r < 50$ pc). In the bottom plot, the probability densities after 1 000, 3 000, and 10 000 years are plotted to their outer limit, and $g(r)$ is only fitted to the data outside the bubble ($r > 50$ pc).

our model), the particles are most likely to move along the regular fields MFLs. This is visualized in Figs. C.1 and C.2 in the appendix, where a single particle trajectory for four different proton energies ($1.0 \cdot 10^{14}$ eV included) are plotted out to $r = 100$ pc.

Moving on to the simulations of protons with energy $E = 1.0 \cdot 10^{15}$ eV (see Fig. 3.11, Tabs. B.11 and B.12) we go further away from diffusive motion inside the bubble ($R_g = 10$ pc $= \lambda_B$). This is mostly clear when we look at the probability density after 100 years (i.e. ~ 30 pc of propagation) in Fig. 3.11 where the probability density curves up for the largest values of r. The rest of the probability densities has no local maximum towards the outer radial distances and, especially inside the bubble, we see "smoother" distributions. The best fit of this probability density (100 yr) is regrettably quite bad as it cuts off the probability density at $R_m < 20$ pc. The rest of the fitted curves perform better than the first, though the one for 1 000 yr inside the bubble is not plotted due to data overlapping and making the plots harder to read. We see further that the curve fitting of the probability densities outside the bubble perform better than for proton

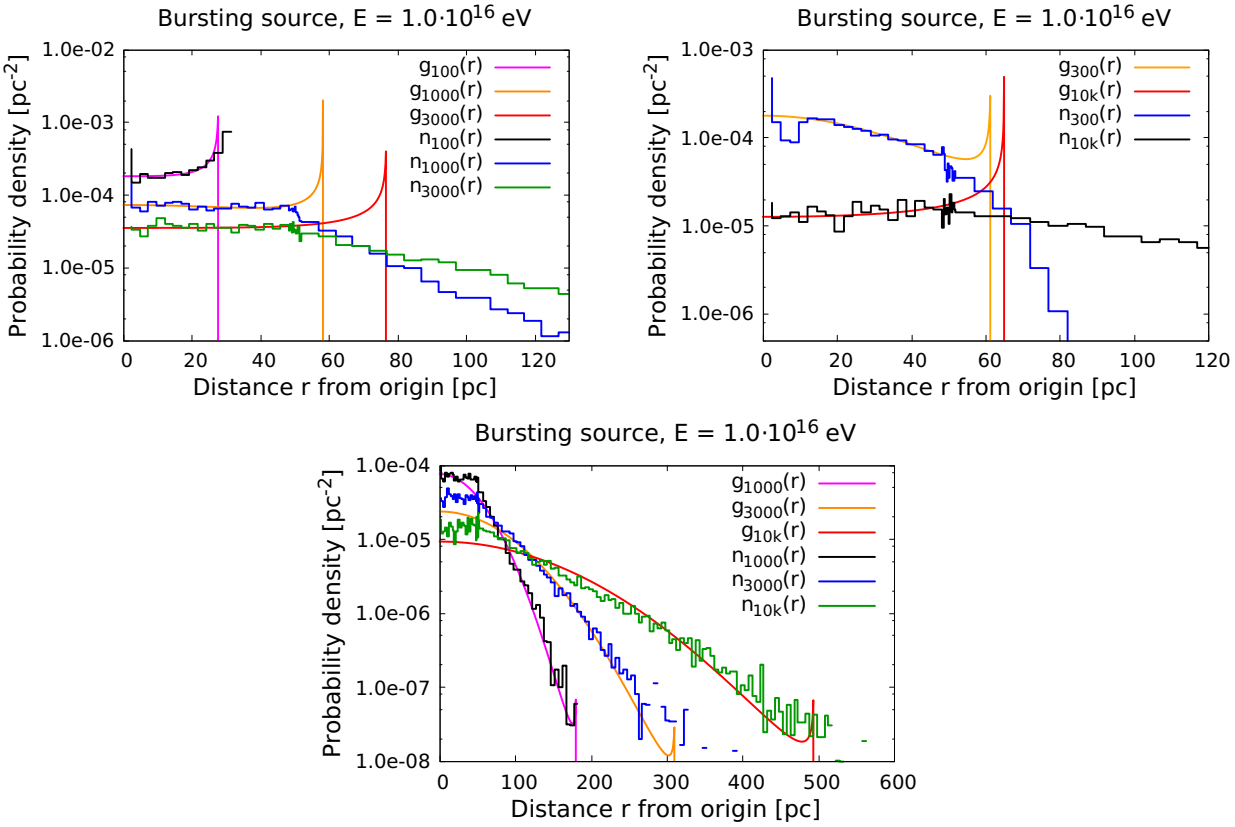

Figure 3.12: The plots show the computed probability densities from $1.0 \cdot 10^{16}$ eV protons ejected from a bursting source located in the center of the modelled superbubble. The top plots show the probability densities ($n(r)$) with the respective best fit from the curve fitting ($g(r)$, eq. (2.62)) at respectively 100, 1 000, and 3 000 years (left), and at 300 and 10 000 (10k) years (right) after the ejection from the origin. In the top plots $g(r)$ is only fitted to the probability density inside the bubble ($r < 50$ pc). In the bottom plot, the probability densities after 1 000, 3 000, and 10 000 years are plotted to their outer limit, and $g(r)$ is only fitted to the data outside the bubble ($r > 50$ pc).

energies $E = 1.0 \cdot 10^{14}$ eV, most likely because of the fact that the higher energy particles escape faster and thus more particles are outside the bubble after an equal amount of time. This in turn improves the precision of the probability densities outside the bubble while decreasing the precision inside. Additionally we notice that the particles reach 250 pc at a time $t \geq 3\,000$ yr, i.e. faster than for the lower energy. Lastly we notice that the probability density inside the bubble starts to approximate a constant value after 10 000 years, but there is still some curvature in the data.

Continuing to the next energy of the simulations, we now look at the probability densities for the protons with $E = 1.0 \cdot 10^{16}$ eV and their fitted curves (see Fig. 3.12, Tabs. B.13 and B.14). We see from the plot of the probability density after 100 yr that the protons are definitely behaving more like ballistic particles than diffusive inside the bubble. Already at 300 yr many protons have left the bubble and we see that they become more diffusive outside the bubble. Due to the gyroradius being $R_g = 2$ pc $= \lambda_B/5$, the motion outside the bubble is closely representing that of

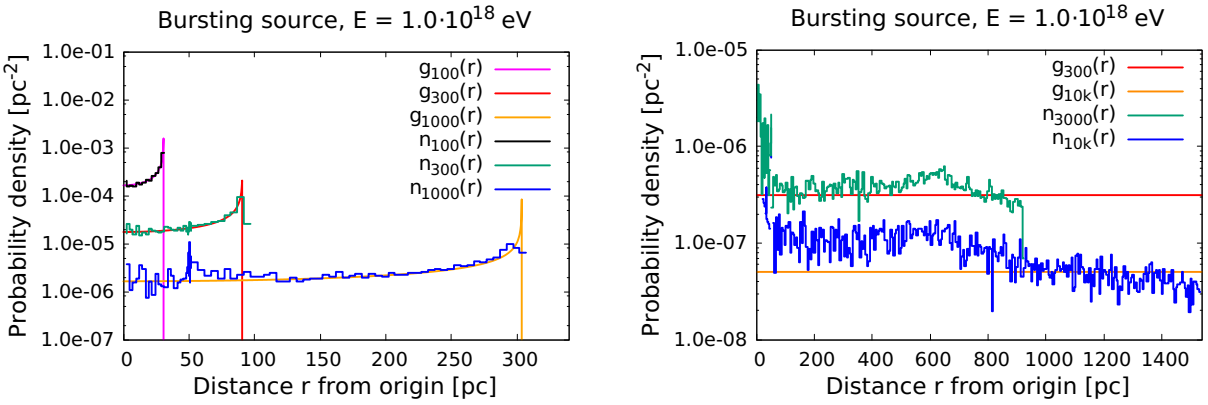

Figure 3.13: The plots show the computed probability densities from $1.0 \cdot 10^{18}$ eV protons ejected from a bursting source located in the center of the modelled superbubble. The top plots show the probability densities ($n(r)$) with the respective best fit from the curve fitting ($g(r)$, eq. (2.62)) at respectively 100, 300, and 1 000 years (left), and at 3 000 and 10 000 (10k) years (right) after the ejection from the origin. In the plots $g(r)$ is fitted to all the probability density data points.

$E = 1.0 \cdot 10^{14}$ eV inside the bubble with the difference being no precisely defined starting time for the particles outside the bubble. Further, we also see that the probability density at 10 000 yr is deviating more from a Gaussian distribution than earlier probability densities. The reason to this might be what we just mentioned about the particles outside the bubble not starting at the same moment at $r = 50$ pc and with gyroradius $R_g = 5$ pc of the same order as λ_B of the TMF, but could just as well be due to the fact the field strengths are different as well as the regular field no longer fulfilling cylinder symmetry. Despite this, the fitted curves are still very close to the simulation data. As with respect to Vela (as with the earlier energies) we see that the first particles reach 250 pc before 3000 years have passed, which is in accordance with the notion that higher energy particles disperse faster in TMFs (Berezinskii et al., 1990).

Looking at the results from last simulated proton energy $E = 1.0 \cdot 10^{18}$ eV (see Fig. 3.13, Tab. B.15) we would expect to see ballistic properties. A difference between the earlier energies and this is that the curve fitting was performed on all data points of the probability densities at once, thus not separating the inside of the bubble from the outside. In the left plot of Fig. 3.13, where the probability densities after 100, 300 and 1000 yr are plotted, we see that the densities are a close match to that of ballistic motion (i.e. $\sigma \gg R_m$) with R_m well defined very close to the total propagation distance (ct) for each time step. Also, we notice that at small radial distances for $t = 1\,000$ yr the probability density start to become very step-like with large variance, which is due to the number of particles in each bin as the area ΔA at lower r is smaller ($\Delta A = 2\pi r \Delta r$).

Looking at the right plot of Fig. 3.13 (3 000 and 10 000 yr) we see that the precision of the computation has failed due to the size of Δr vs. the number of particles, and one would require a greater number of particles to well describe the probability density where it is $< 10^{-6}$ pc^{-2}. To give an analogy, with 10 000 trajectories the probability density corresponding to one single particle inside a r-interval (i.e. Δr) is $2.8 \cdot 10^{-6}$ pc^{-2} at the smallest r ($\Delta r = 2.4$ pc) and $6.8 \cdot 10^{-8}$ pc^{-2} at $r = 50$ pc. Outside it would be smaller due to a doubling of the radial bin size Δr and larger r, giving much larger ΔA. In the curve fitting at 3 000 and 10 000 yr both parameters R_m and σ has

"diverged" giving a constant value as a fit. Additionally we see a trend in the (imprecise) data that the probability density tend to decrease for large radial distances. This may be because the gyroradius is 200 pc outside the bubble, as well as the regular field pointing in the x-direction, thus no longer making the particles ballistic over longer distances. An indication of this may be seen already at 1 000 years where the top in the probability density $r \approx R_m$ are becoming less defined compared to earlier times though this may just be due to the total number of trajectories used. Lastly to cover the notion on the Vela SNR, the particles are relatively ballistic for shorter distances (< 300 pc) and thus one would expect the particles to have passed 250 pc before 10 000 years (as an expanding shell), but the particles could still be deflected back by the magnetic field and thus arriving at a later time as well.

3.5 Limits and Potential Improvements?

From the results in Sec. 3.3 (continuous source) and especially Sec. 3.4 (bursting source) we see that the precision of the computed probability densities is relying heavily on the number of particle trajectories used in the simulations. This is very clear from any energy of the particles with a bursting source given enough propagation time, but also for the very high energies for a continuous source to sample enough time for the probability density which depends on the mean time spent in each radial interval. In the lower energies, especially for a continuous source, the simulations require a long time to finish. This is because of long propagation time for the particles due to many modes required for the TMF (isotropy), the number of decades due to large angle scattering by the TMF, and the fact that the momentum of the particles (i.e. the energy) should not change more than an acceptable amount (preferably less than 1%) meaning the RK solver need to take very small time steps when solving the EOM (calculating the MF for each step). Because of all this, we would need much more computation time in order to improve the precision or to look at smaller energies (which are the most numerous in particle number and sources).

When considering the magnetic field of the bubble, we have used a very simplified model both for the MFLs and the B_{RMS} strength (e.g. compared to van Marle et al. (2015), see Figs. 2.1 and 2.5 vs. Figs. 2.3 and 2.6). Also, we only look at the distribution w.r.t. the Galactic plane, excluding how the distribution of particles is perpendicular to the Galactic field. This is important when considering the extent of the MF in the Galactic disc. To improve on this we would have to implement a more detailed model of the MF and look at the trajectories with angular dependence, especially in the external field. Either we could make the bubble elliptical, like in van Marle et al. (2015), or maybe keep it cylindrical while defining upper and lower boundaries, like lids on a tube, with MF parameters independent of the rest of the bubble (e.g. weaker B_{RMS}). The B_{RMS} strength would have to be redefined as well thus most likely changing the shape of the bubble. A first step would be to make it a two-step barrier (like in Fig. 2.5. The risk of making the model too complex though is not only a larger demand of computation power (or time), but it could also make any source (e.g. the bubble barrier's width) of a property seen (e.g. a fall in probability density over the barrier, or the mean escape time) harder to define or get a measure of its effect.

As touched upon in Sec. 3.4, but also in the introduction, it would be of great interest to see how the probability density of particles from a CR source outside the LB (e.g. the Vela SN)

would look like inside the LB, i.e. modelling two adjoined bubbles and putting the source in one of them. A different yet easier modelling would be to look at the probability density from a CR source (or constant density, i.e. injection at random positions) in the ISM outside the LB in order to gain a picture of how the LB effect these cases of CRs.

Another physical aspect that is not covered in the model is particle interactions. As shown in Figs. 1.1 and 2.1 the bubble barrier itself is a region with a much higher density of particles than the surrounding volume. In these areas, depending on density and particle energy, one would expect a larger probability for particle interactions. This could possibly lead to other effects of the LB on the CR spectra than what could only be described by the MF.

Chapter 4

Conclusion

In this thesis a large number of simulations of very high energy (VHE) cosmic ray (CR) particle trajectories in two magnetic field (MF) models of a superbubble (SB) has been performed, with the goal of describing the effect of a SB on the probability density of CR particles and thus the observable CR spectrum. There are many different bursting sources for VHE CRs, e.g. supernovae (SNe). At low energies, CRs stay longer in the Galaxy, thus one may see many sources which one can approximate by a continuous source (or distribution), while at higher energies a only few sources contribute. Thus both bursting sources and continuous sources of CRs have been simulated.

In Sec. 2.1 two MF models of a SB was modelled with both a regular field component (1st objective, see Sec. 1.1) and a turbulent field component (2nd objective). The regular field component of the two MF models was inspired by van Marle et al. (2015), Beck and Wielebinski (2013), Schulreich et al. (2017), and Streitmatter and Jones (2005) to make the SB most closely resemble the Local Bubble (LB). The regular MF component of the external field in the interstellar medium (ISM) was defined to be constant in in the direction of the Galactic MF (set to x-direction in the models) in the Galactic plane (defined by the xy-plane). The SB's MF was computed as a cylindrical field around the origin with magnetic field lines parallel to the Galactic plane, extending infinitely in the perpendicular direction and out to a radial distance in the plane equal to 51 pc where the transition between the internal bubble field and the external ISM field was modelled. In the first model (labeled CW-ACW) the magnetic field lines was set to follow a clockwise (CW) rotation for $y > 0$ and an anticlockwise (ACW) rotation for $y < 0$, thus making the field component in the x-direction always positive (like the external field component). In the second model (labeled CW) the bubble field was set to follow a clockwise rotation around the origin for all spatial positions. The MF energy ($E_{\mathrm{MF}} \propto B_{\mathrm{RMS}}^2$) of the model (inspired by van Marle et al., 2015; Beck and Wielebinski, 2013) was distributed among the regular MF and the TMF with equipartition, and the root mean square (RMS) strength of the MF (B_{RMS}) was set to be 0.1 μG inside the bubble, 12 μG in the bubble barrier (defined as the outer 2 pc of the bubble), and 5 μG in the external field (see Fig. 2.6).

In Sec. 2.1.2 the turbulent magnetic field (TMF) was modelled using an algorithm presented in Giacalone and Jokipii (1999) which creates turbulent magnetic fields by modelling the fields as a superposition of Fourier modes. By spacing the wave numbers k of the modes on a logarithmic scale with a sufficient number of modes per decade, the algorithm produces an approximately isotropic TMF. Furthermore, the turbulence was set to follow a power law equiva-

lent to Kolmogorov turbulence $E(k) \propto B^2(k) \propto k^{-5/3}$ with a maximal wavelength of the Fourier modes $\lambda_B = 2\pi/k_{\min} = 10$ pc, and the TMF was normalized with a mean square (MS) strength $B^2_{\text{RMS,turb}} = 0.5 \cdot B^2_{\text{tot}}$. In Sec. 3.1 the TMF algorithm was tested using trajectory simulations of particles with a gyroradius $R_g = 10\,000\lambda_B$ and then the resulting RMS deflection angle δ_{RMS} was compared to theory on small angle scattering (SAS) (see Sec. 2.2 and Caprini and Gabici (2015); Harari et al. (2002). It was found that the TMF became sufficiently isotropic with 1 000 Fourier modes per decade, being valid down to just half a decade of modes (500 modes total) when considering the maximum propagation distance for SAS to be $D = 3$ kpc, which is about the width of the halo component of the Galactic MF (De Marco et al., 2007). Furthermore, the δ_{RMS} was shown to follow the scaling with D as expected by the SAS theory, i.e. $\delta_{\text{RMS}} = \Pi\sqrt{D\lambda}/R_g$, but with a scaling factor $\Pi \approx 0.6$ which is about twice that of the theory ($\Pi = 10^{-1/2}$, Caprini and Gabici (2015)).

In Sec. 3.2 the two MF models was compared through trajectory simulations of CRs ejected isotropically from a continuous source (3rd objective) out to a radial distance $r = 100$ pc in the Galactic plane ($r = 2r_{\text{bubble}}$), with particle energies of $1.8 \cdot 10^{14}$ eV, $1.0 \cdot 10^{15}$ eV, $1.0 \cdot 10^{16}$ eV, and $1.0 \cdot 10^{18}$ eV. For each energy the particle probability density was computed as a function of r and the results from both models were compared. At the lowest energy ($E = 1.8 \cdot 10^{14}$ eV) the models showed negligible difference in probability density, but as the energy increased, the probability density of the CW model got relatively larger than the CW-ACW model at smaller r inside the bubble. Additionally, with increasing energy, the fall in probability density over the bubble barrier was shown to decrease in orders of magnitude for the CW-ACW model while being approximately constant for the CW model. The explanation to the difference in probability density with increasing energy, and thereby more ballistic particles, was shown to be caused by resonance like motion across the perpendicular axis (z-axis) in the CW model when the particles were emitted from the source with a zenith angle (w.r.t. the positive z-axis) close to π. The end result was that some of the particles in the CW model tended to propagate far in the negative perpendicular direction thus effectively leaving the Galactic disc while still being traced due to no upper or lower boundary of the model. Because the models showed equal properties at the lower energies (i.e. the most interesting) we chose to only use the CW-ACW model for further simulations.

In Sec. 3.3 further particle trajectory simulations in the CW-ACW model was performed for a continuous source. The simulations traced CRs out to $r = 100$ pc for a set of CR energies from $1.0 \cdot 10^{13}$ eV to $1.0 \cdot 10^{19}$ eV. It was found that the particles' mean escape time from the bubble was following $\langle t_{\text{esc}} \rangle \propto E^{\alpha}$ where $\alpha = 0.354 \pm 0.008$. This result is close to the value $\alpha_{\text{K}} = 1/3$ expected from CR diffusion in a purely isotropic turbulent field defined by Kolmogorov turbulence where the gyroradii of the particles are $R_g \ll \lambda_B$. This time dependence was shown to hold up to energies of $E = 2 \cdot 10^{15}$ eV where α started to decrease, thus giving a steeper curve for $\langle t_{\text{esc}} \rangle$ and a knee-like feature to the mean escape time. At $E \approx 2.4 \cdot 10^{16}$ eV the index α started to increase and going towards zero (i.e. ballistic properties for the particles) for $E = 1 \cdot 10^{19}$ eV. Furthermore, the $\langle t_{\text{esc}} \rangle$ from the simulations showed similarities to Fig. 1 in Giacinti et al. (2015), who argued the "knee" in the CR spectra could be entirely explained by the escape time of CRs from a purely isotropic TMF alone, thus indicating that the LB may give rise to features of the CR "knee" instead of just CR diffusion in the TMF of the ISM. This would have to be further researched through new simulation with different model parameters, which we did not have time to perform.

In Sec. 3.4 we simulated CR trajectories from a bursting source (second part of the 3rd objective) and looked at how the particle probability density for 4 different energies evolved over time. Using energies of $1 \cdot 10^{14}$, $1 \cdot 10^{15}$, $1 \cdot 10^{16}$, and $1 \cdot 10^{18}$ eV, we showed the following for the probability densities. At $E \leq 1 \cdot 10^{14}$ eV the particles move with diffusion like motion described by a Gaussian distribution both inside and outside the bubble, but due imprecise data due to few particle trajectories resulted in bad curve fitting and the scale size of the bubble being of the similar scale to λ_B of the TMF, an estimate of the diffusion coefficient was not possible to acquire. Further we showed that the particles disperse more like ballistic particles inside the bubble as the CR energy increases to $E \approx 1 \cdot 10$ 16 eV. Outside the bubble it was shown that the particles only approach ballistic like motion for $E \approx 1 \cdot 10$ 18 eV, but only for propagation distances of similar order to the particles' gyroradii. To improve the precision of the bursting source data after longer propagation times we would have to increase the number of trajectories quite substantially, thus increasing the computation time with an equal amount.

For possible improvements of the data we would generally have to increase the number of trajectories per particle energy as well as the number of energies to compute. For further research it would be interesting to pursue the result of the mean escape time for a continuous CR source, testing with new bubble models resembling more those from bubble creation simulations (e.g. van Marle et al., 2015). It would also be necessary to view the probability densities of the CRs with angular dependence in the Galactic plane as well as to the perpendicular direction.

Appendix A

Acronyms

CR Cosmic rays
CW Clockwise
CW-ACW Clockwise-anticlockwise
EOM Equation of motion
ISM Interstellar medium
LB Local Bubble
$M_\odot$ Solar mass
MC Monte-Carlo
MF Magnetic field
MFL Magnetic field line
MS Mean square
RK Runge-Kutta
RMS Root mean square
SAS Small angle scattering
SE Standard error
SN Supernova
SNR Supernova remnant
STD Standard deviation
TMF Turbulent magnetic field
SW Stellar wind
VHE Very high energy

Appendix B

Tables of Computation Parameters and Special Results

In this chapter of the appendix the reader will find tables containing information about certain input parameters in the numerical simulations of the particle trajectories described in the Results and Discussion chapter of this thesis (Ch. 3). The reader will also find specific results from the said numerical simulations, as well as all the values of the fitting parameters of the best curve fit to each of the probability densities of the trajectory simulations, see sections 3.3 and 3.4.

Table B.1: An overview of specific TMF parameters and particle trajectories in the field comparison simulations, see Sec. 3.2.

Energy	Number of trajectories	Number of TMF realizations	Number of modes per decade	RK error parameter
E	N_{traj}	N_{real}	n_{dec}	ϵ_{RK}
[eV]	[1]	[1]	[dec^{-1}]	[1]
$1.8 \cdot 10^{14}$	3600	200	1000	$1.0 \cdot 10^{-7}$
$1.0 \cdot 10^{15}$	5000	200	1000	$1.0 \cdot 10^{-7}$
$1.0 \cdot 10^{16}$	20000	400	1000	$3.0 \cdot 10^{-8}$
$1.0 \cdot 10^{18}$	18000	360	1000	$1.0 \cdot 10^{-8}$

Table B.2: An overview of the TMF parameters specific for each simulation in the CW-ACW regular MF model for a continuous source, see Sec. 3.3.

Energy	Number of trajectories	Number of realizations	Number of modes per decade	RK error parameter	Total propagation time
E	N_{traj}	N_{real}	n_{dec}	ϵ_{RK}	t_{tot}
[eV]	[1]	[1]	[dec^{-1}]	[1]	[Myr]
$1.00 \cdot 10^{13}$	900	300	300	$1.0 \cdot 10^{-7}$	36.6
$1.80 \cdot 10^{13}$	900	300	300	$3.0 \cdot 10^{-7}$	29.8
$3.00 \cdot 10^{13}$	900	300	300	$3.0 \cdot 10^{-7}$	27.8
$5.00 \cdot 10^{13}$	800	200	300	$3.0 \cdot 10^{-7}$	19.6
$1.00 \cdot 10^{14}$	1 600	200	300	$1.0 \cdot 10^{-6}$	30.4
$1.80 \cdot 10^{14}$	3 200	200	400	$1.0 \cdot 10^{-6}$	52.1
$3.00 \cdot 10^{14}$	3 200	200	500	$1.0 \cdot 10^{-6}$	48.6
$5.00 \cdot 10^{14}$	1 280	64	1000	$1.0 \cdot 10^{-8}$	17.0
$1.00 \cdot 10^{15}$	5 000	200	1000	$1.0 \cdot 10^{-6}$	55.0
$1.80 \cdot 10^{15}$	3 600	120	1000	$1.0 \cdot 10^{-7}$	33.7
$3.00 \cdot 10^{15}$	4 800	240	1000	$1.0 \cdot 10^{-7}$	36.0
$5.00 \cdot 10^{15}$	3 600	120	1000	$1.0 \cdot 10^{-7}$	22.5
$7.50 \cdot 10^{15}$	8 000	200	1000	$1.0 \cdot 10^{-6}$	39.3
$1.00 \cdot 10^{16}$	40 000	800	1000	$1.0 \cdot 10^{-8}$	155.0
$1.33 \cdot 10^{16}$	8 000	200	1000	$1.0 \cdot 10^{-6}$	23.4
$1.80 \cdot 10^{16}$	8 000	200	1000	$1.0 \cdot 10^{-7}$	16.0
$2.37 \cdot 10^{16}$	8 000	200	1000	$1.0 \cdot 10^{-6}$	12.2
$3.00 \cdot 10^{16}$	8 000	400	1000	$1.0 \cdot 10^{-7}$	10.5
$3.87 \cdot 10^{16}$	8 000	200	1000	$5.0 \cdot 10^{-6}$	9.7
$5.00 \cdot 10^{16}$	8 000	200	1000	$1.0 \cdot 10^{-7}$	9.0
$7.50 \cdot 10^{16}$	8 000	200	1000	$5.0 \cdot 10^{-6}$	8.4
$1.00 \cdot 10^{17}$	40 000	800	1000	$1.0 \cdot 10^{-8}$	37.0
$1.00 \cdot 10^{18}$	18 000	360	1000	$1.0 \cdot 10^{-6}$	9.7
$1.00 \cdot 10^{19}$	18 000	360	1000	$1.0 \cdot 10^{-6}$	9.2

Table B.3: Specific results of the relative change in particle momentum (from injection to extraction) for the trajectory simulations in the CW-ACW regular MF model with a continuous CR source, where the particles were traced to $r = 2r_{\text{bubble}}$ (100 pc) or for 100 000 years, see Sec. 3.3.

Energy E [eV]	Mean rel. momentum change $\langle \Delta p \rangle / p_i$ [1]	STD rel. momentum change σ_p [1]	Max rel. momentum change $\Delta p_{\max} / p_i$ [1]
$1.00 \cdot 10^{13}$	$1.51 \cdot 10^{-3}$	$2.06 \cdot 10^{-3}$	$2.26 \cdot 10^{-2}$
$1.80 \cdot 10^{13}$	$2.76 \cdot 10^{-3}$	$4.08 \cdot 10^{-3}$	$6.75 \cdot 10^{-2}$
$3.00 \cdot 10^{13}$	$1.42 \cdot 10^{-3}$	$2.58 \cdot 10^{-3}$	$5.73 \cdot 10^{-2}$
$5.00 \cdot 10^{13}$	$8.02 \cdot 10^{-4}$	$1.96 \cdot 10^{-3}$	$3.74 \cdot 10^{-2}$
$1.00 \cdot 10^{14}$	$1.04 \cdot 10^{-3}$	$1.58 \cdot 10^{-3}$	$3.78 \cdot 10^{-2}$
$1.80 \cdot 10^{14}$	$4.14 \cdot 10^{-4}$	$5.56 \cdot 10^{-4}$	$9.66 \cdot 10^{-3}$
$3.00 \cdot 10^{14}$	$1.88 \cdot 10^{-4}$	$2.47 \cdot 10^{-4}$	$5.92 \cdot 10^{-3}$
$5.00 \cdot 10^{14}$	$7.78 \cdot 10^{-7}$	$9.63 \cdot 10^{-7}$	$9.35 \cdot 10^{-6}$
$1.00 \cdot 10^{15}$	$1.84 \cdot 10^{-5}$	$2.16 \cdot 10^{-5}$	$3.84 \cdot 10^{-4}$
$1.80 \cdot 10^{15}$	$7.80 \cdot 10^{-7}$	$8.28 \cdot 10^{-7}$	$7.74 \cdot 10^{-6}$
$3.00 \cdot 10^{15}$	$3.97 \cdot 10^{-7}$	$3.89 \cdot 10^{-7}$	$4.05 \cdot 10^{-6}$
$5.00 \cdot 10^{15}$	$9.94 \cdot 10^{-8}$	$8.42 \cdot 10^{-8}$	$6.86 \cdot 10^{-7}$
$7.50 \cdot 10^{15}$	$4.03 \cdot 10^{-7}$	$4.99 \cdot 10^{-7}$	$4.00 \cdot 10^{-6}$
$1.00 \cdot 10^{16}$	$3.58 \cdot 10^{-9}$	$3.04 \cdot 10^{-9}$	$3.79 \cdot 10^{-8}$
$1.33 \cdot 10^{16}$	$1.37 \cdot 10^{-7}$	$1.47 \cdot 10^{-7}$	$1.76 \cdot 10^{-6}$
$1.80 \cdot 10^{16}$	$8.88 \cdot 10^{-9}$	$8.92 \cdot 10^{-9}$	$1.08 \cdot 10^{-7}$
$2.37 \cdot 10^{16}$	$4.72 \cdot 10^{-8}$	$4.14 \cdot 10^{-8}$	$5.59 \cdot 10^{-7}$
$3.00 \cdot 10^{16}$	$5.13 \cdot 10^{-9}$	$4.90 \cdot 10^{-9}$	$4.69 \cdot 10^{-8}$
$3.87 \cdot 10^{16}$	$7.78 \cdot 10^{-9}$	$6.77 \cdot 10^{-9}$	$8.04 \cdot 10^{-8}$
$5.00 \cdot 10^{16}$	$2.03 \cdot 10^{-9}$	$1.71 \cdot 10^{-9}$	$1.97 \cdot 10^{-8}$
$7.50 \cdot 10^{16}$	$4.89 \cdot 10^{-10}$	$4.95 \cdot 10^{-10}$	$8.27 \cdot 10^{-9}$
$1.00 \cdot 10^{17}$	$4.23 \cdot 10^{-11}$	$4.23 \cdot 10^{-11}$	$5.92 \cdot 10^{-10}$
$1.00 \cdot 10^{18}$	$4.69 \cdot 10^{-13}$	$7.55 \cdot 10^{-13}$	$8.76 \cdot 10^{-11}$
$1.00 \cdot 10^{19}$	$4.55 \cdot 10^{-15}$	$6.63 \cdot 10^{-15}$	$6.82 \cdot 10^{-13}$

Table B.4: Fitting parameters from the best fit of the case 1 curve fitting to the proton probability densities inside the bubble, considering a continuous CR source, see Sec. 3.3. A is without units as its units would depend on d in order to get pc^{-2} for eq. (2.61).

E [eV]	A_{in}	ΔA_{in}	σ_{in} [pc]	$\Delta\sigma_{\mathrm{in}}$ [pc]	d_{in} [1]	Δd_{in} [1]
$1.00\cdot10^{13}$	$1.03\cdot10^{-3}$	$5.08\cdot10^{-5}$	$2.47\cdot10^{1}$	$4.23\cdot10^{-1}$	$-4.15\cdot10^{-1}$	$2.16\cdot10^{-2}$
$1.80\cdot10^{13}$	$8.72\cdot10^{-4}$	$2.87\cdot10^{-5}$	$2.55\cdot10^{1}$	$3.14\cdot10^{-1}$	$-3.75\cdot10^{-1}$	$1.45\cdot10^{-2}$
$3.00\cdot10^{13}$	$7.96\cdot10^{-4}$	$2.13\cdot10^{-5}$	$2.54\cdot10^{1}$	$2.58\cdot10^{-1}$	$-3.46\cdot10^{-1}$	$1.18\cdot10^{-2}$
$5.00\cdot10^{13}$	$6.72\cdot10^{-4}$	$1.22\cdot10^{-5}$	$2.74\cdot10^{1}$	$2.21\cdot10^{-1}$	$-3.28\cdot10^{-1}$	$8.03\cdot10^{-3}$
$1.00\cdot10^{14}$	$5.92\cdot10^{-4}$	$1.47\cdot10^{-5}$	$2.97\cdot10^{1}$	$3.96\cdot10^{-1}$	$-3.24\cdot10^{-1}$	$1.10\cdot10^{-2}$
$1.80\cdot10^{14}$	$4.47\cdot10^{-4}$	$1.27\cdot10^{-5}$	$3.26\cdot10^{1}$	$6.02\cdot10^{-1}$	$-2.75\cdot10^{-1}$	$1.26\cdot10^{-2}$
$3.00\cdot10^{14}$	$3.92\cdot10^{-4}$	$1.21\cdot10^{-5}$	$3.37\cdot10^{1}$	$7.30\cdot10^{-1}$	$-2.52\cdot10^{-1}$	$1.37\cdot10^{-2}$
$5.00\cdot10^{14}$	$3.15\cdot10^{-4}$	$5.16\cdot10^{-6}$	$3.56\cdot10^{1}$	$4.50\cdot10^{-1}$	$-2.08\cdot10^{-1}$	$7.30\cdot10^{-3}$
$1.00\cdot10^{15}$	$2.73\cdot10^{-4}$	$4.66\cdot10^{-6}$	$4.94\cdot10^{1}$	$1.25\cdot10^{0}$	$-2.49\cdot10^{-1}$	$7.62\cdot10^{-3}$
$1.80\cdot10^{15}$	$2.31\cdot10^{-4}$	$2.14\cdot10^{-6}$	$1.60\cdot10^{2}$	$2.26\cdot10^{1}$	$-2.82\cdot10^{-1}$	$4.12\cdot10^{-3}$
$3.00\cdot10^{15}$	$1.79\cdot10^{-4}$	$1.15\cdot10^{-5}$	$5.77\cdot10^{6}$	$6.81\cdot10^{15}$	$-2.45\cdot10^{-1}$	$2.79\cdot10^{-2}$
$5.00\cdot10^{15}$	$1.84\cdot10^{-4}$	$1.47\cdot10^{-5}$	$5.38\cdot10^{6}$	$6.77\cdot10^{15}$	$-2.60\cdot10^{-1}$	$3.49\cdot10^{-2}$
$7.50\cdot10^{15}$	$2.03\cdot10^{-4}$	$1.81\cdot10^{-5}$	$2.03\cdot10^{6}$	$4.01\cdot10^{14}$	$-3.00\cdot10^{-1}$	$3.88\cdot10^{-2}$
$1.00\cdot10^{16}$	$2.28\cdot10^{-4}$	$2.25\cdot10^{-5}$	$1.44\cdot10^{6}$	$1.58\cdot10^{14}$	$-3.39\cdot10^{-1}$	$4.27\cdot10^{-2}$
$1.33\cdot10^{16}$	$2.77\cdot10^{-4}$	$2.91\cdot10^{-5}$	$1.93\cdot10^{6}$	$4.06\cdot10^{14}$	$-3.96\cdot10^{-1}$	$4.55\cdot10^{-2}$
$1.80\cdot10^{16}$	$3.59\cdot10^{-4}$	$3.96\cdot10^{-5}$	$2.38\cdot10^{6}$	$7.93\cdot10^{14}$	$-4.81\cdot10^{-1}$	$4.77\cdot10^{-2}$
$2.37\cdot10^{16}$	$4.76\cdot10^{-4}$	$5.26\cdot10^{-5}$	$2.43\cdot10^{6}$	$8.48\cdot10^{14}$	$-5.73\cdot10^{-1}$	$4.78\cdot10^{-2}$
$3.00\cdot10^{16}$	$5.42\cdot10^{-4}$	$5.82\cdot10^{-5}$	$7.91\cdot10^{6}$	$2.84\cdot10^{16}$	$-6.19\cdot10^{-1}$	$4.64\cdot10^{-2}$
$3.87\cdot10^{16}$	$6.21\cdot10^{-4}$	$5.68\cdot10^{-5}$	$7.58\cdot10^{6}$	$2.16\cdot10^{16}$	$-6.66\cdot10^{-1}$	$3.97\cdot10^{-2}$
$5.00\cdot10^{16}$	$6.79\cdot10^{-4}$	$5.29\cdot10^{-5}$	$6.02\cdot10^{6}$	$9.31\cdot10^{15}$	$-7.07\cdot10^{-1}$	$3.39\cdot10^{-2}$
$7.50\cdot10^{16}$	$6.89\cdot10^{-4}$	$5.38\cdot10^{-5}$	$5.92\cdot10^{6}$	$8.84\cdot10^{15}$	$-7.28\cdot10^{-1}$	$3.40\cdot10^{-2}$
$1.00\cdot10^{17}$	$8.44\cdot10^{-4}$	$4.69\cdot10^{-5}$	$6.20\cdot10^{6}$	$7.35\cdot10^{15}$	$-7.92\cdot10^{-1}$	$2.43\cdot10^{-2}$
$1.00\cdot10^{18}$	$1.54\cdot10^{-3}$	$1.02\cdot10^{-5}$	$3.31\cdot10^{6}$	$1.44\cdot10^{14}$	$-9.68\cdot10^{-1}$	$2.96\cdot10^{-3}$
$1.00\cdot10^{19}$	$1.59\cdot10^{-3}$	$8.79\cdot10^{-6}$	$8.13\cdot10^{2}$	$1.77\cdot10^{3}$	$-9.93\cdot10^{-1}$	$2.46\cdot10^{-3}$

Table B.5: Fitting parameters from the best fit of the case 1 curve fitting to the proton probability densities outside the bubble, considering a continuous CR source, see Sec. 3.3. A is without units as its units would depend on d in order to get pc^{-2} for eq. (2.61).

E [eV]	A_{out}	ΔA_{out}	σ_{out} [pc]	$\Delta\sigma_{\mathrm{out}}$ [pc]	d_{out} [1]	Δd_{out} [1]
$1.00\cdot10^{13}$	$1.05\cdot10^{-7}$	$2.69\cdot10^{-7}$	$3.52\cdot10^{1}$	$2.56\cdot10^{0}$	$1.13\cdot10^{0}$	$6.71\cdot10^{-1}$
$1.80\cdot10^{13}$	$1.20\cdot10^{-3}$	$3.22\cdot10^{-3}$	$4.65\cdot10^{1}$	$6.24\cdot10^{0}$	$-1.21\cdot10^{0}$	$7.09\cdot10^{-1}$
$3.00\cdot10^{13}$	$5.21\cdot10^{-6}$	$1.45\cdot10^{-5}$	$3.79\cdot10^{1}$	$3.46\cdot10^{0}$	$2.50\cdot10^{-1}$	$7.31\cdot10^{-1}$
$5.00\cdot10^{13}$	$3.26\cdot10^{-6}$	$8.01\cdot10^{-6}$	$3.63\cdot10^{1}$	$2.70\cdot10^{0}$	$4.89\cdot10^{-1}$	$6.46\cdot10^{-1}$
$1.00\cdot10^{14}$	$3.13\cdot10^{-5}$	$6.76\cdot10^{-5}$	$3.86\cdot10^{1}$	$2.85\cdot10^{0}$	$-2.34\cdot10^{-2}$	$5.69\cdot10^{-1}$
$1.80\cdot10^{14}$	$3.21\cdot10^{-6}$	$6.52\cdot10^{-6}$	$3.40\cdot10^{1}$	$1.84\cdot10^{0}$	$7.00\cdot10^{-1}$	$5.34\cdot10^{-1}$
$3.00\cdot10^{14}$	$9.33\cdot10^{-7}$	$2.17\cdot10^{-6}$	$3.27\cdot10^{1}$	$1.86\cdot10^{0}$	$1.07\cdot10^{0}$	$6.11\cdot10^{-1}$
$5.00\cdot10^{14}$	$8.32\cdot10^{-7}$	$1.74\cdot10^{-6}$	$3.21\cdot10^{1}$	$1.58\cdot10^{0}$	$1.16\cdot10^{0}$	$5.49\cdot10^{-1}$
$1.00\cdot10^{15}$	$9.13\cdot10^{-8}$	$1.78\cdot10^{-7}$	$3.01\cdot10^{1}$	$1.22\cdot10^{0}$	$1.82\cdot10^{0}$	$5.12\cdot10^{-1}$
$1.80\cdot10^{15}$	$2.07\cdot10^{-8}$	$4.27\cdot10^{-8}$	$2.90\cdot10^{1}$	$1.16\cdot10^{0}$	$2.27\cdot10^{0}$	$5.41\cdot10^{-1}$
$3.00\cdot10^{15}$	$1.40\cdot10^{-8}$	$3.37\cdot10^{-8}$	$2.88\cdot10^{1}$	$1.31\cdot10^{0}$	$2.41\cdot10^{0}$	$6.28\cdot10^{-1}$
$5.00\cdot10^{15}$	$9.96\cdot10^{-9}$	$2.24\cdot10^{-8}$	$2.87\cdot10^{1}$	$1.22\cdot10^{0}$	$2.51\cdot10^{0}$	$5.90\cdot10^{-1}$
$7.50\cdot10^{15}$	$3.88\cdot10^{-8}$	$7.33\cdot10^{-8}$	$2.99\cdot10^{1}$	$1.16\cdot10^{0}$	$2.14\cdot10^{0}$	$4.95\cdot10^{-1}$
$1.00\cdot10^{16}$	$5.71\cdot10^{-7}$	$8.11\cdot10^{-7}$	$3.25\cdot10^{1}$	$1.12\cdot10^{0}$	$1.41\cdot10^{0}$	$3.73\cdot10^{-1}$
$1.33\cdot10^{16}$	$4.55\cdot10^{-5}$	$4.71\cdot10^{-5}$	$3.81\cdot10^{1}$	$1.32\cdot10^{0}$	$2.19\cdot10^{-1}$	$2.73\cdot10^{-1}$
$1.80\cdot10^{16}$	$1.84\cdot10^{-3}$	$1.83\cdot10^{-3}$	$4.81\cdot10^{1}$	$2.56\cdot10^{0}$	$-8.03\cdot10^{-1}$	$2.63\cdot10^{-1}$
$2.37\cdot10^{16}$	$4.11\cdot10^{-2}$	$3.19\cdot10^{-2}$	$6.81\cdot10^{1}$	$5.65\cdot10^{0}$	$-1.66\cdot10^{0}$	$2.05\cdot10^{-1}$
$3.00\cdot10^{16}$	$7.95\cdot10^{-2}$	$5.15\cdot10^{-2}$	$8.12\cdot10^{1}$	$8.05\cdot10^{0}$	$-1.85\cdot10^{0}$	$1.71\cdot10^{-1}$
$3.87\cdot10^{16}$	$2.37\cdot10^{-2}$	$1.97\cdot10^{-2}$	$7.23\cdot10^{1}$	$7.38\cdot10^{0}$	$-1.53\cdot10^{0}$	$2.20\cdot10^{-1}$
$5.00\cdot10^{16}$	$1.08\cdot10^{-4}$	$6.80\cdot10^{-5}$	$4.91\cdot10^{1}$	$1.74\cdot10^{0}$	$-1.15\cdot10^{-1}$	$1.65\cdot10^{-1}$
$7.50\cdot10^{16}$	$5.51\cdot10^{-6}$	$2.59\cdot10^{-6}$	$4.68\cdot10^{1}$	$1.12\cdot10^{0}$	$6.23\cdot10^{-1}$	$1.24\cdot10^{-1}$
$1.00\cdot10^{17}$	$3.19\cdot10^{-5}$	$1.76\cdot10^{-5}$	$5.79\cdot10^{1}$	$2.49\cdot10^{0}$	$1.10\cdot10^{-1}$	$1.45\cdot10^{-1}$
$1.00\cdot10^{18}$	$3.77\cdot10^{-3}$	$7.46\cdot10^{-4}$	$3.85\cdot10^{2}$	$2.63\cdot10^{2}$	$-1.21\cdot10^{0}$	$5.24\cdot10^{-2}$
$1.00\cdot10^{19}$	$1.44\cdot10^{-3}$	$2.33\cdot10^{-4}$	$2.53\cdot10^{2}$	$6.07\cdot10^{1}$	$-9.71\cdot10^{-1}$	$4.27\cdot10^{-2}$

Table B.6: Specific results of the propagation time for the trajectory simulations in the CW-ACW regular MF model with a continuous CR source, where the particles were traced to $r = 2r_{\text{bubble}}$ (100 pc) or for 100 000 years, see Sec. 3.3.

Energy	Mean propagation time	Mean time outside	Mean time inside	STD time inside	SE of mean inside	Max time inside
E [eV]	$\langle t_{\text{prop}} \rangle$ [yr]	$\langle t_{\text{out}} \rangle$ [yr]	$\langle t_{\text{in}} \rangle$ [yr]	$\sigma_{t,\text{in}}$ [yr]	$\sigma_{t,\text{mean,in}}$ [yr]	$t_{\text{in,max}}$ [yr]
$1.00 \cdot 10^{13}$	$4.07 \cdot 10^{4}$	$1.85 \cdot 10^{3}$	$3.88 \cdot 10^{4}$	$2.62 \cdot 10^{4}$	$8.74 \cdot 10^{2}$	$1.00 \cdot 10^{5}$
$1.80 \cdot 10^{13}$	$3.32 \cdot 10^{4}$	$1.99 \cdot 10^{3}$	$3.12 \cdot 10^{4}$	$2.10 \cdot 10^{4}$	$6.99 \cdot 10^{2}$	$1.00 \cdot 10^{5}$
$3.00 \cdot 10^{13}$	$3.09 \cdot 10^{4}$	$2.16 \cdot 10^{3}$	$2.87 \cdot 10^{4}$	$2.07 \cdot 10^{4}$	$6.91 \cdot 10^{2}$	$1.00 \cdot 10^{5}$
$5.00 \cdot 10^{13}$	$2.45 \cdot 10^{4}$	$2.43 \cdot 10^{3}$	$2.21 \cdot 10^{4}$	$1.68 \cdot 10^{4}$	$5.93 \cdot 10^{2}$	$9.98 \cdot 10^{4}$
$1.00 \cdot 10^{14}$	$1.90 \cdot 10^{4}$	$2.52 \cdot 10^{3}$	$1.65 \cdot 10^{4}$	$1.27 \cdot 10^{4}$	$3.18 \cdot 10^{2}$	$9.80 \cdot 10^{4}$
$1.80 \cdot 10^{14}$	$1.63 \cdot 10^{4}$	$2.81 \cdot 10^{3}$	$1.35 \cdot 10^{4}$	$1.05 \cdot 10^{4}$	$1.86 \cdot 10^{2}$	$9.06 \cdot 10^{4}$
$3.00 \cdot 10^{14}$	$1.52 \cdot 10^{4}$	$3.02 \cdot 10^{3}$	$1.22 \cdot 10^{4}$	$9.68 \cdot 10^{3}$	$1.71 \cdot 10^{2}$	$9.21 \cdot 10^{4}$
$5.00 \cdot 10^{14}$	$1.35 \cdot 10^{4}$	$3.11 \cdot 10^{3}$	$1.04 \cdot 10^{4}$	$8.61 \cdot 10^{3}$	$2.41 \cdot 10^{2}$	$5.92 \cdot 10^{4}$
$1.00 \cdot 10^{15}$	$1.10 \cdot 10^{4}$	$3.27 \cdot 10^{3}$	$7.75 \cdot 10^{3}$	$6.60 \cdot 10^{3}$	$9.33 \cdot 10^{1}$	$6.91 \cdot 10^{4}$
$1.80 \cdot 10^{15}$	$9.36 \cdot 10^{3}$	$3.32 \cdot 10^{3}$	$6.03 \cdot 10^{3}$	$5.32 \cdot 10^{3}$	$8.87 \cdot 10^{1}$	$4.41 \cdot 10^{4}$
$3.00 \cdot 10^{15}$	$7.52 \cdot 10^{3}$	$3.11 \cdot 10^{3}$	$4.40 \cdot 10^{3}$	$4.15 \cdot 10^{3}$	$6.00 \cdot 10^{1}$	$3.57 \cdot 10^{4}$
$5.00 \cdot 10^{15}$	$6.25 \cdot 10^{3}$	$2.68 \cdot 10^{3}$	$3.57 \cdot 10^{3}$	$3.40 \cdot 10^{3}$	$5.67 \cdot 10^{1}$	$3.43 \cdot 10^{4}$
$7.50 \cdot 10^{15}$	$4.91 \cdot 10^{3}$	$2.19 \cdot 10^{3}$	$2.72 \cdot 10^{3}$	$2.53 \cdot 10^{3}$	$2.83 \cdot 10^{1}$	$2.78 \cdot 10^{4}$
$1.00 \cdot 10^{16}$	$3.87 \cdot 10^{3}$	$1.74 \cdot 10^{3}$	$2.13 \cdot 10^{3}$	$2.02 \cdot 10^{3}$	$1.01 \cdot 10^{1}$	$1.89 \cdot 10^{4}$
$1.33 \cdot 10^{16}$	$2.93 \cdot 10^{3}$	$1.30 \cdot 10^{3}$	$1.62 \cdot 10^{3}$	$1.54 \cdot 10^{3}$	$1.72 \cdot 10^{1}$	$1.44 \cdot 10^{4}$
$1.80 \cdot 10^{16}$	$2.05 \cdot 10^{3}$	$9.31 \cdot 10^{2}$	$1.12 \cdot 10^{3}$	$1.04 \cdot 10^{3}$	$1.16 \cdot 10^{1}$	$1.08 \cdot 10^{4}$
$2.37 \cdot 10^{16}$	$1.53 \cdot 10^{3}$	$7.05 \cdot 10^{2}$	$8.22 \cdot 10^{2}$	$7.63 \cdot 10^{2}$	$8.53 \cdot 10^{0}$	$7.94 \cdot 10^{3}$
$3.00 \cdot 10^{16}$	$1.32 \cdot 10^{3}$	$6.22 \cdot 10^{2}$	$7.02 \cdot 10^{2}$	$6.68 \cdot 10^{2}$	$7.47 \cdot 10^{0}$	$6.94 \cdot 10^{3}$
$3.87 \cdot 10^{16}$	$1.21 \cdot 10^{3}$	$5.78 \cdot 10^{2}$	$6.31 \cdot 10^{2}$	$6.23 \cdot 10^{2}$	$6.96 \cdot 10^{0}$	$5.58 \cdot 10^{3}$
$5.00 \cdot 10^{16}$	$1.11 \cdot 10^{3}$	$5.52 \cdot 10^{2}$	$5.56 \cdot 10^{2}$	$5.76 \cdot 10^{2}$	$6.44 \cdot 10^{0}$	$5.84 \cdot 10^{3}$
$7.50 \cdot 10^{16}$	$1.05 \cdot 10^{3}$	$5.49 \cdot 10^{2}$	$5.01 \cdot 10^{2}$	$5.76 \cdot 10^{2}$	$6.44 \cdot 10^{0}$	$5.77 \cdot 10^{3}$
$1.00 \cdot 10^{17}$	$9.22 \cdot 10^{2}$	$4.82 \cdot 10^{2}$	$4.40 \cdot 10^{2}$	$5.12 \cdot 10^{2}$	$2.56 \cdot 10^{0}$	$5.21 \cdot 10^{3}$
$1.00 \cdot 10^{18}$	$5.41 \cdot 10^{2}$	$2.64 \cdot 10^{2}$	$2.76 \cdot 10^{2}$	$4.55 \cdot 10^{2}$	$3.39 \cdot 10^{0}$	$9.48 \cdot 10^{3}$
$1.00 \cdot 10^{19}$	$5.14 \cdot 10^{2}$	$2.62 \cdot 10^{2}$	$2.52 \cdot 10^{2}$	$4.42 \cdot 10^{2}$	$3.30 \cdot 10^{0}$	$2.69 \cdot 10^{4}$

Table B.7: An overview of the TMF and trajectory parameters specific for each simulation in the CW-ACW regular MF model for a bursting CR source, see Sec. 3.4.

Energy E [eV]	Number of trajectories N_{traj} [1]	Number of realizations N_{real} [1]	Number of modes per decade n_{dec} [dec^{-1}]	RK error parameter ϵ_{RK} [1]
$1.00 \cdot 10^{14}$	4 000	200	300	$1.0 \cdot 10^{-6}$
$1.00 \cdot 10^{15}$	6 000	120	1000	$1.0 \cdot 10^{-6}$
$1.00 \cdot 10^{16}$	6 000	120	1000	$1.0 \cdot 10^{-8}$
$1.00 \cdot 10^{18}$	10 000	200	1000	$1.0 \cdot 10^{-8}$

Table B.8: Specific results of the relative change in particle momentum (from injection to 10 000 years) for the trajectory simulations in the CW-ACW regular MF model with a bursting CR source, where the particles were traced for 10 000 years, see Sec. 3.4.

Energy E [eV]	Mean rel. momentum change $\langle \Delta p \rangle / p_i$ [1]	STD rel. momentum change σ_p [1]	Max rel. momentum change $\Delta p_{\text{max}} / p_i$ [1]
$1.0 \cdot 10^{14}$	$5.44 \cdot 10^{-3}$	$2.70 \cdot 10^{-3}$	$4.12 \cdot 10^{-2}$
$1.0 \cdot 10^{15}$	$8.79 \cdot 10^{-5}$	$2.86 \cdot 10^{-5}$	$6.53 \cdot 10^{-4}$
$1.0 \cdot 10^{16}$	$1.09 \cdot 10^{-5}$	$1.65 \cdot 10^{-6}$	$1.58 \cdot 10^{-5}$
$1.0 \cdot 10^{18}$	$4.66 \cdot 10^{-10}$	$2.70 \cdot 10^{-10}$	$1.92 \cdot 10^{-9}$

Table B.9: Fitting parameters from the best fit (case 4, see eq. (2.62)) of the proton probability densities inside the bubble, considering a bursting CR source and proton energy $E = 1.0 \cdot 10^{14}$ eV, see Sec. 3.4.

E [eV]	A_{in} [pc^{-2}]	ΔA_{in} [pc^{-2}]	$R_{m,\text{in}}$ [pc]	$\Delta R_{m,\text{in}}$ [pc]	σ_{in} [pc]	$\Delta \sigma_{\text{in}}$ [pc]
$1.0 \cdot 10^{2}$	$1.06 \cdot 10^{-2}$	$2.19 \cdot 10^{-4}$	$1.80 \cdot 10^{1}$	$5.56 \cdot 10^{-1}$	$3.73 \cdot 10^{0}$	$1.98 \cdot 10^{-2}$
$3.0 \cdot 10^{2}$	$3.90 \cdot 10^{-3}$	$2.55 \cdot 10^{-4}$	$2.84 \cdot 10^{1}$	$2.96 \cdot 10^{-1}$	$6.10 \cdot 10^{0}$	$5.60 \cdot 10^{-2}$
$1.0 \cdot 10^{3}$	$4.43 \cdot 10^{-4}$	$1.46 \cdot 10^{-5}$	$6.03 \cdot 10^{1}$	$1.06 \cdot 10^{1}$	$1.78 \cdot 10^{1}$	$6.10 \cdot 10^{-1}$
$3.0 \cdot 10^{3}$	$1.37 \cdot 10^{-3}$	$2.63 \cdot 10^{-4}$	$3.86 \cdot 10^{1}$	$2.00 \cdot 10^{0}$	$1.03 \cdot 10^{1}$	$4.46 \cdot 10^{-1}$
$1.0 \cdot 10^{4}$	$1.35 \cdot 10^{-4}$	$4.03 \cdot 10^{-6}$	$8.61 \cdot 10^{1}$	$1.17 \cdot 10^{2}$	$3.05 \cdot 10^{1}$	$7.05 \cdot 10^{0}$

Table B.10: Fitting parameters from the best fit (case 4, see eq. (2.62)) of the proton probability densities outside the bubble, considering a bursting CR source and proton energy $E = 1.0 \cdot 10^{14}$ eV, see Sec. 3.4.

E [eV]	A_{out} [pc^{-2}]	ΔA_{out} [pc^{-2}]	$R_{m,\text{out}}$ [pc]	$\Delta R_{m,\text{out}}$ [pc]	σ_{out} [pc]	$\Delta\sigma_{\text{out}}$ [pc]
$3.0 \cdot 10^3$	$1.48 \cdot 10^{-5}$	$1.05 \cdot 10^{-5}$	$1.05 \cdot 10^2$	$5.08 \cdot 10^{-1}$	$2.72 \cdot 10^1$	$2.31 \cdot 10^0$
$1.0 \cdot 10^4$	$1.36 \cdot 10^{-5}$	$4.52 \cdot 10^{-6}$	$1.94 \cdot 10^2$	$9.64 \cdot 10^0$	$6.21 \cdot 10^1$	$5.26 \cdot 10^0$

Table B.11: Fitting parameters from the best fit (case 4, see eq. (2.62)) of the proton probability densities inside the bubble, considering a bursting CR source and proton energy $E = 1.0 \cdot 10^{15}$ eV, see Sec. 3.4.

E [eV]	A_{in} [pc^{-2}]	ΔA_{in} [pc^{-2}]	$R_{m,\text{in}}$ [pc]	$\Delta R_{m,\text{in}}$ [pc]	σ_{in} [pc]	$\Delta\sigma_{\text{in}}$ [pc]
$1.0 \cdot 10^2$	$1.33 \cdot 10^{-3}$	$6.72 \cdot 10^{-4}$	$1.85 \cdot 10^1$	$1.36 \cdot 10^0$	$7.35 \cdot 10^0$	$1.85 \cdot 10^0$
$3.0 \cdot 10^2$	$7.64 \cdot 10^{-4}$	$3.79 \cdot 10^{-5}$	$5.80 \cdot 10^1$	$1.07 \cdot 10^1$	$1.40 \cdot 10^1$	$3.93 \cdot 10^{-1}$
$1.0 \cdot 10^3$	$1.29 \cdot 10^{-4}$	$5.26 \cdot 10^{-6}$	$5.52 \cdot 10^1$	$5.42 \cdot 10^0$	$3.14 \cdot 10^1$	$3.10 \cdot 10^0$
$3.0 \cdot 10^3$	$3.30 \cdot 10^{-4}$	$1.07 \cdot 10^{-5}$	$4.99 \cdot 10^1$	$9.62 \cdot 10^{-1}$	$1.98 \cdot 10^1$	$4.01 \cdot 10^{-1}$
$1.0 \cdot 10^4$	$5.08 \cdot 10^{-5}$	$1.71 \cdot 10^{-6}$	$5.38 \cdot 10^1$	$3.48 \cdot 10^0$	$3.36 \cdot 10^1$	$2.91 \cdot 10^0$

Table B.12: Fitting parameters from the best fit (case 4, see eq. (2.62)) of the proton probability densities outside the bubble, considering a bursting CR source and proton energy $E = 1.0 \cdot 10^{15}$ eV, see Sec. 3.4.

E [eV]	A_{out} [pc^{-2}]	ΔA_{out} [pc^{-2}]	$R_{m,\text{out}}$ [pc]	$\Delta R_{m,\text{out}}$ [pc]	σ_{out} [pc]	$\Delta\sigma_{\text{out}}$ [pc]
$1.0 \cdot 10^3$	$1.46 \cdot 10^{-5}$	$3.56 \cdot 10^{-6}$	$1.17 \cdot 10^2$	$2.03 \cdot 10^0$	$2.99 \cdot 10^1$	$1.01 \cdot 10^0$
$3.0 \cdot 10^3$	$3.05 \cdot 10^{-5}$	$6.57 \cdot 10^{-6}$	$1.95 \cdot 10^2$	$8.36 \cdot 10^{-1}$	$4.44 \cdot 10^1$	$1.10 \cdot 10^0$
$1.0 \cdot 10^4$	$1.34 \cdot 10^{-5}$	$1.29 \cdot 10^{-6}$	$3.55 \cdot 10^2$	$7.37 \cdot 10^{-1}$	$8.56 \cdot 10^1$	$1.11 \cdot 10^0$

Table B.13: Fitting parameters from the best fit (case 4, see eq. (2.62)) of the proton probability densities inside the bubble, considering a bursting CR source and proton energy $E = 1.0 \cdot 10^{16}$ eV, see Sec. 3.4.

E [eV]	A_{in} [pc^{-2}]	ΔA_{in} [pc^{-2}]	$R_{m,\text{in}}$ [pc]	$\Delta R_{m,\text{in}}$ [pc]	σ_{in} [pc]	$\Delta\sigma_{\text{in}}$ [pc]
$1.0 \cdot 10^2$	$1.82 \cdot 10^{-4}$	$4.21 \cdot 10^{-5}$	$2.77 \cdot 10^1$	$2.02 \cdot 10^{-3}$	$2.93 \cdot 10^1$	$1.81 \cdot 10^1$
$3.0 \cdot 10^2$	$1.79 \cdot 10^{-4}$	$5.66 \cdot 10^{-6}$	$6.12 \cdot 10^1$	$7.83 \cdot 10^0$	$2.78 \cdot 10^1$	$1.77 \cdot 10^0$
$1.0 \cdot 10^3$	$3.55 \cdot 10^{-5}$	$1.85 \cdot 10^{-6}$	$7.66 \cdot 10^1$	$9.85 \cdot 10^1$	$7.75 \cdot 10^1$	$1.54 \cdot 10^2$
$3.0 \cdot 10^3$	$7.33 \cdot 10^{-5}$	$4.56 \cdot 10^{-6}$	$5.82 \cdot 10^1$	$1.42 \cdot 10^1$	$4.41 \cdot 10^1$	$1.57 \cdot 10^1$
$1.0 \cdot 10^4$	$1.27 \cdot 10^{-5}$	$1.12 \cdot 10^{-6}$	$6.49 \cdot 10^1$	$5.00 \cdot 10^1$	$9.94 \cdot 10^1$	$3.50 \cdot 10^2$

Table B.14: Fitting parameters from the best fit (case 4, see eq. (2.62)) of the proton probability densities outside the bubble, considering a bursting CR source and proton energy $E = 1.0 \cdot 10^{16}$ eV, see Sec. 3.4.

E [eV]	A_{out} [pc^{-2}]	ΔA_{out} [pc^{-2}]	$R_{m,\text{out}}$ [pc]	$\Delta R_{m,\text{out}}$ [pc]	σ_{out} [pc]	$\Delta\sigma_{\text{out}}$ [pc]
$1.0 \cdot 10^{3}$	$7.64 \cdot 10^{-5}$	$9.38 \cdot 10^{-6}$	$1.80 \cdot 10^{2}$	$5.31 \cdot 10^{-1}$	$4.07 \cdot 10^{1}$	$5.28 \cdot 10^{-1}$
$3.0 \cdot 10^{3}$	$2.38 \cdot 10^{-5}$	$2.89 \cdot 10^{-6}$	$3.10 \cdot 10^{2}$	$5.61 \cdot 10^{-1}$	$7.08 \cdot 10^{1}$	$1.13 \cdot 10^{0}$
$1.0 \cdot 10^{4}$	$9.34 \cdot 10^{-6}$	$6.23 \cdot 10^{-7}$	$4.93 \cdot 10^{2}$	$3.02 \cdot 10^{0}$	$1.22 \cdot 10^{2}$	$1.52 \cdot 10^{0}$

Table B.15: Fitting parameters from the best fit (case 4, see eq. (2.62)) of the proton probability densities, considering a bursting CR source and proton energy $E = 1.0 \cdot 10^{18}$ eV, see Sec. 3.4.

E [eV]	A_{out} [pc^{-2}]	ΔA_{out} [pc^{-2}]	$R_{m,\text{out}}$ [pc]	$\Delta R_{m,\text{out}}$ [pc]	σ_{out} [pc]	$\Delta\sigma_{\text{out}}$ [pc]
$1.0 \cdot 10^{2}$	$1.64 \cdot 10^{-4}$	$5.94 \cdot 10^{-6}$	$3.08 \cdot 10^{1}$	$1.78 \cdot 10^{-1}$	$1.55 \cdot 10^{5}$	$4.19 \cdot 10^{11}$
$3.0 \cdot 10^{2}$	$1.75 \cdot 10^{-5}$	$9.98 \cdot 10^{-7}$	$9.09 \cdot 10^{1}$	$9.45 \cdot 10^{-1}$	$5.75 \cdot 10^{5}$	$4.55 \cdot 10^{12}$
$1.0 \cdot 10^{3}$	$1.64 \cdot 10^{-6}$	$9.43 \cdot 10^{-8}$	$3.04 \cdot 10^{2}$	$3.18 \cdot 10^{0}$	$1.00 \cdot 10^{4}$	$2.00 \cdot 10^{6}$
$3.0 \cdot 10^{3}$	$3.12 \cdot 10^{-7}$	$1.62 \cdot 10^{-8}$	$9.09 \cdot 10^{6}$	$3.94 \cdot 10^{16}$	$8.44 \cdot 10^{7}$	$3.16 \cdot 10^{19}$
$1.0 \cdot 10^{4}$	$5.06 \cdot 10^{-8}$	$3.64 \cdot 10^{-9}$	$6.40 \cdot 10^{6}$	$2.75 \cdot 10^{16}$	$6.54 \cdot 10^{7}$	$2.94 \cdot 10^{19}$

Appendix C

Trajectory Plots

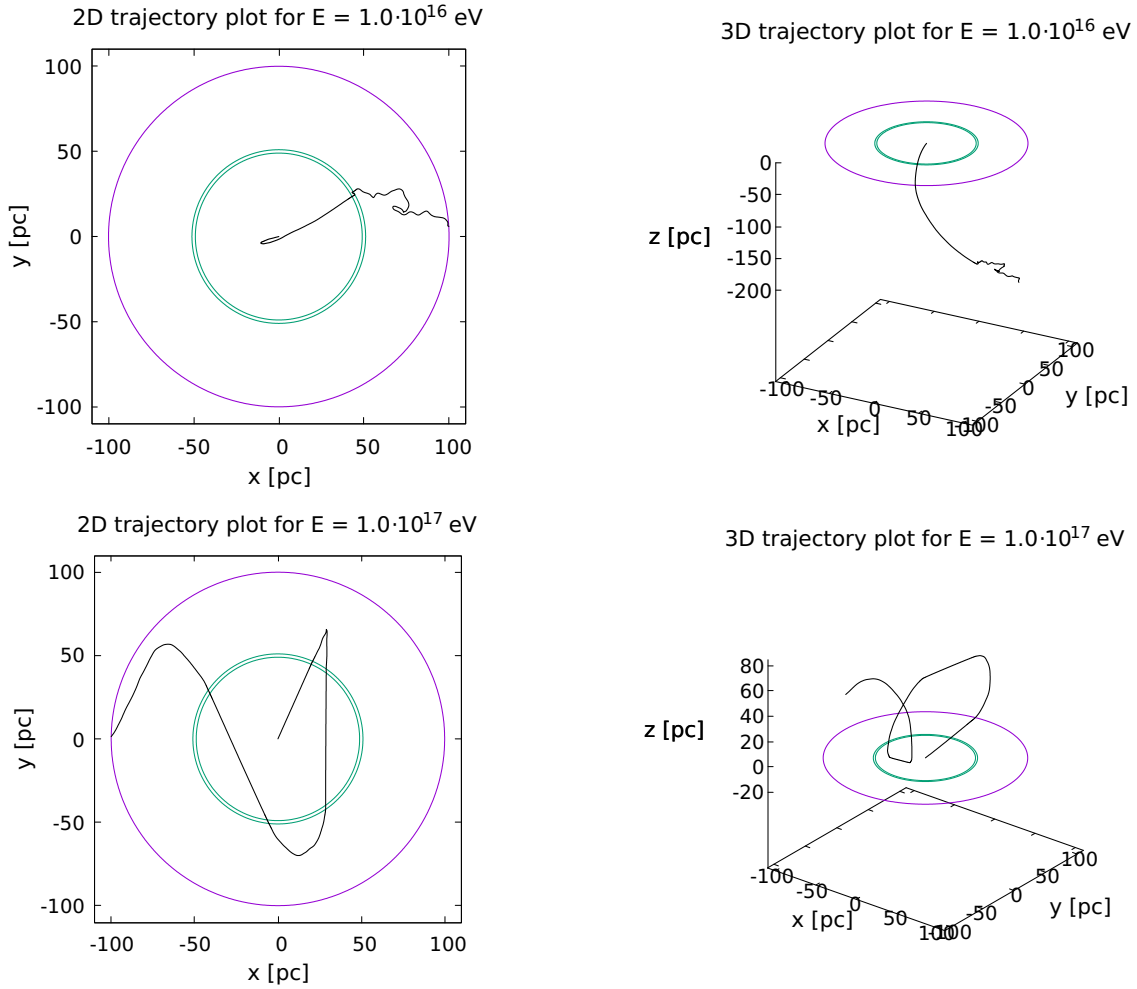

Figure C.1: Single trajectory plots in 2D and 3D for protons with energy $E = 1.0 \cdot 10^{16}$ eV and $E = 1.0 \cdot 10^{17}$ eV in the CW-ACW model. The green circles represent the inner and outer walls of the bubble barrier, while the purple circle represent the outer radius of the constant source model described in Sec. 3.3.

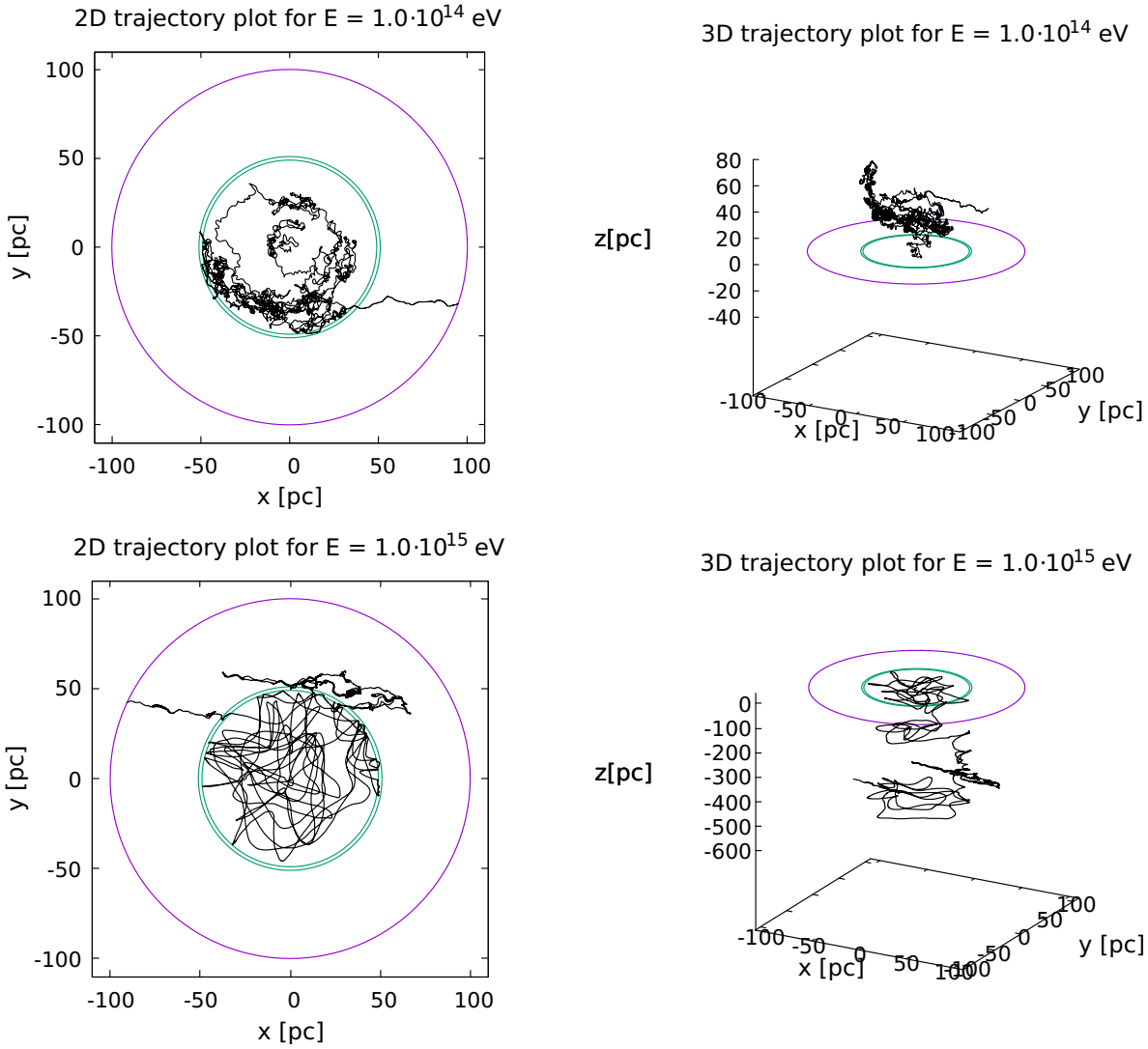

Figure C.2: Single trajectory plots in 2D and 3D for protons with energy $E = 1.0 \cdot 10^{14}$ eV and $E = 1.0 \cdot 10^{15}$ eV in the CW-ACW model. The green circles represent the inner and outer walls of the bubble barrier, while the purple circle represent the outer radius of the constant source model described in Sec. 3.3.

Bibliography

Aharonian, F. A., Kelner, S. R., and Prosekin, A. Y. (2010). Angular, spectral, and time distributions of highest energy protons and associated secondary gamma rays and neutrinos propagating through extragalactic magnetic and radiation fields. *Phys. Rev. D*, 82(4):043002.

Beck, R. and Wielebinski, R. (2013). *Planets, Stars and Stellar Systems*, volume 5. Springer, Berlin, 3rd edition.

Berezinskii, V. S., Bulanov, S. V., Dogiel, V. A., and Ptuskin, V. S. (1990). *Astrophysics of cosmic rays*. North Holland.

Beringer, J. et al. (2012). Review of particle physics. *Phys. Rev. D*, 86:010001.

Bramwell, S. T., Giblin, S. R., Calder, S., Aldus, R., Prabhakaran, D., and Fennell, T. (2009). Measurement of the charge and current of magnetic monopoles in spin ice. *Nature*, 461:956–959.

Caprini, C. and Gabici, S. (2015). Gamma-ray observations of blazars and the intergalactic magnetic field spectrum. *Phys. Rev. D*, 91:123514.

Cardillo, M., Amato, E., and Blasi, P. (2016). Supernova remnant W44: a case of cosmic-ray reacceleration. *Astron. Astrophys.*, 595:A58.

Chen, D., Huang, J., and Jin, H.-B. (2015). Spectra of cosmic ray electrons and diffuse gamma rays with the constraints of AMS-02 and HESS data. *Astrophysical Journal.*, 811(2):154.

De Marco, D., Blasi, P., and Stanev, T. (2007). Numerical propagation of high energy cosmic rays in the Galaxy. I. Technical issues. *JCAP*, 0706:027.

Fowler, J. W. et al. (2001). A Measurement of the cosmic ray spectrum and composition at the knee. *Astropart. Phys.*, 15:49–64.

Gaisser, T. K., Stanev, T., and Tilav, S. (2013). Cosmic Ray Energy Spectrum from Measurements of Air Showers. *Front. Phys.(Beijing)*, 8:748–758.

Galeazzi, M. et al. (2014). The origin of the local 1/4-keV X-ray flux in both charge exchange and a hot bubble. *Nature*, 512:171–173.

Giacalone, J. and Jokipii, J. (1994). Charged-particle motion in multidimensional magnetic-field turbulence. *Astrophysical Journal*, 430(2 PART 2):L137–L140.

Giacalone, J. and Jokipii, J. (1999). The Transport of Cosmic Rays across a Turbulent Magnetic Field. *Astrophysical Journal*, 520(1):L204–L214.

Giacinti, G., Kachelrieß, M., and Semikoz, D. V. (2015). Escape model for Galactic cosmic rays and an early extragalactic transition. *Phys. Rev.*, D91(8):083009.

Griffiths, D. J. (2014). *Introduction to Electrodynamics*. Pearson, Harlow, 4th edition.

Harari, D., Mollerach, S., Roulet, E., and Sánchez, F. (2002). Lensing of ultra-high energy cosmic rays in turbulent magnetic fields. *Journal of High Energy Physics*, 2002(03):045.

Haverkorn, M. and Spangler, S. R. (2013). Plasma Diagnostics of the Interstellar Medium with Radio Astronomy. *Space Science Reviews*, 178:483–511.

Jiang, Y.-Y., Hou, L. G., Han, J. L., Sun, X. H., and Wang, W. (2010). Do Ultrahigh Energy Cosmic Rays Come from Active Galactic Nuclei and Fermi γ-ray Sources? *Astrophysical Journal*, 719:459–468.

Kachelrieß, M., Kalashev, O., Ostapchenko, S., and Semikoz, D. V. (2017). A minimal model for extragalactic cosmic rays and neutrinos. arXiv:1704.06893.

Kachelrieß, M., Neronov, A., and Semikoz, D. V. (2015). Signatures of a two million year old supernova in the spectra of cosmic ray protons, antiprotons and positrons. *Phys. Rev. Lett.*, 115(18):181103.

Lingenfelter, R. E. (2013). Superbubble origin of cosmic rays. In Ormes, J. F., editor, *American Institute of Physics Conference Series*, volume 1516 of *American Institute of Physics Conference Series*, pages 162–166.

NASA (2015). Astronomical picture of the day (january 1st). `https://apod.nasa.gov/apod/ap150101.html`.

NIST (2017). Digital library of mathematical functions. `http://dlmf.nist.gov/`.

Padoan, P., Pan, L., Haugbølle, T., and Nordlund, Å. (2016). Supernova Driving. I. The Origin of Molecular Cloud Turbulence. *Astrophysical Journal*, 822:11.

Press, W. H., Teukolsky, S. A., Vetterling, W. T., and Flannery, B. P. (1997). *Numerical Recipes in Fortran 77*. Press Syndicate of the University of Cambridge, Cambridge, 2nd edition.

Rand, R. J. and Kulkarni, S. R. (1989). The local Galactic magnetic field. *Astrophysical Journal*, 343:760–772.

Rottmann, K. (2003). *Matematisk Formelsamling*. Spektrum forlag, Oslo, 11th edition.

Savchenko, V., Kachelrieß, M., and Semikoz, D. V. (2015). Imprint of a 2 million year old source on the cosmic-ray anisotropy. *The Astrophysical Journal Letters*, 809(2):L23.

Schulreich, M. M., Breitschwerdt, D., Feige, J., and Dettbarn, C. (2017). Numerical studies on the link between radioisotopic signatures on earth and the formation of the local bubble. i. 60fe transport to the solar system by turbulent mixing of ejecta from nearby supernovae into a locally homogeneous ism. arXiv:1704.08221.

Simpson, J. A. and Garcia-Munoz, M. (1988). Cosmic-ray lifetime in the Galaxy - Experimental results and models. *Space Science Reviews*, 46:205–224.

Streitmatter, R. E. and Jones, F. C. (2005). Superbubbles and Local Cosmic Rays. *International Cosmic Ray Conference*, 3:157.

Sun, X. H., Reich, W., Waelkens, A., and Enßlin, T. A. (2008). Radio observational constraints on galactic 3d-emission models. *AA*, 477(2):573–592.

Tautz, R. C. (2012). On Simplified Numerical Turbulence Models in Test-particle Simulations. *Journal of Computational Physics*, 231(14):L4537–L4541.

van Marle, A. J., Meliani, Z., and Marcowith, A. (2015). Shape and evolution of wind-blown bubbles of massive stars: on the effect of the interstellar magnetic field. *Astron. Astrophys.*, 584:A49.